SECOND ANNUAL TECHNICAL PROGRESS REPORT
For Award Period 4/1/03 – 10/1/03

DoE Award #**DE-FC26-01NT41203**
"High-Efficiency Nitride-Based Solid-State Lighting"

OCTOBER 30th, 2003

Authors: Dr. Paul T. Fini, Prof. Shuji Nakamura

University of California, Santa Barbara
Materials Dept., Bldg. 503 rm. 1355
Santa Barbara, CA 93106-5050

DISCLAIMER

“This report was prepared as an account of work sponsored by an agency of the United States Government. Neither the United States Government nor any agency thereof, nor any of their employees, makes any warranty, express or implied, or assumes any legal liability or responsibility for the accuracy, completeness, or usefulness of any information, apparatus, product, or process disclosed, or represents that its use would not infringe privately owned rights. Reference herein to any specific commercial product, process, or service by trade name, trademark, manufacturer, or otherwise does not necessarily constitute or imply its endorsement, recommendation, or favoring by the United States Government or any agency thereof. The views and opinions of authors expressed herein do not necessarily state or reflect those of the United States Government or any agency thereof.”

ABSTRACT

In this second annual report we summarize the progress in the second-year period of Department of Energy contract #**DE-FC26-01NT41203**, entitled "High-Efficiency Nitride-Based Solid-State Lighting". The two teams, from the University of California at Santa Barbara (Principle Investigator: Dr. Shuji Nakamura) and Rensselaer Polytechnic Institute (led by Dr. N. Narendran), are pursuing the goals of this contract from thin film growth, characterization, and packaging standpoints. The UCSB team has recently made significant progress in the development of light-emitting diodes (LEDs) with AlGaN active regions emitting in the ultraviolet (UV), resonant-cavity LEDs (RCLEDs), as well as lateral epitaxial overgrowth (LEO) techniques to obtain large-area non-polar GaN films with low average dislocation density. The Rensselaer team has benchmarked the performance of commercially available LED systems and has also conducted efforts to develop an optimized RCLED packaging scheme, including development of advanced epoxy encapsulant chemistries.

TABLE OF CONTENTS

LIST OF GRAPHICAL MATERIALS

Fig. 27. Plan-view SEM montage showing half of an a-GaN LEO wagon wheel pattern. The angles are included to facilitate reference to the wagon wheel pattern, where 0° corresponds to the GaN c-axis [0001].

Fig. 28. SEM images of stripes oriented parallel to [0001], [$\bar{1}$101], and [$\bar{1}$100]. The images correspond to the 0°, 45°, and 90° orientation labeling in Fig. 14 (scale bar = 5 μm).

Fig. 29. Cross-sectional TEM image of a [$\bar{1}$100] stripe (a) which clearly shows threading dislocation reduction in the asymmetric overgrowth regions. Magnified views of the mask edge region defined by the dashed box on part (a) are shown for (b) [$\bar{1}$100] and (c) [0001] stripes.

Fig. 30. Plan-view panchromatic CL images of stripes oriented parallel to [0001], [$\bar{1}$101], and [$\bar{1}$100]. The images directly correspond to the stripes imaged by SEM in Fig. 5 (scale bar = 5 μm).

Fig. 31. (a) Nomarski optical contrast micrograph of a coalesced LEO *a*-plane GaN film. The stripes are oriented along the $[10\bar{1}0]$ direction. (b-d) AFM images of coalesced $[10\bar{1}0]$-oriented GaN stripes: (b) 40 x 40 μm image showing the relative surface quality of the window and wing regions. (c) Magnified view of the window region. (d) Magnified view of the overgrown region.

Fig. 32. (a) Cross-sectional SEM image of parallel LEO stripes approaching coalescence. (b) Cross-sectional SEM image showing coalesced stripes. The arrows mark sub-micron voids at the wing-mask interface where the stripes coalesced. (c) Plan-view SEM image of the coalesced region pictured in (d), which is a monochromatic CL image of the region shown in (c) at 365 nm. The mask in each case consisted of parallel SiO_2 stripes along the GaN $[10\bar{1}0]$ direction.

Fig. 33. (a) Cross-sectional TEM image of an a-GaN LEO stripe. (b) Plan-view TEM image.

Fig. 34. Relative light output as a function of time for (a) Luxeon red LEDs, (b) Luxeon green LEDs, (c) Luxeon blue LEDs, (d) Luxeon white LEDs, and (e) Shark white LEDs.

Fig. 35. Relative efficacy as a function of time for (a) Luxeon red LEDs, (b) Luxeon green LEDs, (c) Luxeon blue LEDs, (d) Luxeon white LEDs, and (e) Shark white LEDs.

Fig. 36. CIE x,y values of the individual white LEDs after 0, 1000, and 2000 hours.

Fig. 37. Relative light output as a function of time of white LEDs, blue LEDs and blue-plus-phosphor LEDs arrays for 40 mA and 60 mA drive currents.

Fig. 38. Estimated junction temperature as a function of time for white LEDs, blue LEDs, and blue-plus-phosphor LEDs arrays for 40 mA and 60 mA drive currents.

Fig. 39. CIE x,y coordinates of white (top), blue (center) and blue-plus-phosphor (bottom) LED arrays for 40 mA (left) and 60 mA (right) drive currents. The ellipses are centered at the initial x,y value (t=0 hours). The data close to the perimeter of the ellipses represent measurements at t=1100 hours for 40 mA and t=650 hours for 60 mA.

Fig. 40. A commercially available, high-efficiency LED with an epoxy dome.[21]

Fig. 41. A cubic LED can extract light from six surfaces.[22]

Fig. 42. Truncated inverted pyramid (TIP) LED structure by Lumileds.[24]

Fig. 43. Tapered LED structure.[22,26]

Fig. 44. Surface-textured LED structure.[21,27]

Fig. 45. RCLED basic structure.

Fig. 46. UCSB RCLED structure [UCSB].

Fig. 47. Photograph of the forward-biased RCLED with 'interfacial' top-side mirror [UCSB].

Fig. 75. Comparison of the simulated and prototyped results for the diffuse distribution optic (left) and the directional distribution optic (right).

Fig. 76. Comparison of VPC 2000 with conventional 5 mm LED epoxy. Left: unheated conventional epoxy; center: conventional epoxy heated at 140°C for 14 days; right: VPC 2000 heated at 140°C for 3 months.

Fig. 77. Encapsulation of an LED array with VPC 2000 (Left: Filling of the LED cup, Right: cured product).

Fig. 78. Comparison of the light output degradation rates of devices using RPI epoxy and those of a commercial product.

EXECUTIVE SUMMARY

Recently, solid-state lighting based on GaN semiconductors has made remarkable breakthroughs in efficiency, with current commercially available 'white' LEDs at about 20 lm/W. With further improvements to GaN-based LEDs and laser diodes (originally demonstrated by Nakamura and coworkers), we plan to achieve a solid-state light source with >50% efficiency (corresponding to a luminous efficiency of 200 lm/W). GaN LEDs already surpass incandescent technology and have the potential to displace halogen and fluorescent lighting. Not only would GaN-based lasers be the most efficient visible light sources, but they would be non-toxic (mercury-, phosphorus- and arsenic-free) and have projected lifetimes longer than 10 years.

We have assembled a team of researchers in the Materials Department at UC Santa Barbara and at the Lighting Research Center (LRC) at Rensselaer Polytechnic Institute to explore the fundamental issues associated with nitride-based solid-state lighting. The work at UCSB will focus on basic materials and ultraviolet device development. The work at RPI will focus on challenges in packaging, fixturing, testing, and evaluation of nitride-based solid-state lighting.

The ultimate goal at UCSB will be the demonstration of a white-light emitter based on a continuous-wave GaN-based resonant cavity LED or vertical cavity surface emitting laser. Realization of such a structure will require continued improvements in all aspects of our materials. We will focus on the development of bulk GaN substrates which would enable back-side contacting, provide improved thermal conduction over sapphire substrates, and have reduced threading dislocation densities. We will work to optimize all aspects of the device structure with particular emphasis on improvement of InGaN quantum well growth and p-(Al)GaN layer growth. As a result of this work, we will demonstrate a nitride-based white light source with an efficiency of 200 lm/W. The goal for the LRC will be to utilize packaging design and modeling technology to create a light source/fixture useful for general lighting applications and quantify its merits with respect to traditional light sources.

Recently, the UCSB team has made significant progress in the development of light-emitting diodes (LEDs) emitting in the ultraviolet (~ 330-340 nm). This wavelength range is particular interest since it is optimal for excitation of conventional red, green, and blue phosphors. We have also made significant progress in the development of RCLEDs, which have higher efficiency and directional emission than conventional LEDs. Our recent work in the lateral overgrowth of non-polar a-plane GaN by both MOCVD and HVPE has been promising, as we are close to obtaining a free-standing, low dislocation density a-GaN wafer for use as a substrate in device regrowth. In addition, The Rensselaer team has developed target specifications for some of the key parameters for the proposed solid-state lighting system, and has also benchmarked the performance characteristics of currently available commercial LEDs for eventual comparisons to the devices developed in the scope of this project. Work on epoxy encapsulants is progressing steadily, in the effort to obtain an encapsulant that is resistant to damage by ultraviolet light and elevated temperatures.

Note: UCSB and LRC delivered the final presentation of Year 1 accomplishments to DoE on Nov 25th 2002. Following this event, DoE provided input with regard to Year 2 tasks, and LRC/RPI provided UCSB with a revised task list for Year 2 that was incorporated into UCSB's task list, and was submitted to DoE. As a result, the 2nd year funding was delayed until late April 2003. Since November 2002 both UCSB and LRC/RPI have continued working on the project, but at a reduced level.

INTRODUCTION AND EXPERIMENTAL

E.1 Experimental Apparatus

At UCSB, the (Al,In)GaN device layers as well as the A-plane GaN layers described in Sections E.2 and E.4 were deposited by metalorganic chemical vapor deposition (MOCVD). Specifically, Thomas Swan single-wafer vertical close-spaced 'showerhead' deposition chambers were employed for the growth of these films. These chambers feature a showerhead for gas injection, which is a platen with alternating holes supplying group-III (e.g. trimethylgallium, TMG) precursors and ammonia (NH_3). The c-plane sapphire substrate upon which the film is grown is placed on a SiC-coated graphite susceptor, and is separated from the showerhead by about 1 cm. Heat is supplied by BN-coated graphite heater(s) below the susceptor, and the film surface temperature as well as film deposition rate may be monitored through one of three optical ports which extend through the showerhead platen. A pictorial schematic of a multi-wafer version of this reactor design is shown in Fig. 1. Note that the susceptor typically rotates for improved film growth uniformity.

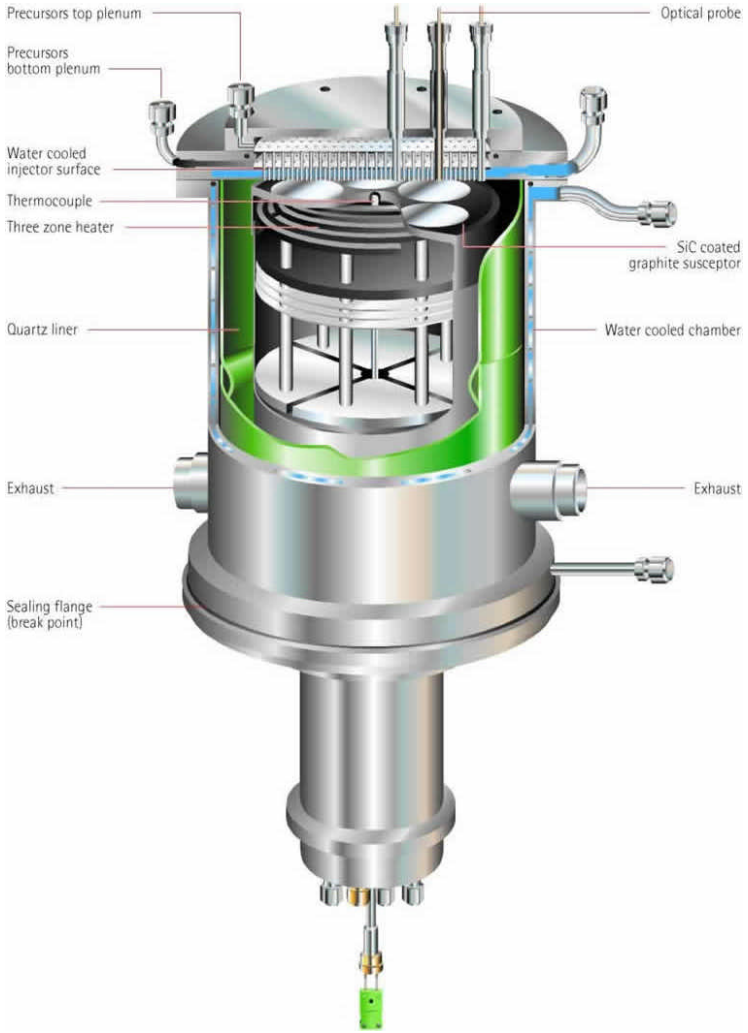

Fig. 1. Pictorial cut-away schematic of a multi-wafer close-spaced vertical showerhead deposition chamber.

(courtesy Thomas Swan Scientific Equipment Ltd.)

For film growth development of resonant-cavity light emitting diode (RCLED) devices discussed in Section E.3, MOCVD in a custom-designed Nippon Sanso cold-wall deposition chamber was performed. This deposition chamber incorporates a pseudo-two-flow approach, directed via a nozzle at a single 2-inch sapphire substrate held by a quartz tray. As in the Thomas Swan showerhead system, heating is

accomplished resistive BN-coated graphite heater, which can reach temperatures of over 1200°C. A typical growth procedure consists of loading a sapphire substrate, performing a hydrogen 'prebake' to clean the surface, deposition of a low-temperature (e.g. 600°C) GaN nucleation layer using TMG and NH_3 as precursors, followed by a high-temperature (e.g. 1050°C) planar GaN layer. Further device layers (e.g. AlGaN cladding layers, p-GaN layer) are then deposited, as discussed in Section E.3. Pictures of this MOCVD system are shown in Fig. 2. The control panel shown in the picture at right has an integrated computer control system, in which programs (recipes) can be developed via a Microsoft Excel® environment in the computer on the left, and uploaded to the computer on the right for execution. A graphical interface allows direct control of most components in the system, including solenoid valves and mass flow controllers.

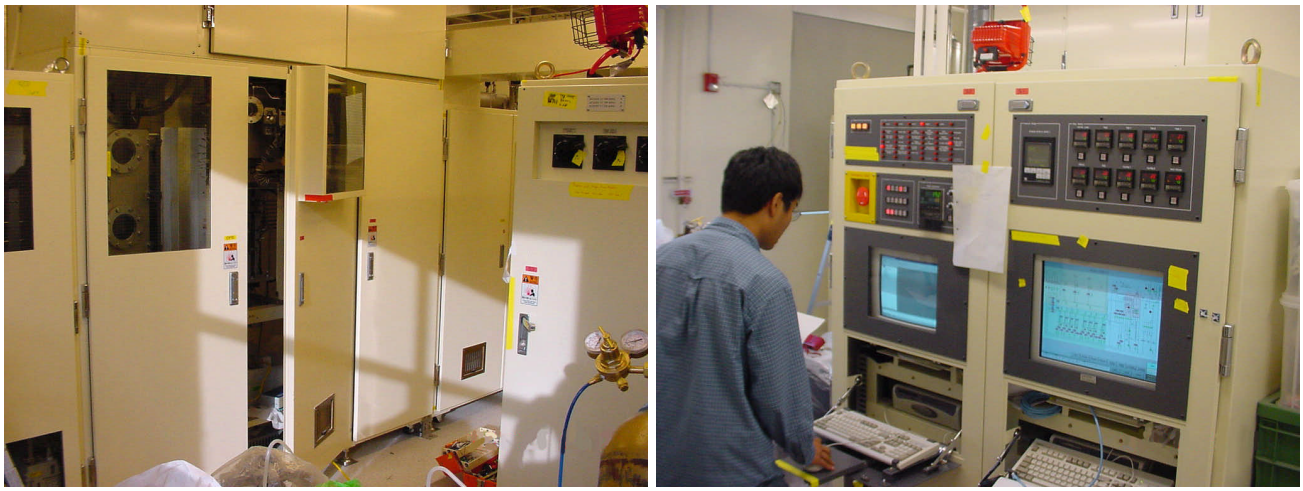

Fig. 2. Front view of Nippon Sanso MOCVD system (left) and Control Panel (right).

All device processing for LEDs discussed in the following sections was carried out in UCSB's multi-user Nanofabrication Facility, which is comprised of Class-10000 and Class-100 cleanrooms. Conventional photolithographic processes were employed, in which a photoresist (PR) such as AZ 4110 is spun onto an as-grown wafer, and is then selectively exposed to ultraviolet light through a patterned metal-on-glass mask. When the photoresist is 'developed', selected areas are removed, whereas others remain to cover the epitaxial film. Subsequently, a variety of processing steps may be carried out, such as selective dry etching by reactive-ion etching (RIE), or metal deposition in an E-beam vacuum deposition chamber. The deposition, patterning, and removal of PR may be performed multiple times depending on the complexity of the device to be fabricated. Processing procedures particular to each type of device are described in more detail in Sections E.2 and E.3. Additionally, procedures relating to the patterning of lateral overgrowth samples are described in Sections E.4 and E.5.

The hydride vapor phase epitaxy (HVPE) lateral overgrowth studies discussed in Section E.5 and R.4 were performed in a hot-wall quartz horizontal-flow reaction chamber (DAIWA Ltd., Tokyo, Japan). This system provides Ga to the growing GaN film via a gaseous HCl flow over liquid Ga upstream of the reaction zone, which creates $GaCl_x$. As in MOCVD, NH_3 serves as the N source for the film. The growth temperature range is similar to that used in MOCVD (1000-1100°C), but heating is provided by a split-shell furnace design. A picture of this HVPE system is shown in Fig. 3.

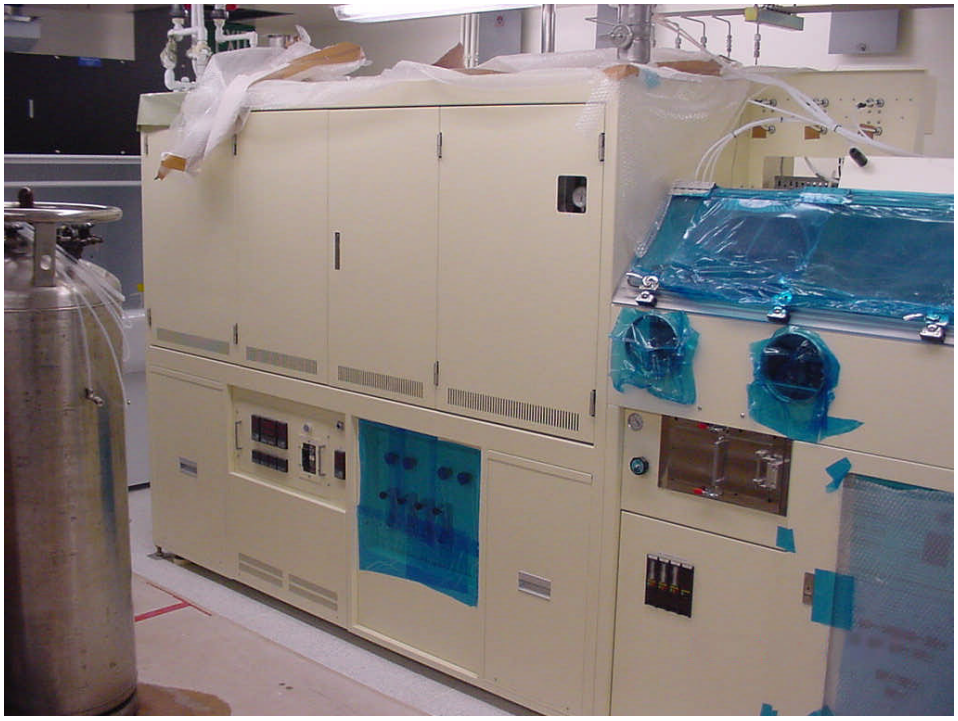

Fig. 3. Front view of Daiwa HVPE system shortly after move-in and installation.

As described in subsequent sections, UCSB has begun fabrication and testing of resonant-cavity LEDs. If these LEDs operate as intended under current injection, the intensity of the emitted light should have a strong directional (angular) dependence, due to mode formation in the LED cavity. To measure this effect, we have constructed a simple computer-controlled measurement setup, shown below in Fig. 4. Via the use of an aperture and collimation lens on a moveable arm, this setup enables angular-dependent intensity measurements, which are useful in determining whether an RCLED is performing as designed.

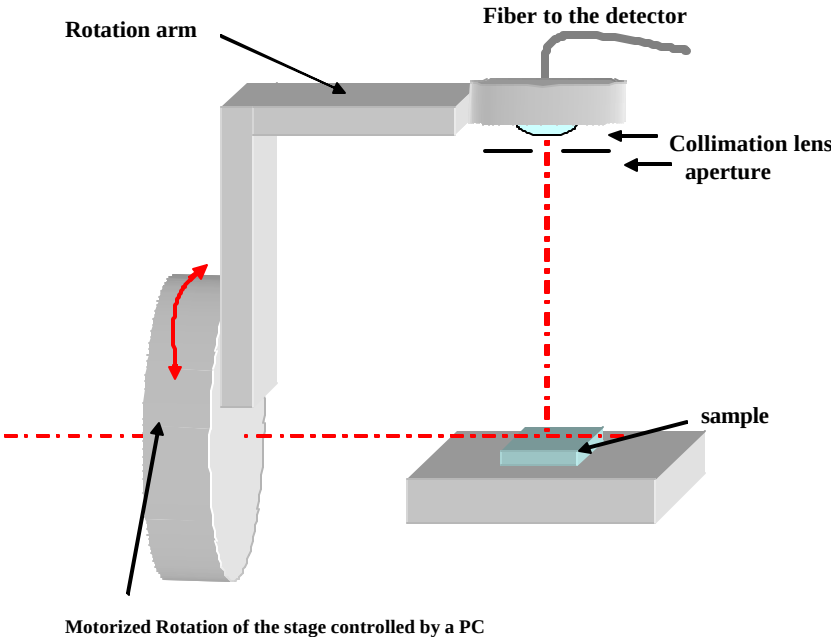

Fig. 4. Schematic of angular measurement system for RCLED testing.

E.2 UV LED Growth, Fabrication, and Testing

Our most recent UV (~340 nm) LED device design is shown schematically in Fig. 5. As previously reported, we have utilized a high-quality GaN 'template' layer on c-plane sapphire to achieve relatively low threading dislocation density. Recently we have also added a low temperature AlN interlayer to inhibit cracking in the overlying AlGaN layers. The active region consists of an $Al_{0.1}GaN$ quantum well surrounded by $Al_{0.16}GaN$ barriers, as well as $Al_{0.3}GaN$ hole- and electron-blocking layers to prevent carrier overflow out of the active region. A short-period alloy superlattice (SPASL) was used in both the n and p-type cladding regions to reduce the vertical resistivity.

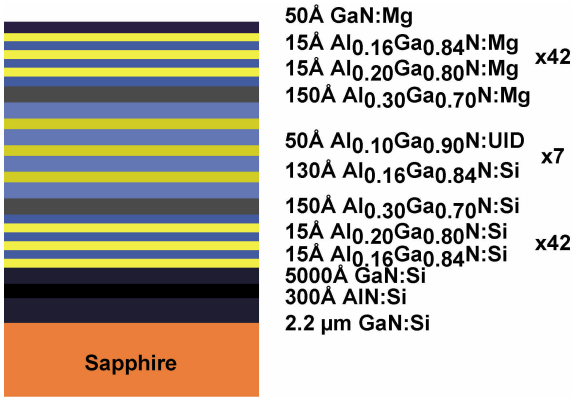

Fig. 5. Cross-sectional schematic of 336 nm UV LED with AlN interlayer to prevent cracking

The growth was performed in a vertical close-spaced metalorganic chemical vapor deposition reactor at 760, 300, and 76 torr for the GaN, AlGaN, and AlN layers respectively. The growth temperatures ranged from ~ 1000 - 1060 °C for all layers except the AlN interlayer which was grown at ~ 930 °C. The AlN was grown in the presence of TMIn resulting in a smoother topography than for films grown without TMIn injection. Devices grown both with and without indium were crack free. The TMAl, and TMIn flows were 10.9, and 16.1 µmol/min respectively, with a V/III ratio of 6896. The indium is acting almost solely as a surfactant as the incorporation is low due to the relatively high growth temperatures for indium-containing compounds. The current epitaxial design is almost at the critical thickness for cracking despite the use of the AlN:In interlayer. It should be noted that if the 5000 Å n-GaN contact layer is removed from on top of the AlN:In, a much thicker device design can be grown without cracking. Although the device can be made much thicker by removing the GaN:Si contact layer, an increase in dislocation density is observed using this growth design, and the lateral current crowding becomes more dominant.

After growth, the samples were annealed at 750 °C for 15 minutes and a semi-transparent Pd/Au (30Å/50Å) p-contact was deposited. The mesa was formed by reactive ion etching in Cl_2 gas at 200W and Ti/Al/Ni/Au (100Å/2000Å/200Å/3000Å) n-contacts were subsequently deposited. A thick Ti/Au (200Å/5000Å) p-pad was then deposited on a portion of the p-contact to be used for probing during test and subsequent wirebonding. The LEDs were then diced, mounted to headers, and wirebonded for testing. A fraction of the headers were also encapsulated in an epoxy typically used for InGaN-based blue and green LEDs.

E.3 RCLED Development

Recently we have begun development of resonant cavity light emitting diodes (RCLEDs), which offer significant benefits over standard LEDs. RCLEDs have improved quantum efficiency over

standard LEDs, due to the Fabry-Perot cavity mode density along the emission axis. In addition, they have enhanced spectral purity due to this Fabry-Perot cavity. Lastly, the active region spontaneous emission emits into the modes of the cavity, which results in highly directional emission. This is made possible by a highly reflective bottom mirror (R > 90%) and a less reflective top mirror (40% < R < 60%) which channel emission to the top of the device.

Significant material growth, fabrication, and design challenges need to be overcome in order to fabricate blue and particularly UV RCLEDs. High-quality material must be grown at a reduced thickness in order to obtain bright emission with a short cavity length that approaches ?/2. In addition, thin structures with appropriate mirror reflectance need to be considered. We have considered dielectric (*i.e.* stacked-oxide) distributed Bragg reflectors (DBRs), epitaxial (*i.e.* 'grown-in') DBRs, metal mirrors, and interfacial mirrors. In addition to cavity thinning techniques, reduced-height structures must be used to achieve efficient, spectrally pure emission. In this report, we describe our initial RCLED fabrication efforts, and we compare their performance with standard LEDs.

A schematic of our present target RCLED design is shown in Fig. 6, which illustrates the key 'building blocks' of this flip-chipped design: highly reflective silver mirror on the p-GaN which also acts as the p-contact in combination with Ni/Au; SiO_2 current aperture, thin active region, transparent indium-tin oxide n-contact spreading layer, and oxide dielectric DBR mirror stack. Although at present we are using the n-GaN/air interface an interfacial 'mirror', we will soon deposit a dielectric mirror stack in combination with an indium-tin oxide transparent current spreading layer. We have chosen a dielectric DBR rather than an epitaxially grown GaN-AlN DBR stack due to our considerable previous use of such oxide stacks in vertical-cavity surface-emitting laser (VCSEL) structures.

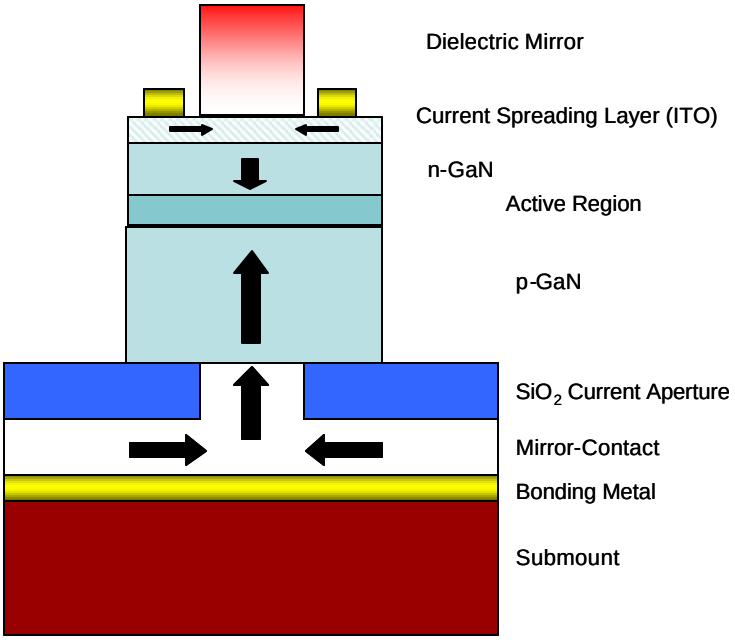

Fig. 6. Schematic of RCLED device structure, which is flip-chipped (*i.e.* p-GaN side down) onto a submount such as Silicon.

The as-grown structure of this device is shown in Fig. 7, which shows that it is not altogether different than conventional InGaN multi-quantum well (MQW) LED device structures. For our initial attempts, we have been utilizing five InGaN QWs with GaN barriers, since it is a relatively well understood system for blue emission. In the eventual move to shorter UV wavelengths, we will be lowering the In content in the wells and then move to GaN and AlGaN QWs, such as have been used in the conventional UV LED structure discussed in section E.1.

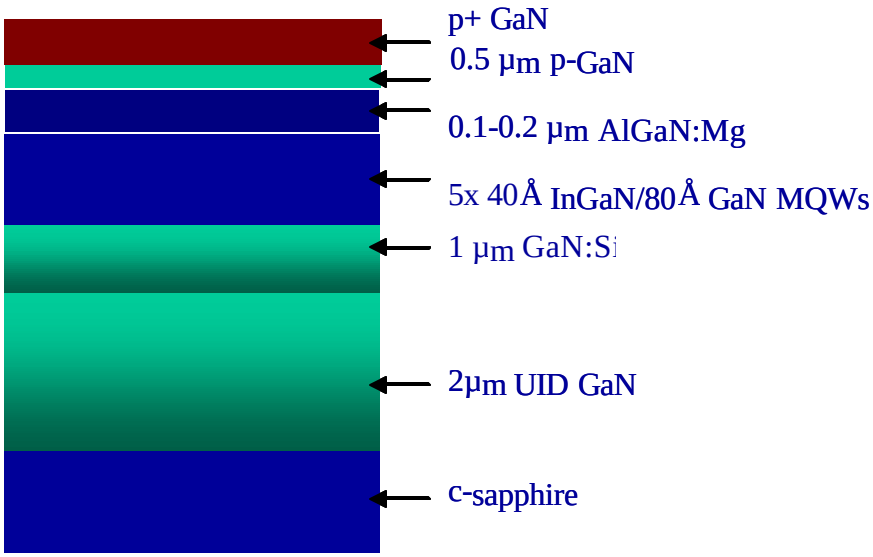

Fig. 7. Schematic of as-grown RCLED device layers on sapphire, which is similar to conventional blue InGaN MQW LED structures.

Once the RCLED device structure has been grown, it is put through a number of processing steps to fabricate the Fabry-Perot cavity and put contacts on both p-GaN and n-GaN sides of the device, as shown in Fig. 8. The process flow shown in this figure stops at removal of the sapphire substrate via KrF excimer laser debonding, but further steps are needed to complete the device, depending on the desired approach. After thinning the cavity by chemical-mechanical polishing and/or dry etching, the simplest means of testing the device after depositing the n-GaN contact is to treat the GaN/air interface as a 'mirror' of much lower reflectivity than the p-side Ag mirror. More reproducibly, a dielectric DBR stack would be deposited in combination with a transparent but conductive ITO contact, as shown in Fig. 2. This approach is still in development, since thinning the cavity via chemical-mechanical polishing reproducibly and without introducing tilt on the sub-micron scale is difficult. Thus we have elected to use a combination of this polishing with dry etching (*e.g.* reactive ion etching or inductively coupled plasma etching) to maintain more control over the final cavity thickness.

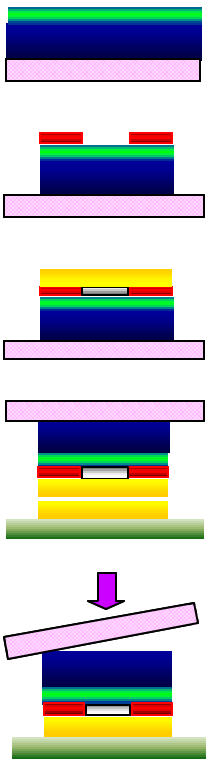

Fig. 8. Process flow for RCLED fabrication, including etching to define the overall device mesa, deposition of the p-GaN current aperture, flip-chipping to a Si submount, and laser lift-off from the sapphire substrate.

E.4 A-plane GaN Lateral Overgrowth by MOCVD

Epitaxial growth of non-polar wurtzite nitride semiconductor films provides a promising means of eliminating polarization-induced electric field effects in nitride semiconductor quantum structures. The total polarization of a wurtzite nitride semiconductor, consisting of spontaneous and piezoelectric components, is aligned along the unique polar axis of the crystal structure. Discontinuities in total polarization result in the formation of fixed sheet charges at the corresponding interfaces or surfaces. Conventional GaN devices employ heterostructures grown along the polar *c*-axis [0001] direction, resulting in the formation of strong electrostatic fields parallel to the growth direction.[1-7] Despite the large internal electric fields in polar nitride devices, technological advances have been achieved due to the continual improvement of epitaxial device layer quality. Although a variety of techniques have been demonstrated, dislocation reduction has been extensively studied in laterally overgrown c-plane GaN via MOCVD.[8-11] Low dislocation density substrates obtained through various lateral overgrowth techniques are directly responsible for the remarkable performance of nitride-based optoelectronics, most notably enhanced lifetime cw-InGaN laser diodes.[12]

Recently, we have grown planar non-polar a-plane $(11\bar{2}0)$ GaN films on $(1\bar{1}02)$ r-plane sapphire substrates via MOCVD.[13] The threading dislocation density present in these films was determined by plan-view transmission electron micrographs to be about 2.6 x 10^{10} cm^{-2}. Improving the crystal quality of these films is fundamental to the realization of high-performance, polarization-free nitride devices. The purpose of this letter is to describe the lateral epitaxial overgrowth (LEO) of non-polar $(11\bar{2}0)$ a-plane GaN seed layers and to report the achievement of threading dislocation reduction. Specifically, the orientation dependence of stripe morphology and dislocation reduction is the focus of this report.

Planar $(11\bar{2}0)$ GaN films (referred to as a-GaN) were grown on r-plane sapphire substrates in a vertical close-spaced MOCVD chamber using a two-step technique.[13] Plasma-enhanced chemical vapor deposition (PECVD) was used to deposit 200 nm of SiO_2 on the as-grown a-GaN, which served as the regrowth mask. The mask pattern was transferred to the SiO_2 using conventional photolithographic techniques and wet etching with buffered hydrofluoric acid. After patterning the mask, the sample was solvent cleaned prior to a selective epitaxy regrowth using the same reactor conditions employed for the heteroepitaxial growth on sapphire (growth temperature of ~1100°C and V/III ratio of ~1300). The regrowth time was kept short so that uncoalesced LEO stripes could be characterized. The stripe morphology was observed using a JEOL 6300 field emission scanning electron microscope (FE-SEM) operating at 5 kV. The microstructure of the lateral overgrowth was studied in cross-section using a JEOL 2000FX transmission electron microscope (TEM) operating at 200 kV. Cathodoluminescence (CL) images were obtained at room temperature using a Gatan MonoCL attached to the JEOL 6300 FE-SEM and provided spatial maps of the luminescence from the laterally overgrown stripes.

E.5 A-plane GaN Lateral Overgrowth by HVPE

Since bulk GaN crystals of appreciable size are not yet available, hydride vapor phase epitaxy (HVPE) has been used to heteroepitaxially grow thick (10-300+ μm) *c*-plane GaN films to serve as homoepitaxial pseudo-substrates for subsequent device growth by molecular beam epitaxy (MBE) and MOCVD. Recently we reported on the first successful growth of planar $(11\bar{2}0)$ *a*-plane GaN by HVPE, demonstrating the potential for fabrication of non-polar GaN substrates. These films described exhibited defect densities comparable to those of heteroepitaxially grown *c*-plane films. However, ideal GaN substrates would be essentially free of threading dislocations, stacking faults, and macroscopic defects that could affect the quality of the device layers subsequently regrown upon them.

As mentioned above, LEO has been demonstrated to be an effective approach for the reduction of threading dislocation densities in *c*-plane GaN by both MOCVD and HVPE. LEO performed by

MOCVD has yielded similar threading dislocation reduction in *a*-plane GaN films. In this report we demonstrate defect reduction in HVPE-grown *a*-plane GaN films via LEO.

The masks for the LEO process were prepared by utilizing conventional photolithographic processing and wet etching on ~ 1300 Å-thick PECVD SiO_2 layers. A variety of mask designs were investigated, including arrays of circular apertures, parallel stripes oriented along the [0001] direction, parallel stripes oriented along the $[10\bar{1}0]$ direction, and non-parallel stripes in a 'wagon-wheel' pattern. The LEO growth process was carried out in a conventional three-zone horizontal directed-flow HVPE system, identical to the system used previously for the growth of planar a-plane $(11\bar{2}0)$ GaN films on *r*-plane sapphire substrates. Typical vertical growth rates ranged from 16 to 40 μm/hr at a substrate temperature of ~ 1040°C. A variety of mask geometries yielded coalesced films; in particular the use of masks consisting of periodic arrays of $[10\bar{1}0]$-oriented stripes allowed full 2-inch diameter *a*-plane GaN wafers to be coalesced.

E.6 Benchmark of current state-of-the-art LED devices

The Lighting Research Center started a study in the first year of this program to benchmark the performance characteristics of currently available commercial high-power LEDs for the purpose of eventual comparisons with the devices developed in the scope of this project. One part of this study was aimed at investigating long-term performance issues. Arrays of LEDs were placed inside specially designed thermal chambers that were housed in a temperature controlled room. The LEDs were operated under various drive currents and ambient temperatures. Light output, luminous efficacy, and color properties (CIE x, y values) as a function of time were measured for five types of commercial high-flux LEDs: red, green, blue, and single-die white LED packages from LumiLeds Lighting (Luxeon), and a multiple-die white LED package from Opto Technology (Shark). LED arrays for each type (total of 15) were powered on for a life test on January 3, 2003. The LEDs were seasoned for 500 hours and then tested for initial light output and other relevant photometric and electrical characteristics. The LED arrays were tested under three different operating conditions: 350 mA and 35°C; 350 mA and 50°C; 450 mA and 35°C. Because each LED type has to operate at a particular ambient temperature, all were tested in specially designed individual life-test chambers built in an LRC lab. These test chambers had two functions: one, to keep the ambient temperature constant, and two, to act as light-integrating boxes for measuring light output parameters. To date, the LRC has collected more than 4,500 hours of life-test data.

E.7 RCLED Packaging Issues – Phosphor Placement

Based on past studies and the long-term performance results, LRC researchers postulated that the performance of phosphor-converted LEDs are negatively affected by placing the down-conversion phosphor very close to the die. This is mainly due to the fact that phosphor medium surrounding the die behaves like an isotropic scatterer and some portion of the light circulates between the phosphor layer, the die, and the reflector cup, and increases the yellowing of the encapsulant. Unlike traditional LEDs, the light output of RCLEDs is much more collimated. In this case much more light from the LRCLED will be coupled back into the device, increasing the junction temperature and thus reducing system efficacy. To validate this theory, the LRC conducted a laboratory study with commercially available 5 mm phosphor-converted (YAG:Ce) white LEDs with the phosphor layer both close to the die and further away. Figure 1 illustrates the LED arrays used in this study. The experiment was conducted at two over drive conditions (currents 40 mA and 60 mA). The ambient temperature remained same (25°C) for both cases. Light output, efficacy, junction temperature, and color properties (CIE x,y) were measured as a function of time. The LEDs were seasoned for 100 hours and then tested for initial light

output and spectral power distribution. Three LED arrays were used for each drive current (Fig. 9). Two of the arrays were assembled using blue LEDs, and one was assembled with white LEDs. One blue LED array and the white LED array were covered with a 5 cm round transparent glass window. The remaining blue LED array was fitted with a similar glass window coated with a YAG:Ce phosphor on the side facing the LED array. The light source assemblies were mounted vertically facing downward. The LED arrays were housed and life-tested inside three chambers, similar to those used in the benchmarking study. To date, the LRC has collected approximately 650 hours for the first condition and approximately 1,200 hours for the second condition. The results showed that the LEDs with the phosphor layer away from the die degraded at a slower rate. Based on this study it was concluded that to improve performance of RCLED white light source, including light source efficacy and life, the phosphor layer must be placed further away from the die.

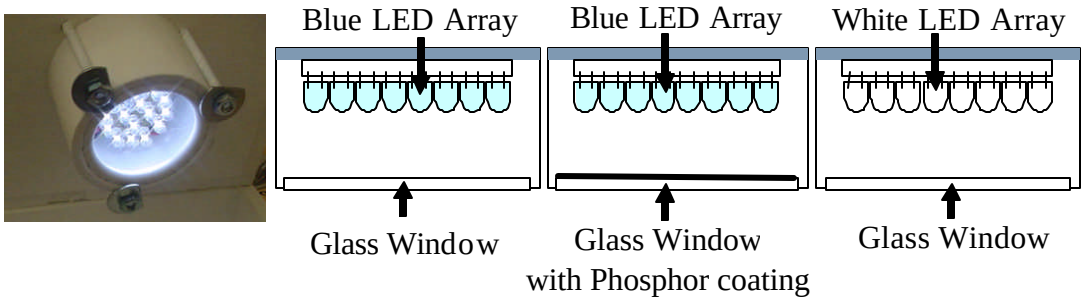

Fig. 9. Photo of an LED array enclosed in an aluminum cylinder and the schematics of the three LED arrays used in the experiments.

E.8 RCLED Packaging Issues – Source Modeling

In light-emitting diodes (LED) total internal reflection (TIR) limits light extraction, and consequently, overall efficacy of the light source. Maximizing the light extraction is important to improving overall efficacy and flux and reducing junction temperature due to internal absorption Increased device temperature affects internal quantum efficiency and the reliability of the devices. Changes in die geometry and surface structure, the index of refraction of the encapsulant, and the shape of the encapsulant offer the opportunity to reduce the luminous flux loss due to TIR and Fresnel reflection losses, and thus increase the light extraction.

The goal of this task was to optimize the chip shape and package design and increase the light extraction efficiency of the resonant-cavity light-emitting diode (RCLED). The LRC conducted a literature review of RCLED structures and solutions to increasing LED or RCLED light extraction efficiency. Using a commercial ray tracing software package, LightTools™, RCLED structures were modeled and the light extraction issue was thoroughly investigated.

E.10 RCLED Packaging Issues – White Light Source Modeling and Prototyping

The next challenge is to package the RCLED into a high efficacy white light source. Prior to constructing the prototype devices, an optical modeling study was conducted identify optimum system components. As described in the section on RCLED Packaging—Phosphor Placement, placing the phosphor layer very close to the RCLED die is not ideal because it would negatively impact performance in terms of efficacy and life. Further analysis showed that placing a phosphor-coated glass plate over the LEDs, as shown in Figure 1, is also not ideal because light reflected off the phosphor still

enters the LED and degrades it. Additionally, it is difficult to create a uniform beam distribution over the glass plate. Therefore, the challenge was to create a packaging concept that would allow the phosphor layer to be removed away from the die and prevent light feedback into the RCLED. At the same time, light from the RCLED must impinge on the phosphor layer uniformly to obtain uniform white light. Based on this criteria, a package was designed with an optical element that redistributed the light from the source uniformly over an outer tube coated with phosphor (Fig. 10). The performance target for the redistributing optical element is to achieve efficiency greater than 94% and uniformity of light along the length of the tube to be greater than less than 10% (less than 10% variation for max/avg ratio).

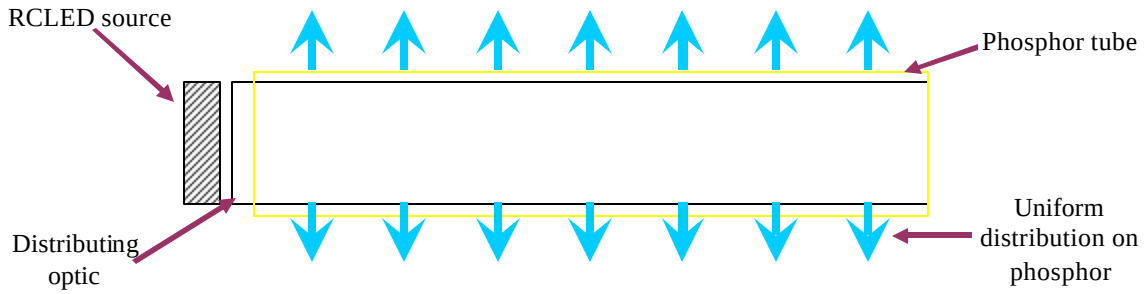

Fig. 10. White light source package using RCLEDs.

An LED source was modeled using LightTools™ ray tracing software. The design and modeling of the optical system was completed using two approaches, which were then optimized for efficiency and uniform light distribution. Prototypes of two models were then built using glass and polycarbonate materials, and the modeled results were compared with the prototypes, which showed good agreement.

E.10 Development of epoxy material

Epoxy development work started during the first year of this project. At RPI's chemistry lab, several novel epoxy resins (structures shown in Table 1) and curing systems for the application of future LED encapsulants were evaluated. The thermal stability test of the polymers was conducted at 140°C for 4 to 14 days. Visual inspection of the samples indicated that all of the samples yellowed significantly while being kept at 140°C and increasingly became more yellow with prolonged treatment.

Table 1. Structures of epoxy resins tested.

PC 1000	PC2003	ERL-4221E
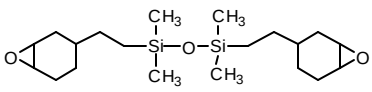	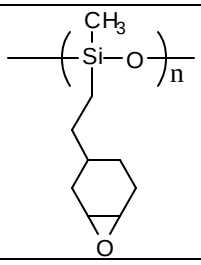	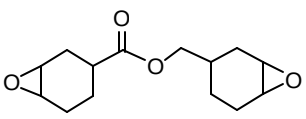

Many other monomers (depicted in Fig. 11) were tested for thermal stability at 140°C but all of them turned yellow after one to two days. The structures of some of the monomers tested are shown below.

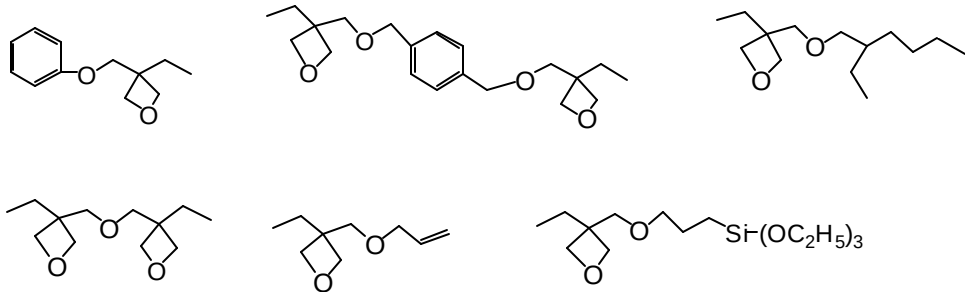

Fig. 11. The structures of the monomers tested.

In addition to the numerous monomers tested, three series of new oligomers were prepared for the encapsulation of RCLEDs. Curing and thermal stability properties of these oligomers were studied, and the results are discussed in section R.9.

RESULTS AND DISCUSSION

R.1 UV LED Growth, Fabrication, and Testing

DC and pulsed LIV measurements for 200 x 200 µm LEDs are shown in Fig. 12. Pulsed data were obtained at a frequency of 1 kHz with a 1% duty cycle. It is clear that self-heating limited the performance of these devices based on the large difference in the current at which the power saturated between DC and pulsed measurements. At 100 mA, the output power was over three times higher for the pulsed conditions, 146 µW, than for DC testing, 44 µW. A sub-linear increase in power with increasing current was already observed at 30 mA under DC conditions while it was not observed until ~150 mA under pulsed conditions. The peak emission wavelength red-shifted by 1.8 nm between electroluminescence taken at 20 and 70 mA which is further evidence of device self-heating with increased current injection. It is anticipated that higher output powers will be obtained as the series resistance is reduced. Power saturation for 50 x 50, 100 x 100, and 150 x 150 µm diodes was observed at 18.1, 26.2, and 31.4 µW for current densities of 2.35, 0.88, and 0.44 kA/cm^2 respectively. Area-dependent power saturation at different current densities indicated non-uniform current injection over the diode area.

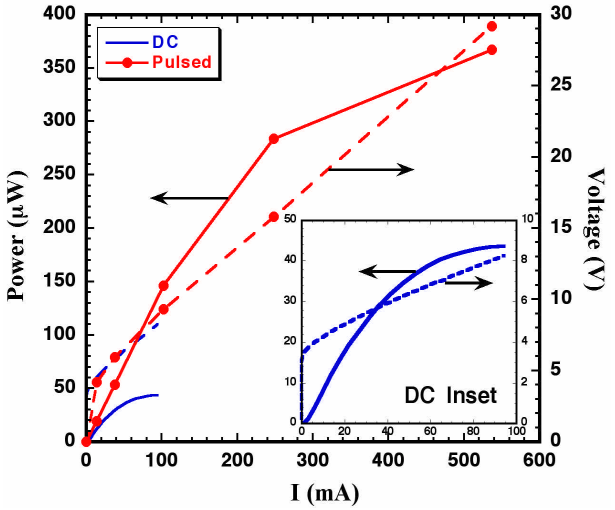

Fig. 12. DC and pulsed LIV measurements on 200 x 200 µm UV LEDs. DC data is expanded in the inset for clarification.

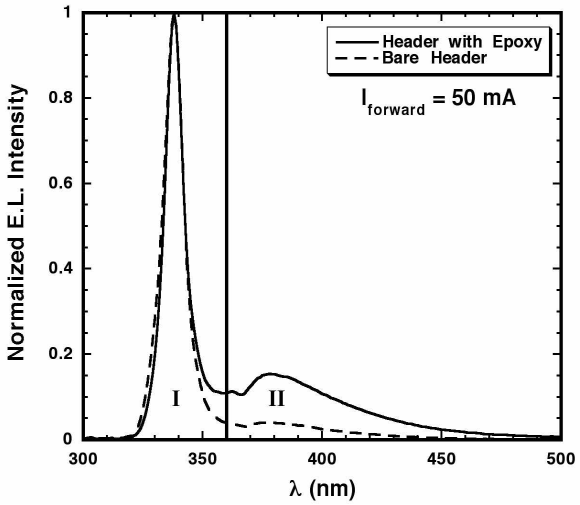

Fig. 13. Electroluminescence spectrum for 336 nm LEDs mounted on a bare header and an epoxy-encapsulated header.

Spectral measurements were taken on devices mounted on bare headers as well as on headers encapsulated in 'conventional' epoxy used for blue and green InGaN-based LEDs. The normalized spectra are shown in Fig. 13, with region I designating the intended emission peak at 336 nm and region II designating the deep level emission commonly observed in UV LEDs. We believe the deep level emission is a result of electron overflow from the active region into the p-type SPASL. This occurs despite having a 150 Å $Al_{0.30}GaN$ electron blocking layer on top of the active region quantum wells. The deep level signal at 378 nm increased relative to the dominant quantum well emission at 336 nm for the epoxy encapsulated device, indicating absorption of the peak wavelength by the epoxy. The fraction of light in the target wavelength range to total light output, α, is defined in the equation below. Over a factor of three increase in α was observed for the bare header (0.157) compared to the header with epoxy encapsulation (0.433).

$$a \equiv \frac{\int_{360}^{300} I(\lambda)\,d\lambda}{\int_{700}^{300} I(\lambda)\,d\lambda}$$ where I(λ) ≡ intensity of the electroluminescence spectrum.

The measured output powers were comparable for the two lamp designs, bare header and epoxy encapsulated header, despite the added extraction efficiency gained by epoxy coating. The epoxy used for encapsulating these devices is typically used for InGaN based green and blue LEDs. Thus it is clear from these data that UV-specific packaging needs to be developed for deep ultraviolet LEDs, such as that being pursued by the LRC/RPI team.

R.2 RCLED Development

One of the principle 'building blocks' in our RCLED structure is a p-GaN contact of sufficiently low resistivity as well as high reflectivity. To this end, we have developed silver (Ag) contacts, which are covered by an overlying Ni/Au layer for oxidation protection. As shown in Fig. 14, the as-deposited Ag contacts have a comparable turn-on voltage to conventional Ni/Au contacts. After rapid thermal annealing (RTA) to activate the p-GaN, the turn-on voltage increased by about 1 V, but the result was still acceptable for device use.

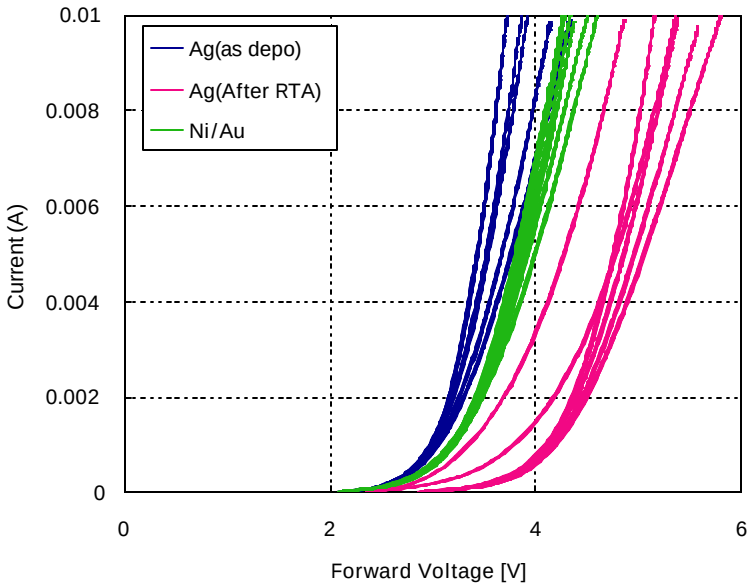

Fig. 14. I-V curves of Ag, annealed Ag, and Ni/Au p-GaN contacts.

The most promising aspect of the Ag mirror/contact development so far has been the measurement of mirror reflectivity over the wavelength range of interest, as shown in Fig. 15. Reflectivity exceeds 95% for wavelengths longer than ~410 nm, and we expect this to improve with further optimization of deposition and annealing conditions.

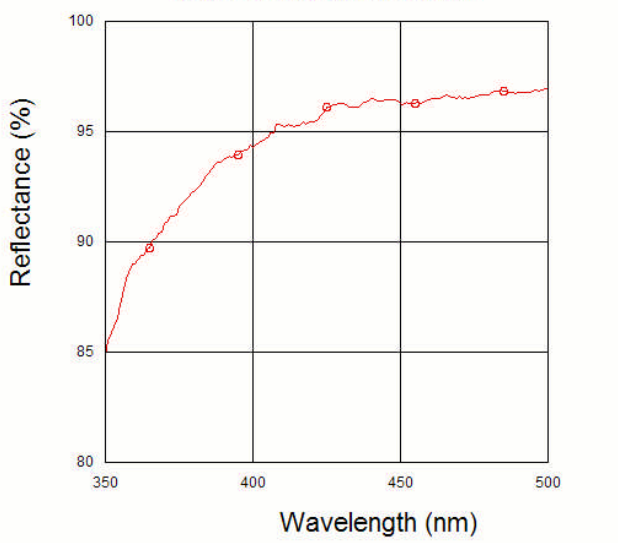

Fig. 15. Reflectance of Ag mirror/contact at various wavelengths.

As mentioned in the Introduction/Experimental section, our initial RCLED structures have consisted of flip-chipped GaN with the sapphire removed and the cavity thinned to leave a GaN/air 'interfacial mirror', as shown in Fig. 16. In this case, thinning was performed with a Ga focused-ion beam (FIB), which allows for carefully controlled etch rate and lateral etch area. When tested under continuous forward voltage, the devices had bright blue emission centered at about 450 nm (Fig. 17), despite the fact that we noticed apparent ion damage from the FIB etch. We will investigate whether ion damage of the active region is unavoidable during FIB etching, and if so, use chemical-mechanical polishing and dry etching exclusively.

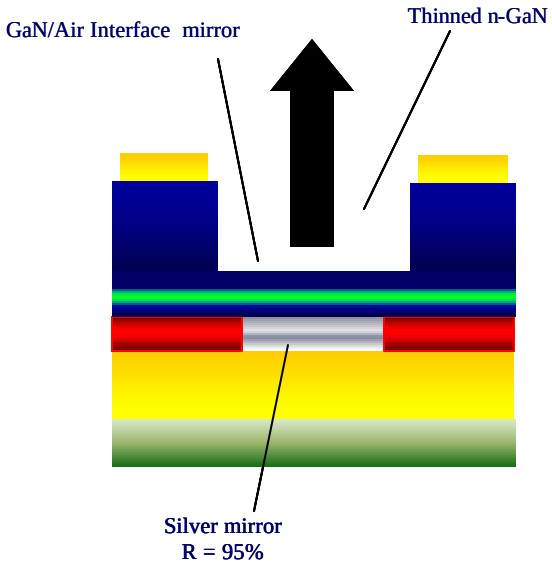

Fig. 16. Schematic of a flip-chipped RCLED with 'interfacial' GaN/air mirror over thinned n-GaN region.

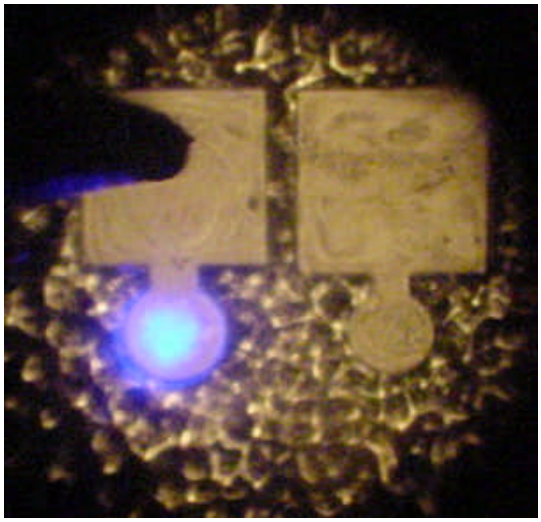

Fig. 17. Photograph of an initial forward-biased RCLED with 'interfacial' top-side mirror.

A typical spectrum from an RCLED with an interfacial mirror is shown in Fig. 18, and for comparison the spectrum emitted from a conventional LED fabricated from the same material is shown in Fig. 19. The primary difference between the two is the presence of small 'lobes' in the RCLED spectrum, which arise due to the emergence of cavity modes in this structure. The spacing of the lobes corresponds to a cavity length of 2.8 μm, in good agreement with the actual value. Future polishing and

etching studies will focus on decreasing cavity length while maintaining a smooth surface in order to obtain more pronounced cavity mode behavior.

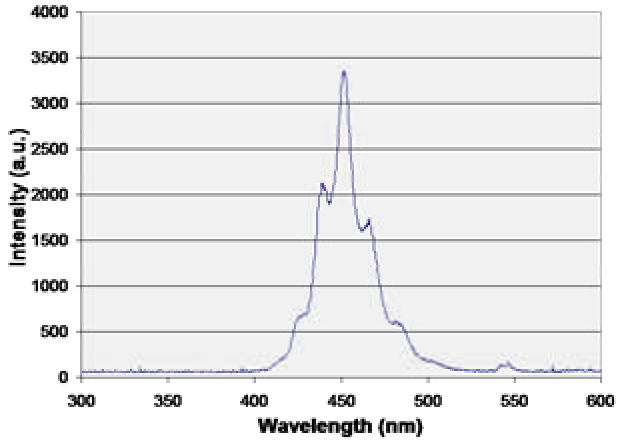

Fig. 18. Electroluminescence spectrum from a flip-chipped RCLED with an interfacial mirror on the n-GaN top side.

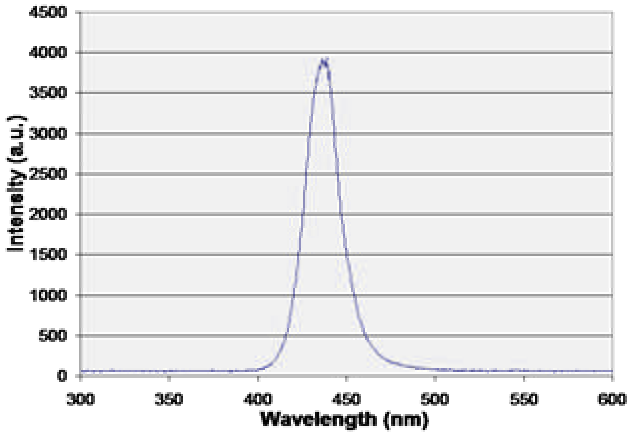

Fig. 19. Electroluminescence spectrum from a conventional LED fabricated from the same material as the RCLED in Fig. 18.

Angular-Dependent Measurements

For initial evaluation purposes, the first sample measured with the angle-resolved measurement setup was a film with a quantum well structure typical of a conventional LED. Since there were no doped regions (p or n-type), the photoluminescence (PL) as excited by a 325nm He-Cd laser was measured as a function of angle. As shown in Fig. 20, the central wavelength of ~420 nm did not shift when recorded at various angles. In addition, the normalized intensity of the LED followed the expected Gaussian profile, as evident in Fig. 21. The PL intensity as a function of both measurement angle and wavelength is shown in Fig. 22.

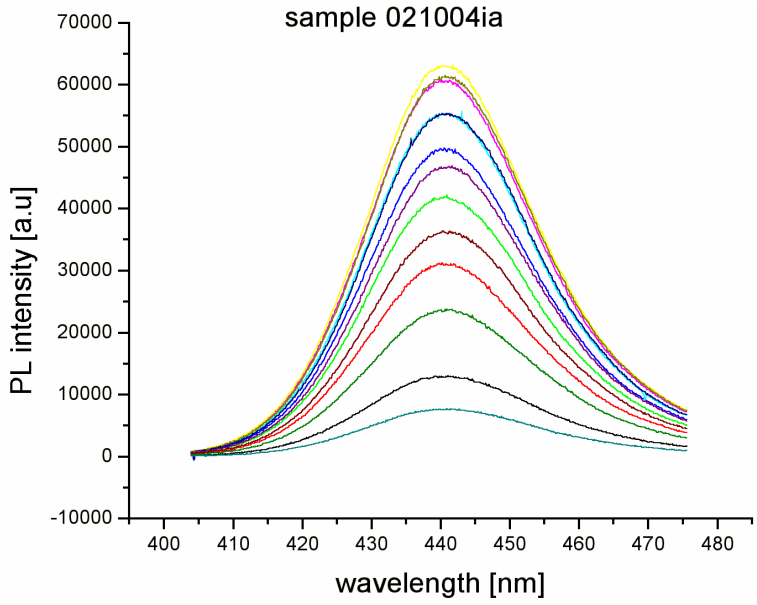

Fig. 20. Spectra from conventional LED QW structure measured at various angles.

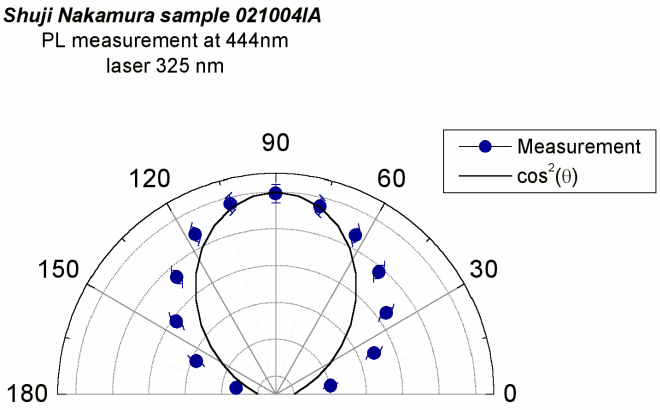

Fig 21. Polar plot of the normalized intensity as a function of the angle, with comparison to the expected Gaussian response of $\cos^2\theta$.

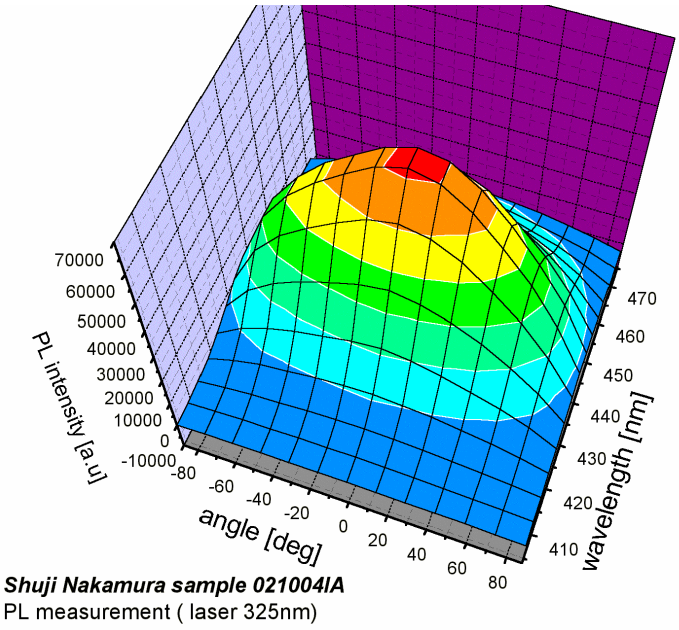

Fig. 22. 3-D intensity plot of the PL spectrum of a conventional LED QW as a function of angle and wavelength.

Once the angular measurement setup was evaluated and calibrated for general use as described above, we proceeded with angular measurement of light emission from RCLED structures. A picture of the electroluminescence of a typical RCLED used for these measurements is shown in Fig. 23 below.

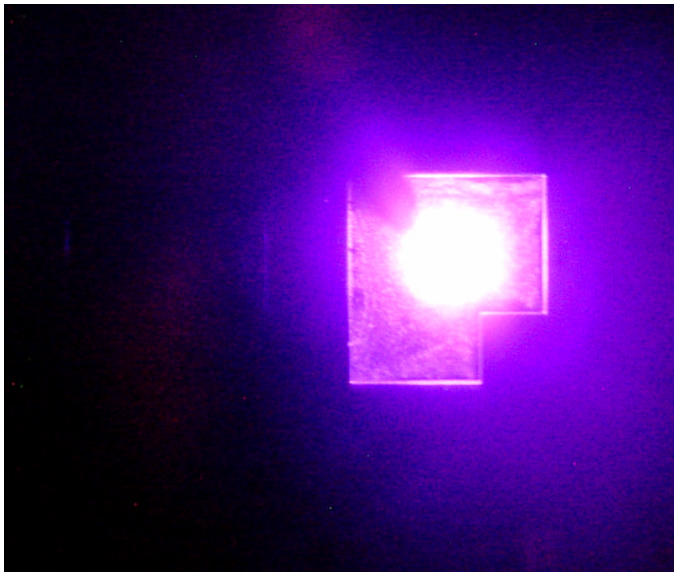

Fig. 23. Electroluminescence from an RCLED tested in this study.

During RCLED processing, the overall film thickness was generally decreased from 5μm to less than 0.5μm using a combination of RIE etching and chemical-mechanical polishing. This thinning was necessary to see Fabry-Perot cavity effects in the RCLED cavity. The EL spectra shown in Fig. 24 below are from a device thinned to about 1.5 μm, yielding a cavity order of 16 for a peak wavelength of ~ 420 nm. The full intensity vs. wavelength-angle data are shown in Fig. 25. Note that the two distinct lobes ("rabbit ears") on either side of the central peak indicate the emergence of the desired microcavity effect.

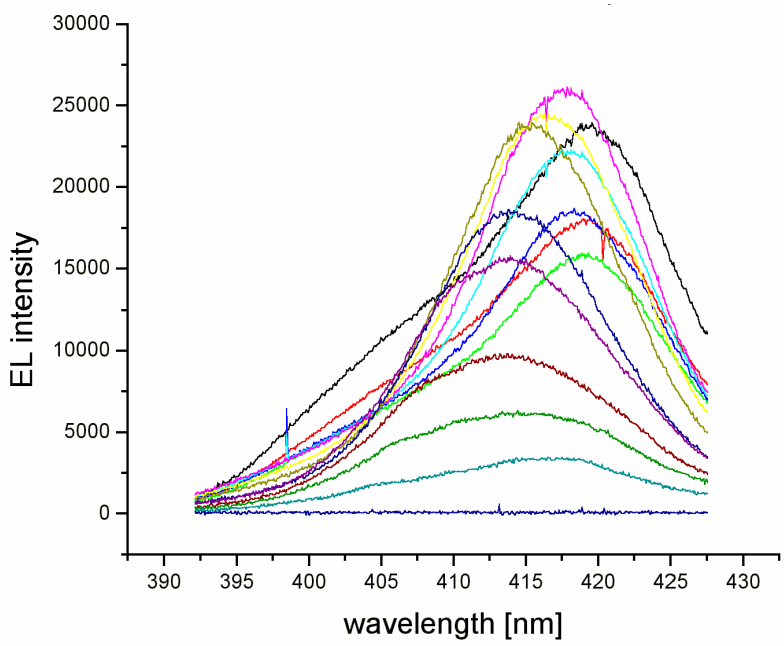

Fig. 24. EL spectra from an RCLED at various angles.

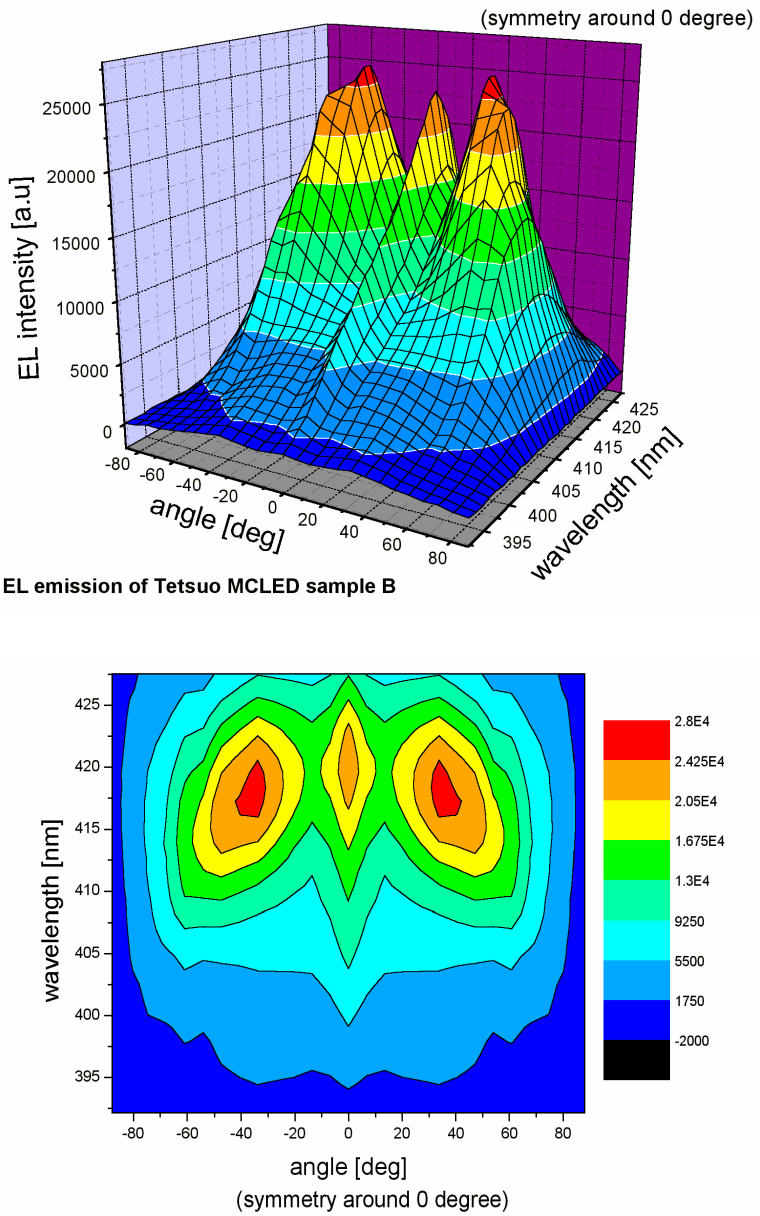

Fig. 25. 3-D (top) and contour (bottom) plots of RCLED EL intensity as a function of wavelength and measured angle. (Note: data were recorded for angles of 0 to 90°, but plotted as symmetric about 0°).

Although the rabbit ears in the plots above indicated the presence of desirable "detuning" (*i.e.* elevated efficiency) in this device, the central peak at normal angle was due to the fact that the cavity order was too high and a second peak was present in the escape cone. This can be easily viewed by considering again the polar representation of the power emitted at the source of the MCLED, as shown in Fig. 26 below.

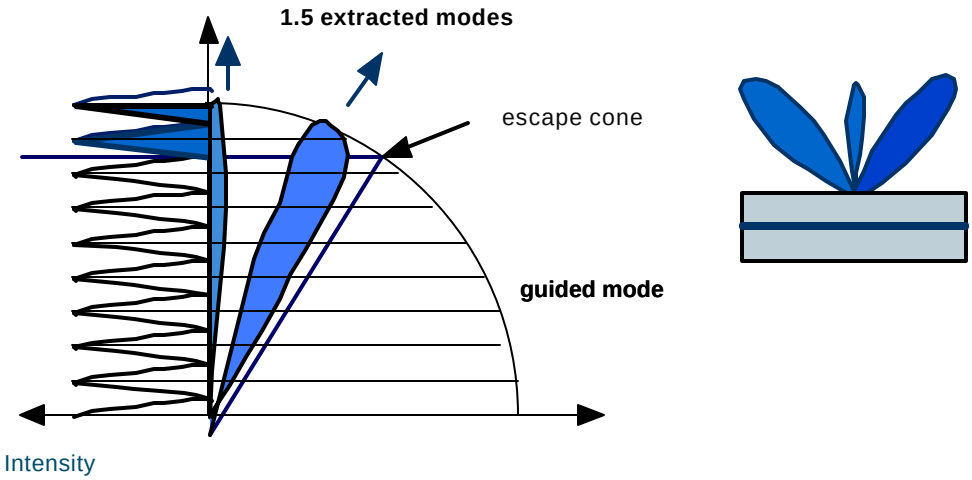

Fig. 26. Polar representation of emitted power from RCLED, showing that 1.25 modes are present in the escape cone.

Almost 1.25 modal peaks fit the extraction cone, thus there is a fully extracted mode at some angle and part of the other mode is extracted at normal incidence. By taking these 1.25 extracted modes into account, the approximate order and the size of the cavity can be calculated. The relationship between the wavelength of the source λ_0 and the wavelength of the cavity λ_{cav} is given by

$$l_0 = l_{cav} \cos q_{0,in}$$

The angular measurement described above yielded $\lambda_0 = 412nm$, so

$$\theta_{0,ext} = 35°$$

which, with the Snell-Descartes law $[n_{in} \sin(\theta_{0,in}) = \sin(\theta_{0,iext})]$ $\theta_{0,in} = 13.3°$

$$l_{cav} = \frac{l_0}{\cos(13.3°)} \sim 431nm$$

thus the detuning of the device is: $d = l_0 - l_{cav} = -19nm$, which is close to the calculated 'optimal' detuning of -17nm.

Since we have: $l_{cav} = \frac{2n_{in}L}{m_c}$, then:

$$\boxed{\frac{L}{m_c} \approx 86nm}$$

Thus for a cavity order m_c of 16, the calculated cavity length L is 1.38µm, which agrees relatively well with the target value of 1.5µm, as measured by SEM.

R.3 A-plane GaN Lateral Overgrowth by MOCVD

As we have shown for laterally overgrown c-plane GaN, the crystallographic orientation of the mask stripe openings dictate the facets that form, and hence the characteristics of the lateral overgrowth.[14] To investigate the orientation dependence of the laterally overgrown a-GaN, the SiO_2 mask was patterned with an array of rectangular mask openings (windows) which formed a "wagon wheel" design. The windows that made up the wagon wheel pattern were 5 μm wide and oriented in 5° intervals so that a range of crystallographic mask orientations could be analyzed in a single MOCVD growth run. This experimental design is similar to that employed for the initial investigations of laterally overgrown c-plane GaN from linear mask openings.[14,15]

The reduced symmetry of the a-GaN surface (with respect to the c-GaN surface) was apparent in the stripe orientation dependence shown in Fig. 27, a 180° view of a single wagon wheel pattern. Primarily, this plan-view SEM image shows that lateral overgrowth occurred for all possible stripe orientations. Upon closer inspection, three stripe orientations had uniform morphologies without faceted sidewalls: parallel to $[0001]$, 45° off, and perpendicular $[\bar{1}100]$ to the GaN c-axis. The stripes oriented 45° off the c-axis are indexed as $[\bar{1}101]$ stripes since this crystallographic direction makes a 46.8° angle with the c-axis. Figure 27 shows that as the stripe orientation changed from $[0001]$ to $[\bar{1}100]$, the stripe width increased until a maximum width was reached for stripes aligned 70° off the c-axis. After reaching this maximum, the stripe width decreased until it reached $[\bar{1}100]$. Note that we self-consistently use specific crystallographic indexing throughout this section due to the reduced symmetry of this film/substrate system in comparison to c-GaN.

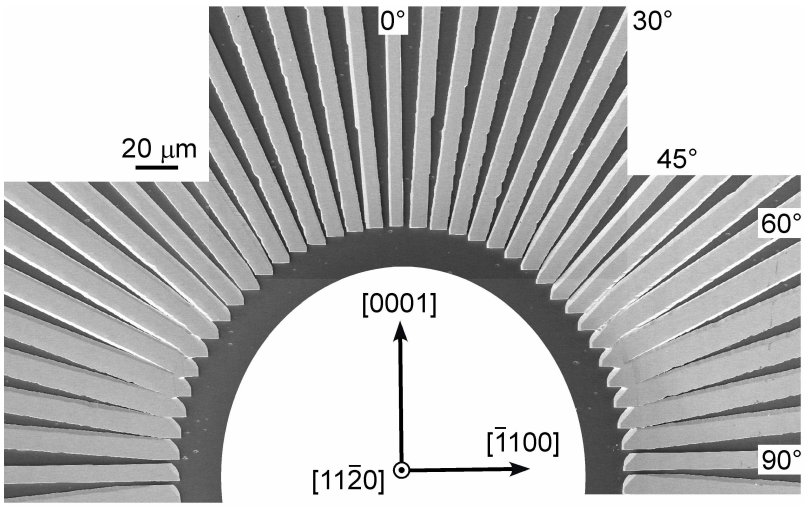

Fig. 27. Plan-view SEM montage showing half of an a-GaN LEO wagon wheel pattern. The angles are included to facilitate reference to the wagon wheel pattern, where 0° corresponds to the GaN c-axis $[0001]$.

An additional perspective is required to clearly observe the effects of stripe orientation on a-GaN LEO morphology. Figure 28 shows a series of SEM images with inclined views of the three stripe orientations introduced above. For the growth conditions employed, $[0001]$ and $[\bar{1}101]$ stripes had various combinations of inclined and vertical sidewalls. Symmetric morphologies were observed for the $[0001]$ stripes while the $[\bar{1}101]$ stripes had asymmetric morphologies with one micro-faceted vertical $(1\bar{1}02)$ sidewall and one inclined $(10\bar{1}2)$ sidewall. The $[0001]$ stripes had coexisting vertical and inclined facets from the same crystallographic family of $\{10\bar{1}0\}$ planes. Conversely, $[\bar{1}100]$ stripes had rectangular cross sections with vertical (0001) basal plane sidewalls. Overall, $[0001]$ and $[\bar{1}100]$ stripe orientations yielded uniform, symmetric morphologies.

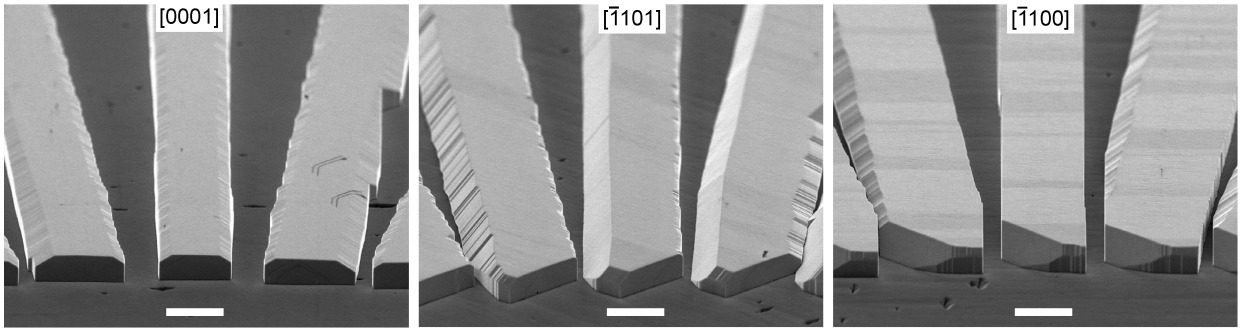

Fig. 28. SEM images of stripes oriented parallel to [0001], [$\bar{1}$101], and [$\bar{1}$100]. The images correspond to the 0°, 45°, and 90° orientation labeling in Fig. 14 (scale bar = 5 μm).

Threading dislocation reduction was observed for LEO stripes aligned along [$\bar{1}$100], as shown in the cross-section TEM image in Fig. 29(a). Mask blocking is the primary dislocation reduction mechanism since no dislocations were observed to bend in the direction of the lateral overgrowth, Fig. 29(b). Unlike [$\bar{1}$100] stripes, Fig. 29(c) shows that dislocations propagated into the overgrown regions of stripes aligned along [0001]. Although the precise origin of this dislocation bending is not yet known, the presence of inclined facets for the [0001] stripe orientation likely plays a key role, due to their exertion of an 'image' force on vertically propagating dislocations. In addition to TD reduction, Fig. 16(a) reveals an asymmetry in lateral overgrowth rates for [$\bar{1}$100] stripes. The existence of polar c-plane sidewalls explains this asymmetry. With the polar axis perpendicular to the stripe direction, one sidewall is the +c-plane or Ga-face while the opposing sidewall is the –c-plane or N-face. As expected, the Ga-face sidewall grew faster than the N-face sidewall by a factor of ~10, depending on the growth conditions. Note that we have previously determined the polarity of a-GaN on r-sapphire using convergent beam electron diffraction (CBED) measurements.[13] Since polarity had such a significant effect on the lateral overgrowth of the [$\bar{1}$100] stripes, some of the asymmetric morphologies observed in Figs. 27 and 28 may be explained in terms of polarity.

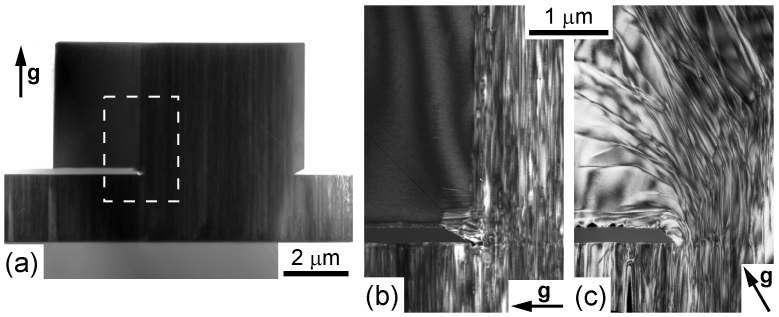

Fig. 29. Cross-sectional TEM image of a [$\bar{1}$100] stripe **(a)** which clearly shows threading dislocation reduction in the asymmetric overgrowth regions. Magnified views of the mask edge region defined by the dashed box on part (a) are shown for **(b)** [$\bar{1}$100] and **(c)** [0001] stripes.

Additional evidence of the lateral overgrowth asymmetry for polar GaN was supplied by plan-view panchromatic CL images of [0001], [$\bar{1}$101], and [$\bar{1}$100] LEO stripes. The CL images shown in Fig. 30 directly correspond to the stripes imaged by SEM in Fig. 28. The mottled regions within each stripe orientation define the openings in the SiO_2 growth mask where threading dislocations have extended unimpeded to the top surface of the LEO stripe. This CL characteristic has been observed in polar GaN LEO stripes.[16-18] The mottled area extends across the entire width of the [0001] stripe, which corresponds to the TEM observation of dislocation bending into the laterally overgrown regions for this stripe orientation. Even though the [0001] stripe shown in Fig. 28 had little lateral overgrowth, CL measurements of wider stripes grown under similar conditions confirmed the dislocation bending observed in Fig. 29(c). The uniform luminescence from the overgrown regions of [$\bar{1}$100] stripes

confirms that those areas are relatively free of threading dislocations. The effects of polarity on the lateral overgrowth rates of $[\bar{1}100]$ stripes are also clearly observed.

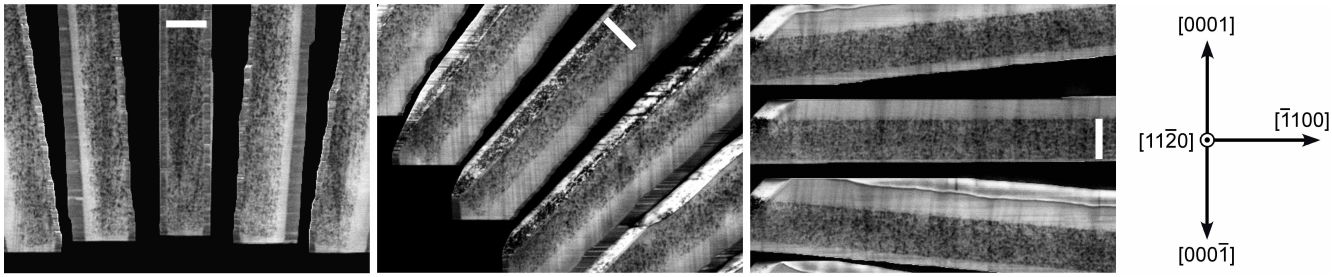

Fig. 30. Plan-view panchromatic CL images of stripes oriented parallel to [0001], $[\bar{1}101]$, and $[\bar{1}100]$. The images directly correspond to the stripes imaged by SEM in Fig. 5 (scale bar = 5 µm).

R.4 A-plane GaN Lateral Overgrowth by HVPE

Figure 31(a) shows a Nomarski optical contrast micrograph of a 20 µm-thick coalesced LEO film formed by $[10\bar{1}0]$-oriented stripes. The faint "fish scale"-like feature on the right side of the image demonstrates that the film's surface is in focus, while the refractive index contrast from the SiO_2 allows the out-of-focus mask pattern to be observed. Similar, near-featureless surfaces are observed for masks consisting of arrays of circular apertures. Atomic force microscopy (AFM) was performed to compare the surface quality in the window and wing regions of the *a*-plane LEO films. Figure 31(b) shows a 40 x 40 µm AFM micrograph spanning multiple stripes. The window region appears as the band of heavily pitted material, with the coalescence front a few micrometers to the left of the windows. This pitted region is shown in detail in Fig. 31(c). The broad, light band between the pitted regions is the Ga-face wing, enlarged in Fig. 31(d). The overgrown material exhibits virtually no pitting and surface roughness on the order of 0.7 nm.

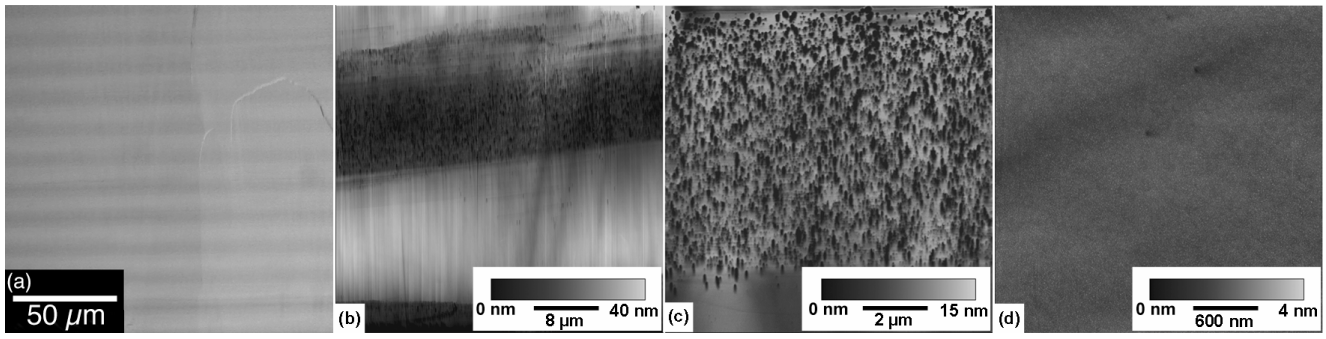

Fig. 31. **(a)** Nomarski optical contrast micrograph of a coalesced LEO *a*-plane GaN film. The stripes are oriented along the $[10\bar{1}0]$ direction. **(b-d)** AFM images of coalesced $[10\bar{1}0]$-oriented GaN stripes: (b) 40 x 40 µm image showing the relative surface quality of the window and wing regions. **(c)** Magnified view of the window region. **(d)** Magnified view of the overgrown region.

Figures 32(a) and (b) are cross-sectional SEM images of LEO wafers patterned with a periodic array of $[10\bar{1}0]_{GaN}$- oriented SiO_2 stripes. Figure 32(a) demonstrates the sharply vertical {0001} sidewalls that are prevalent for $[10\bar{1}0]$-oriented stripes, and Fig. 32(b) shows an inclined cross-sectional view of three coalesced GaN stripes. The two arrows point to sub-micron voids that are frequently observed at the wing-mask interface at the coalescence front. These voids are observed to result when $\{11\bar{2}2\}$ facets form on the lower edges of the Ga-face (0001) planes within the last 1 µm of lateral growth, possibly

due to a mass transport-limited local shift in the V/III ratio. Fig. 32(c) is a plan-view SEM image of a coalesced film, again with a mask of SiO_2 stripes oriented along the GaN $[10\bar{1}0]$ direction. The surface is flat and almost featureless, except for a few faint irregular ridges. These ridges manifest themselves in the corresponding cathodoluminescence (CL) image in Fig. 32(d) as dark lines due to scattering. Figure 32(d) is a monochromatic CL image of the surface in Fig. 32(c) imaged at 365 nm, with lighter shades of grey indicating greater luminous intensity. The window regions in the CL image are apparent as the dark horizontal bands. Higher-magnification CL images allow the fast-growing Ga-face [0001]-advancing wing to be distinguished from the slow-growing N-face $[000\bar{1}]$-advancing wing, as the Ga-face wing tends to grow approximately 8-12 times as fast as the N-face wing. As a result, the coalescence front resides within 1-2 μm of the windows and provides little defect-free surface area. The narrow, dark stripes oriented along the <0001> direction do not appear to correspond to surface features. The cause of this decreased luminescence is a point of ongoing investigation.

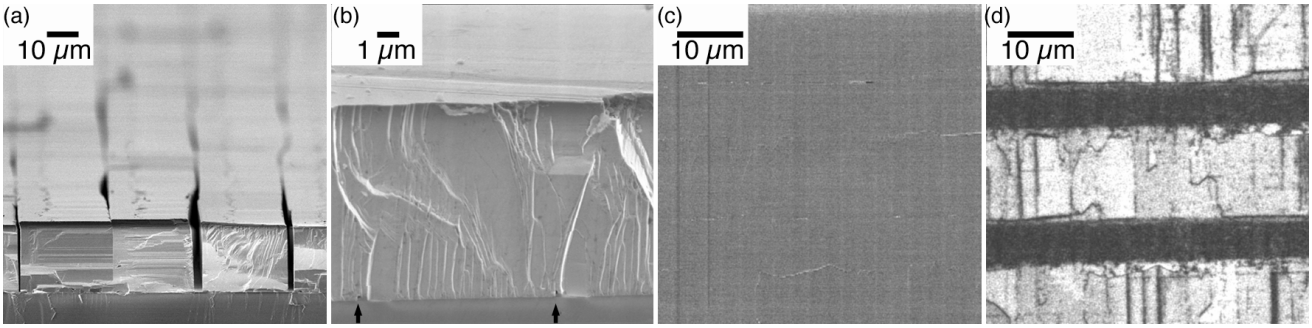

Fig. 32. (a) Cross-sectional SEM image of parallel LEO stripes approaching coalescence. **(b)** Cross-sectional SEM image showing coalesced stripes. The arrows mark sub-micron voids at the wing-mask interface where the stripes coalesced. **(c)** Plan-view SEM image of the coalesced region pictured in **(d)**, which is a monochromatic CL image of the region shown in **(c)** at 365 nm. The mask in each case consisted of parallel SiO_2 stripes along the GaN $[10\bar{1}0]$ direction.

The structural quality of the *a*-plane LEO films was characterized by x-ray diffraction (XRD) and TEM. X-ray rocking curves of the $11\bar{2}0$ GaN reflection taken perpendicular to the LEO stripe direction were single-peaked, indicating a lack of measurable tilt in the coalesced films. Furthermore, narrowing of both on- and off-axis reflections was observed in the LEO films compared to planar *a*-plane GaN films grown directly on *r*-plane sapphire. Typical full widths at half maximum for the $11\bar{2}0$ and $10\bar{1}0$ reflections were 0.21° and 0.35°, respectively. Figure 33 shows cross-sectional and plan-view TEM images of a coalesced a-plane LEO film. In good agreement with observations from AFM and CL, the window regions have high threading dislocation ($\sim 9 \times 10^9$ cm^{-2}) and stacking fault ($\sim 4 \times 10^5$ cm^{-1}) densities. In contrast, the overgrown regions appear to be largely free of both dislocations and stacking faults, indicating a reduction in extended defect density of at least four orders of magnitude.

The above results have demonstrated that substantial reduction in morphological and structural defects in *a*-plane GaN may be readily achieved by LEO with hydride vapor phase epitaxy. The reduction in threading dislocation density in the overgrown GaN is accompanied by a significant improvement in surface morphology compared to planar *a*-plane GaN. Coupling LEO with the comparably high growth rates achievable by HVPE bodes well for the fabrication of free-standing, high-quality non-polar GaN substrates.

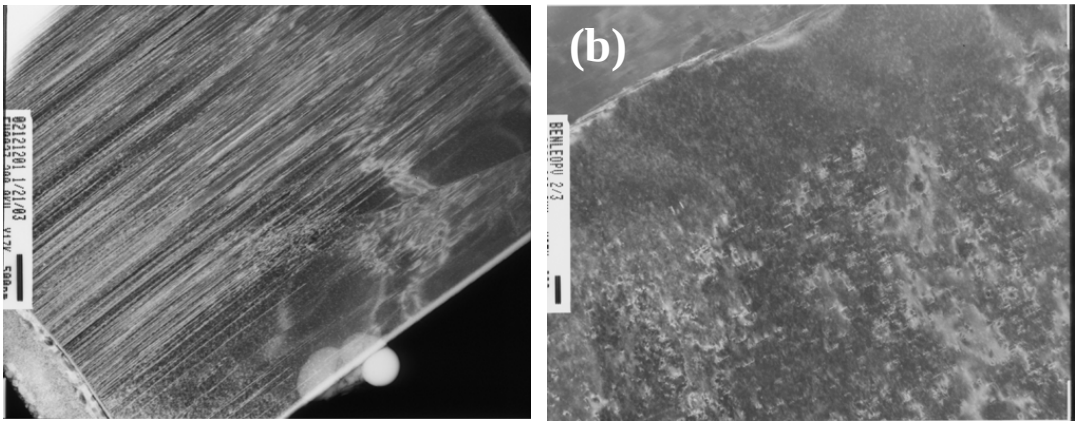

Fig. 33. **(a)** Cross-sectional TEM image of an *a*-GaN LEO stripe. **(b)** Plan-view TEM image.

R.5 Benchmark of current state-of-the-art LED devices

LED performance and degradation can vary significantly depending on how the devices are packaged and driven, as well as the ambient temperature during operation. Based on past literature and what we have observed in the LRC lab, junction temperature has the greatest influence on performance and degradation. The amount of power supplied to the LED and ambient temperature surrounding the LED contribute to junction heat. Therefore, this benchmarking study evaluated selected high-power LEDs under two drive currents and two ambient temperatures and the resulting changes in light output, efficacy, and color.

Relative light output as a function of time

Figure 34 illustrates the light output change as a function of time for five types of high-flux LEDs at three operating conditions. Table 2 shows the average board temperatures and the corresponding junction temperatures of the different LEDs at the three operating conditions. At the first operating condition—350 mA and 35ºC— the Shark white and the Luxeon blue LED arrays had the highest light output loss, approximately 10% during the 4,500-hour period. The Luxeon green and the Shark white arrays had similar degradations of approximately 4%.

At the second operating condition—350 mA and 50ºC—where the drive current was similar to the first condition but the ambient temperature was higher, the Luxeon blue, Shark white, Luxeon red, and Luxeon white arrays experienced approximately 25%, 23%, 10%, and 8% light loss, respectively, at the end of the 4,500-hour period. However, the Luxeon green arrays experienced very little light loss, less than 5%. As seen in Table 2, all of the LED arrays at this operating condition had the highest board temperatures, approximately 53ºC, except for the Shark white LED array (58.3 ºC).

At the third operating condition—450 mA and 35ºC—where the ambient temperature was similar to the first condition but the drive current was higher, the Luxeon red and the Shark white arrays experienced light losses of approximately 19% and 15%, respectively. However, the Luxeon green and Luxeon blue arrays experienced a light loss of less than 2%. One Luxeon blue array showed a slight increase in light output during its initial 1,200-hour period. This particular array had a higher peak wavelength than the other two samples tested. Furthermore, this array had the highest junction temperature compared with the other two blue LED arrays, yet showed better lumen maintenance up to this point.

Overall, the Luxeon green and white arrays showed very little light loss after 4,500 hours, even though the current and the ambient temperature were increased. The Shark white LEDs seem to have the highest overall degradation. The light output fluctuation, especially at the first 1,000 hours, was caused

by a failure of the room's air conditioning, which led to the fluctuation of the testing chamber's temperature and therefore, changes in light output.

Table 2: Average board temperature and estimated junction temperature of each LED array tested.

LED Type	Operating Condition	Measured Board Temperature °C	Estimated Junction Temperature °C
Red	350 mA, 35°C	41.3	62.1
Red	350 mA, 50°C	52.1	73.6
Red	450 mA, 35°C	48.0	79.7
Green	350 mA, 35°C	42.4	61.8
Green	350 mA, 50°C	52.4	71.5
Green	450 mA, 35°C	46.4	72.6
Blue	350 mA, 35°C	43.8	64.6
Blue	350 mA, 50°C	52.7	72.9
Blue	450 mA, 35°C	49.8	75.3
Luxeon White	350 mA, 35°C	42.9	62.8
Luxeon White	350 mA, 50°C	53.2	73.9
Luxeon White	450 mA, 35°C	48.2	76.5
Shark White	350 mA, 35°C	52.2	76.6
Shark White	350 mA, 50°C	58.3	82.4
Shark White	450 mA, 35°C	72.8	107.6

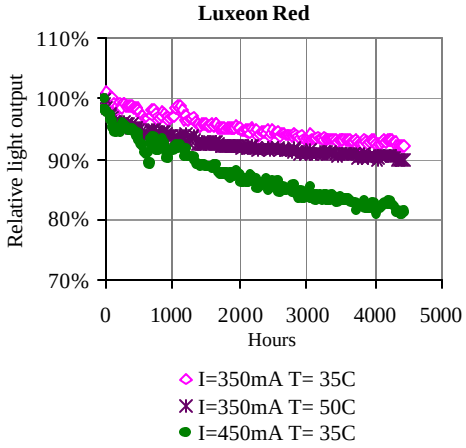

(a)

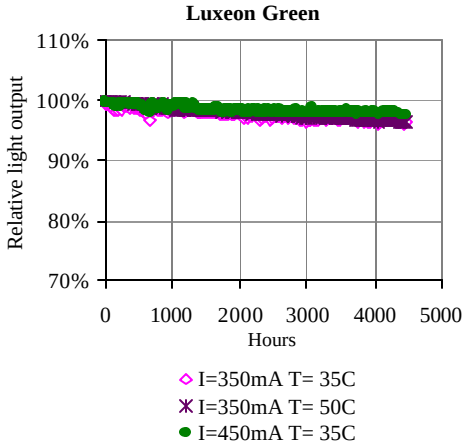

(b)

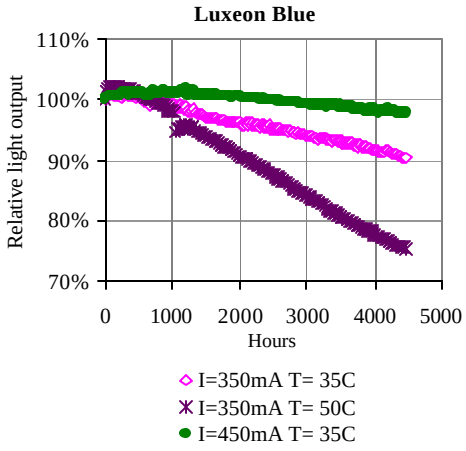

(c)

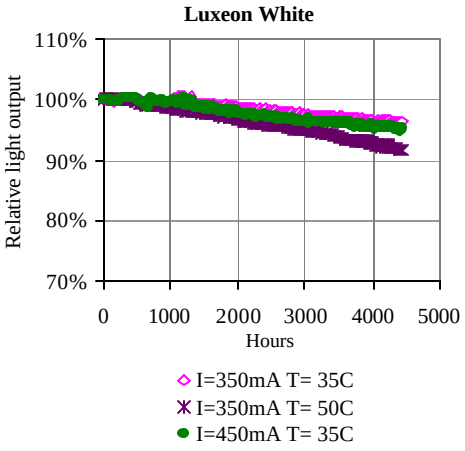

(d)

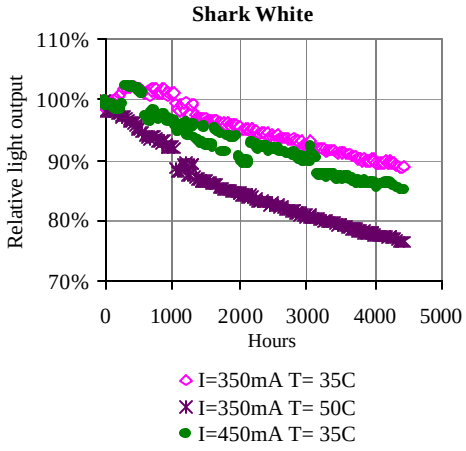

(e)

Fig. 34. Relative light output as a function of time for (a) Luxeon red LEDs, (b) Luxeon green LEDs, (c) Luxeon blue LEDs, (d) Luxeon white LEDs, and (e) Shark white LEDs.

Relative system efficacy as a function of time

Similar to the light output degradation, the Shark white had the highest overall efficacy drop during this testing period. Conversely, the Luxeon green and Luxeon white LEDs had the smallest efficacy decrease (Fig. 35, below).

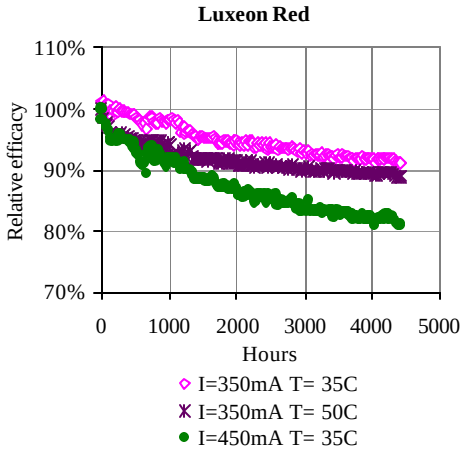

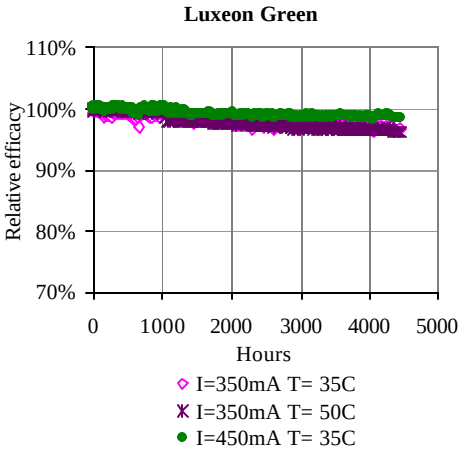

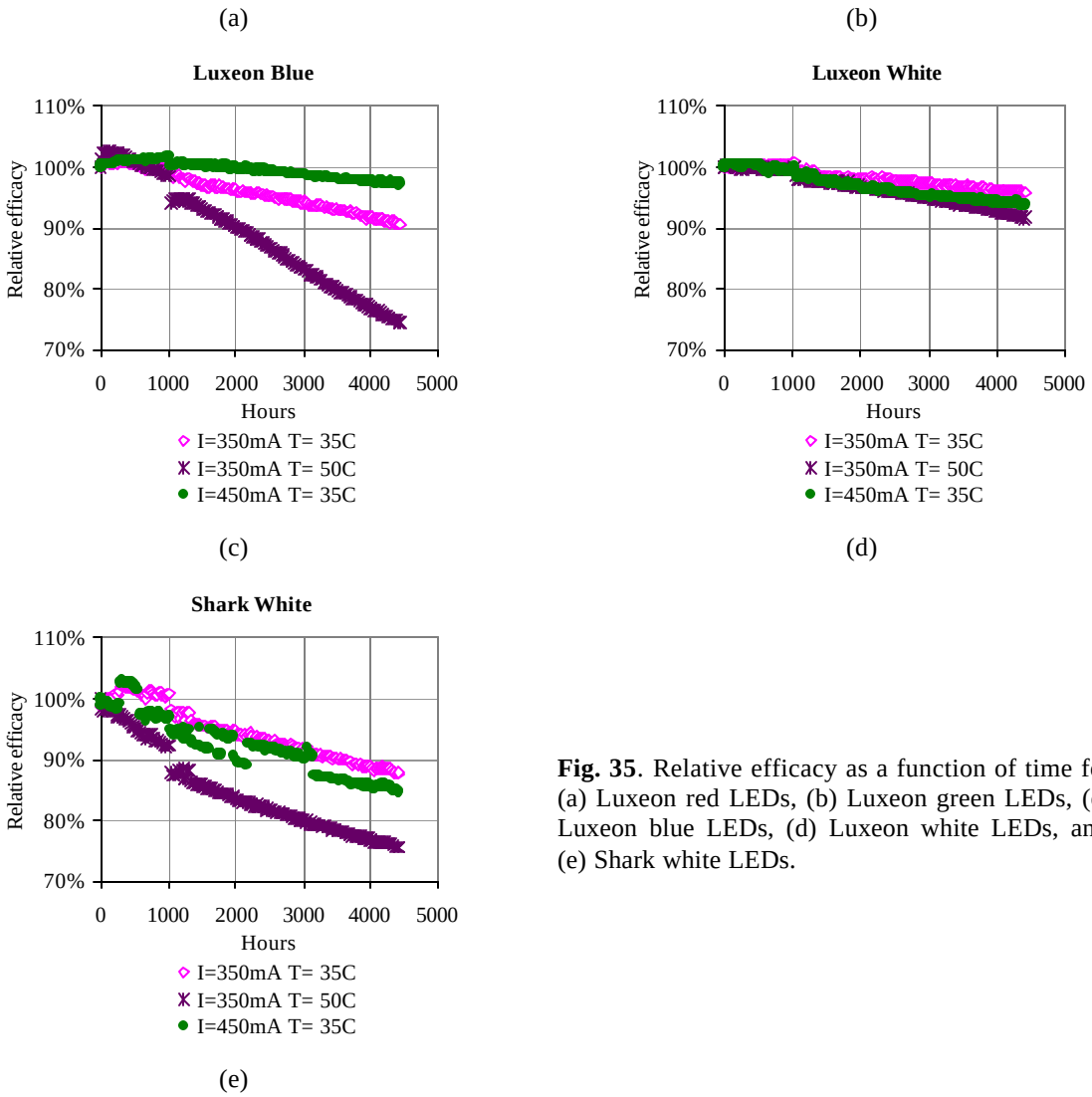

Fig. 35. Relative efficacy as a function of time for (a) Luxeon red LEDs, (b) Luxeon green LEDs, (c) Luxeon blue LEDs, (d) Luxeon white LEDs, and (e) Shark white LEDs.

Photometric characteristics

Figure 36 illustrates the CIE x,y values of the individual white LEDs after 0, 1,000, and 2,000 hours of continuous operation. The white LEDs still had significant color variations (of the order of a 12-step MacAdam ellipse) among them. Luxeon white LEDs showed more color variation between products compared with the Shark LEDs. However, the color shift over time was very small.

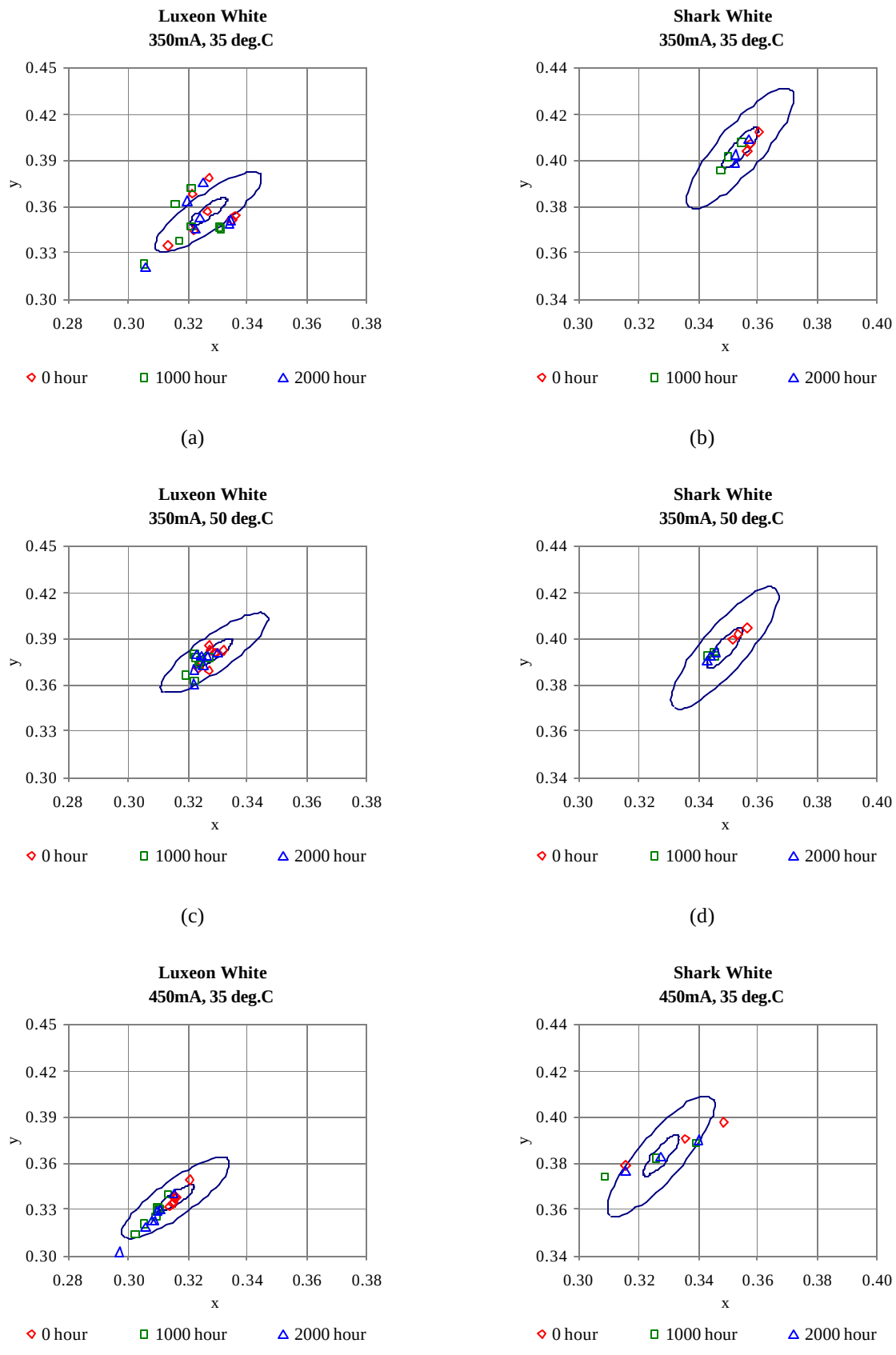

Fig. 36. CIE x,y values of the individual white LEDs after 0, 1000, and 2000 hours.

Summary

Overall, the green and Luxeon white arrays showed very little light loss after 4,500 hours, even when the current and the ambient temperature were increased much above normal operating conditions. However, the Shark white LED array seemed to have a high degradation rate. Although the degradation rate appeared to increase with increasing junction temperature for most LEDs within each LED type, it is too early to generalize. Many previously published studies indicate that junction heat is one of the primary causes of LED degradation. It is worth noting here that for a given junction temperature, the degradation rate will be different for the different types of LEDs. As an example, the results from this study show that at a junction temperature around 70ºC, the degradation rates for the Luxeon white and the green LEDs are similar and low; however, for the red and the blue LEDs, they are much higher. Moreover, the efficacy depreciation for each array is similar to the corresponding light output degradation.

Based on the results, it appears that the white LEDs would maintain greater than 70% light at 100,000 hours. This sets the target for the RCLED white light source that is being developed in this project.

The white LEDs showed significant color variations (of the order of a 12-step MacAdam ellipse) between each individual LED. However, the color shift over time was very small. For white LEDs to be accepted broadly for general illumination applications, the color variation between similar products must become much smaller, of the order of a 2-step MacAdam ellipse, in order to match the performance of linear fluorescent lamps available at the present time. Until manufacturing processes improve to provide consistent color between similar LEDs, color binning is one option for creating arrays with unnoticeable color variation.

In addition to monitoring the light output of white light devices, additional work was carried out to predict junction temperature of white LEDs based on spectral power distribution. The results showed that by taking the ratio of the total energy of the white light emission and dividing it by the energy in the short wave length emission can predict junction temperature. If junction temperature can be shown to relate to degradation of white LEDs then the need for long term life tests can be eliminated.

Future work

Continue to Benchmark Current State-of-the-Art White LED Devices

The LRC will continue the life-test for approximately 10,000 hours and then benchmark performance for state-of-the-art white LED technology, including efficacy, color characteristics, spectral power distribution, and lumen maintenance.

Identify parameters to predict LED performance

The LRC will try to identify predictors such as junction temperature to project system life. This can significantly reduce the time needed to characterize LEDs in the future and would eliminate the need for long-term life tests. Once the RCLEDs under development in this program are ready for life-tests, a similar procedure will be used for testing. Predictors will be identified so that performance can be quantified and improved rapidly without the long wait for life-test results.

R.6 RCLED Packaging Issues – *Phosphor Placement*

Past studies have shown that the light output degradation of white LEDs caused by the yellowing of the epoxy depends on two factors: the heat at the p-n junction and the amount of short-wavelength radiation. However, it has been observed that the 5 mm type phosphor-converted white LED degrades faster than the similar type of blue LED. If heat and the amount of short-wavelength radiation were the only reasons for the yellowing of the epoxy, then the blue LED should degrade faster than the white LED because the total amount of short-wavelength radiation will be much higher for the blue LED compared with the white LED at the same drive current. The main difference between a 5 mm type blue and a similar white LED is the phosphor that is mixed in with the epoxy. Literature supports the stability of phosphors over time; thus, phosphor degradation was not expected nor studied. Therefore, this study was designed to determine whether the location of phosphor could be the reason for the excess degradation.

Relative light output as a function of time

Figure 37 illustrates the relative light output of the six LED arrays tested as a function of time. As hypothesized, the white LED array had the highest depreciation rate while the blue and blue-plus-phosphor arrays had lower depreciation rates. As it can be inferred from the plot, the LEDs with the phosphor layer close to the die degraded faster.

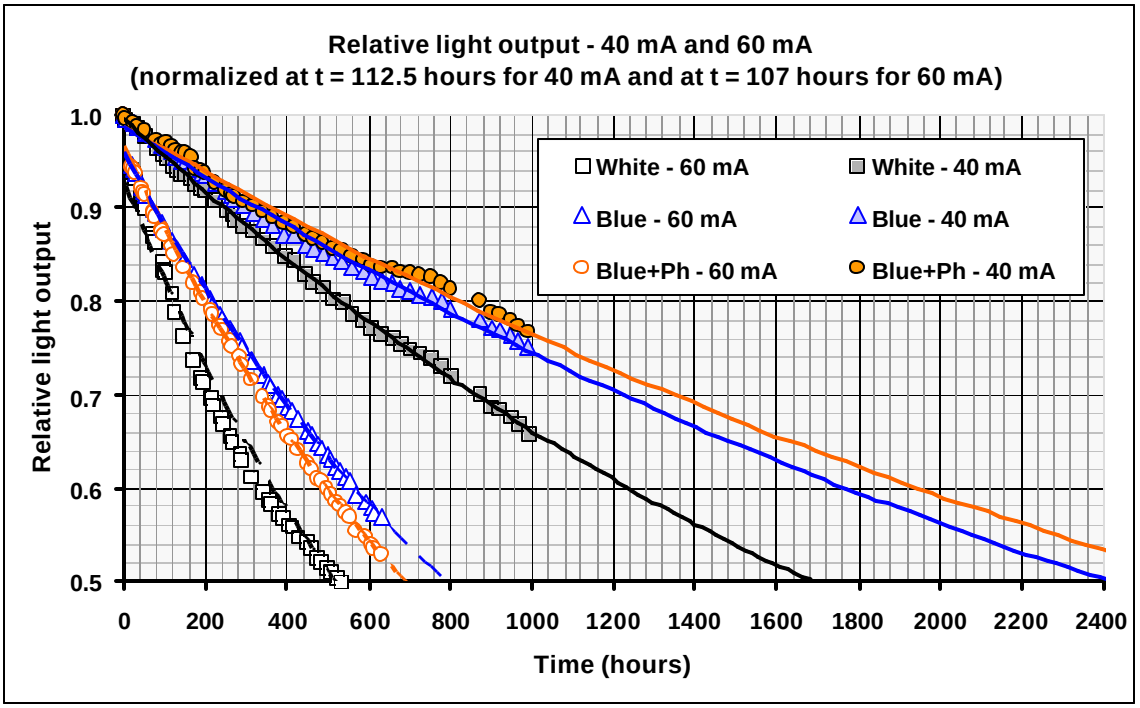

Fig. 37. Relative light output as a function of time of white LEDs, blue LEDs and blue-plus-phosphor LEDs arrays for 40 mA and 60 mA drive currents.

Figure 38 illustrates the estimated junction temperature of the LED arrays as a function of time for the two drive current conditions. These values were calculated from measured LED lead temperatures. As expected, this graph shows higher junction temperatures for white LEDs at both drive currents, with the blue-plus-phosphor arrays in second place. The average difference in junction temperature between white and blue-plus phosphor arrays was 5.5ºC at 40 mA and 4.2ºC at 60 mA. This and other ongoing

experiments at the LRC have shown that although junction temperature and amplitude of short-wavelength radiation influenced the yellowing of the epoxy—and hence, the light output degradation rate of these types of white LEDs—the junction temperature had a much greater effect than the short-wavelength amplitude. These results seem to support the hypothesis that the closer the phosphor medium is to the die, the more light will be reflected to the die, increasing the temperature of the junction.

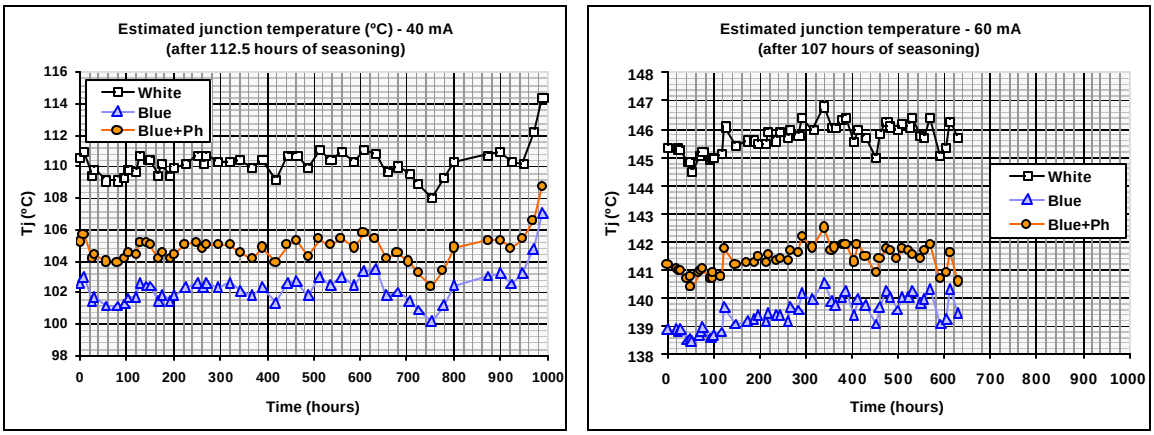

Fig. 38. Estimated junction temperature as a function of time for white LEDs, blue LEDs, and blue-plus-phosphor LEDs arrays for 40 mA and 60 mA drive currents.

Moreover, a possible explanation for the additional degradation of white LEDs is that the phosphor particles mixed into the epoxy emit light isotropically and also scatter the unconverted short-wavelength light. Therefore, at any given time only a fraction of the light will travel outward from the phosphor layer; the balance is redirected toward the phosphor layer, the reflector cup, or the die. Since the radiant energy travels through the epoxy region of the white LED more often than in the blue LED, the epoxy would yellow more.

Relative system efficacy as a function of time

The power consumption of the six LED arrays remained within 0.39% of the initial value (median: 0.08%) at 40 mA and within 1.15% of the initial value (median: 0.35%) for 60 mA. Therefore, the efficacy of the LEDs changed only as a function of and with the same magnitude as the light output (see Figure 37).

Photometric characteristics

Figure 39 shows the change in CIE x,y coordinates of the six arrays as a function of time. Each chart shows four x,y measurements, representing the starting, ending, and two intermediate points during the testing period. For either drive current, the white LED arrays and the blue-plus-phosphor arrays exhibit the largest color shift, approximately a 7-step MacAdam ellipse. The three arrays showed color shifts of similar magnitude from 40 mA to 60 mA, increasing to approximately a 16-step MacAdam ellipse. Note, however, that there is no MacAdam ellipse reference for coordinates close to those representing the blue LEDs. These results are consistent with the light output depreciation trends, since the color shift is due primarily to the yellowing of the epoxy.

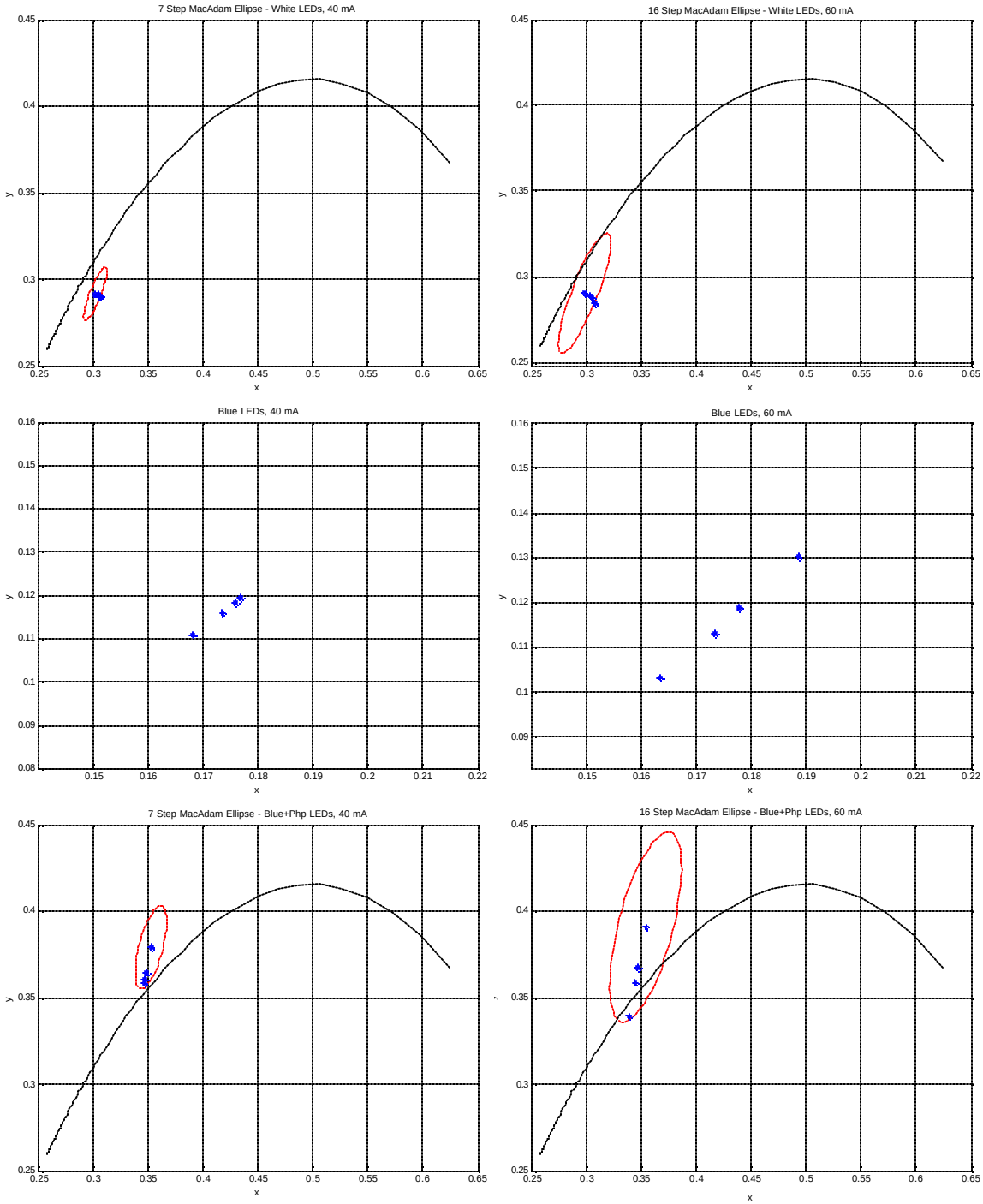

Fig. 39. CIE x,y coordinates of white (top), blue (center) and blue-plus-phosphor (bottom) LED arrays for 40 mA (left) and 60 mA (right) drive currents. The ellipses are centered at the initial x,y value (t=0 hours). The data close to the perimeter of the ellipses represent measurements at t=1100 hours for 40 mA and t=650 hours for 60 mA.

Summary

The results obtained thus far show that the lumen maintenance of white LEDs can be improved by using epoxy materials that have lower photo-degradation characteristics, by extracting the heat more efficiently from the die to keep it cooler, and by not placing the phosphor layer very close to the die. Currently, some commercially available white LEDs have exploited the first two facts and have shown

dramatic improvements in lumen maintenance[19,20]. It is worth emphasizing that in RCLEDs, the effect of the phosphor location would be of larger proportions, since the light output distribution is much more concentrated than in traditional LEDs.

Future work – Year 2 (remaining 3 months)

One aspect that needs further investigation is the interaction between junction temperature and the amount of short wavelength radiation on the degradation of white LED. This subject is currently being investigated and the results will be reported at a later time.

Tasks of interest for the development of RCLEDs include the study of interactions between junction temperature and distance from the phosphor layer to the semiconductor die. Since RCLEDs are still under development at UCSB, we plan to use a commercial blue laser diode for the study. Initially, feedback into the laser diode will be monitored as a function of intensity and the relative geometry with the phosphor layer. This task would include software modeling to characterize these effects in configurations that may be difficult to build.

R.7 RCLED Packaging Issues – *Source Modeling*

Prior to modeling the RCLED device a literature survey was conducted to understand what others have done in the are of light extraction to improve efficiency.

Background: An improvement in the overall efficacy of an RCLED can by achieved by increasing its light extraction efficiency—the ratio of total light generated in the device to the amount of light that escapes from the device. A planar LED device releases only a fraction of the total generated light; the remainder is trapped within the device and absorbed due to total internal reflection (TIR) occurring at device-air interface and Fresnel reflection at the same interfaces. Light rays hitting an interface at an angle larger than the critical angle will undergo TIR. The critical angle (θc) is given by:

$$\theta c = \arcsin (n_1/n_2)$$

where n_1 is the refraction index of the outer material (typically $n_1 = 1$ for air, and greater than 1 for epoxy), and n_2 is the refraction index of the semiconductor material. The critical angle forms an escape cone through which light is extracted. Light extraction efficiency of planar LED devices can be improved by altering the geometric shape of the LED device. Six light extraction scenarios are described next.

Transparent epoxy dome

An increase in the critical angle, and thus the amount of light extracted, can be achieved by using a transparent epoxy dome with a high refractive index (normally 1.4 to 1.5) over the die (Fig. 40). Epoxy domes are typically employed in indicator type LEDs to increase their efficiency.

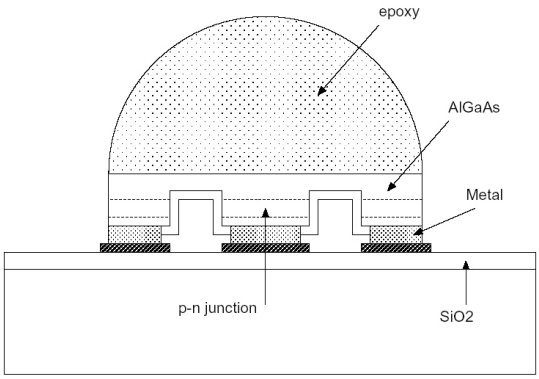

Fig. 40. A commercially available, high-efficiency LED with an epoxy dome.[21]

Extraction through multiple planes

Extracting light through more than one surface can improve the extraction efficiency of the light source (Fig. 41). For example, a cubic LED emitting light through all six planes potentially will have extraction efficiency six times greater than an LED using only a single plane for light extraction. Light inside the LED can be redirected and further extracted by altering certain structural components. For a planar LED, adopting a rear mirror between the active layer and the light absorbing substrate can double the extraction efficiency.

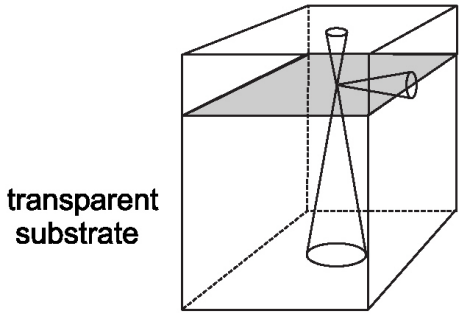

Fig. 41. A cubic LED can extract light from six surfaces.[22]

Truncated Inverted Pyramid (TIP) LED

The TIP LED technique breaks the cubic chip's symmetry in such a way that allows the rays to be reflected internally two, three or even more times after leaving the semiconductor, altering the direction of the rays until they reach the escape cone. By using this technique, the light is given different propagation angles after bouncing off of a skew interface, as shown in Fig. 42 (right). Efficiencies of approximately 50% have been reported for AlGaInP LEDs using this technique.[23]

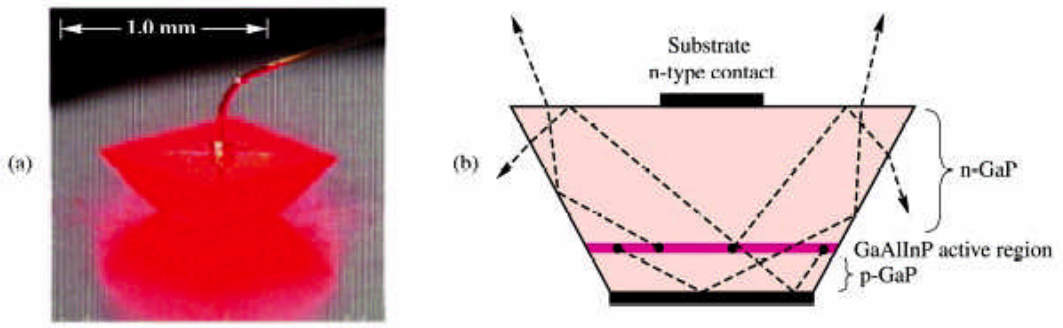

Fig. 42. Truncated inverted pyramid (TIP) LED structure by Lumileds.[24]

Tapered LED

In an alternative concept, a tapered LED (Fig. 43), light extraction occurs at the bottom. The truncated cone cylindrical surface is covered with a gold (Au) mirror. Light that is not extracted from the bottom out-coupling surface is reflected again at the metal mirror on the taper. Each time the light hits the taper, its angle of incidence is reduced by the taper angle. Finally, when the incidence angle is smaller than the critical angle, the light is extracted. At first sight, this tapered LED looks very similar to the inverted pyramid LED of the previous section. However, this device is planar and extraction is single-sided. Absorption is expected to have a strong influence since the intensity decrease obeys an exponential law in distance. A maximum extraction efficiency of 35% has been reported for an absorption coefficient of $100cm^{-1}$ at an angle of 22°.[25]

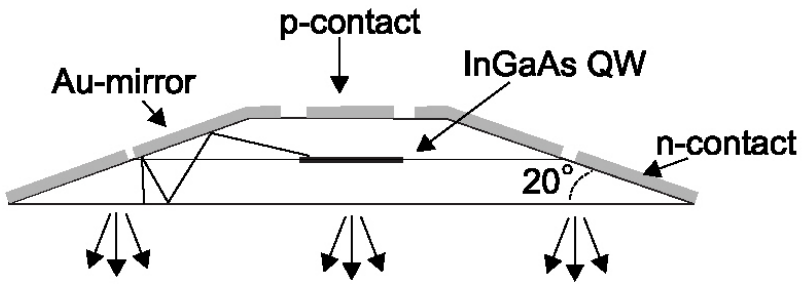

Fig. 43. Tapered LED structure.[22,26]

Surface-roughened LED

Another way to increase the extraction efficiency of planar LED devices is to roughen one or more surfaces of the chip and place a high reflectivity mirror on the bottom side. When the light is scattered at the roughened top surface, its path is altered in a random way. Light that is not extracted through the top surface is reflected back and forth between the back mirror and the roughened surface and gets another chance to be extracted. If the dimensions of the LED are small, absorption can be minimized and the randomly scattered light has a statistically larger probability of escaping the LED (Fig. 44). Maximum overall efficiencies of 41% have been reported by roughening alone and of 55% when the LED is surrounded by an epoxy dome.[22]

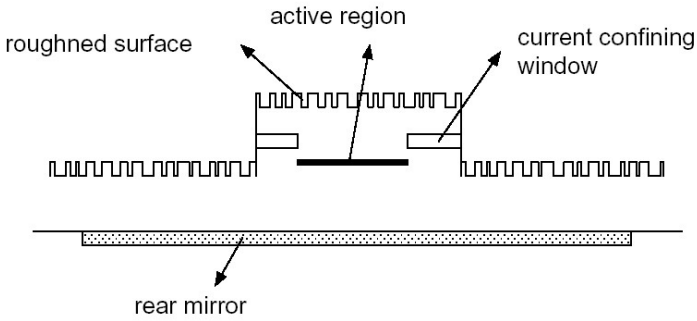

Fig. 44. Surface-textured LED structure.[21,27]

Resonant-cavity LED

Resonant-cavity LEDs handle the problem of light extraction with a completely different approach compared with the former devices. Figure 45 shows a simplified structure of an RCLED. Normally, the back mirror has a reflectance greater than 90% while the outer mirror's reflectance is approximately 30% to 50%. In an RCLED, a resonator is used to form the angular power distribution inside the device in such a way that more of the active layers' emissions are launched into the escape cone. The resonant-cavity effect modifies the preferential propagation direction of the photons spontaneously emitted. While the radiant energy of an RCLED is lower than that of a laser for a given power, it is easily orders of magnitude larger than the conventional LEDs. The RCLED is the only commercialized high-efficiency LED so far, but it is in the red to near-infrared region. Other devices under study use a combination of the resonant-cavity effect and a controlled distribution of light using a grating (grating-assisted RCLEDs) or they use a resonant-cavity reflector (RC LEDs).[22]

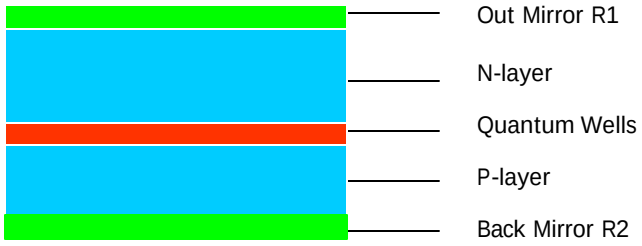

Fig. 45. RCLED basic structure.

Device Modeling: Figure 46 illustrates the UCSB RCLED structure upon which we based our modeling. The RCLED consists of a flip-chipped GaN with the sapphire removed and the cavity thinned to deposit a distributed bragged reflector (DBR) as the outer mirror. The reflectance of the three pairs of DBR is approximately 50%. The back mirror is a silver mirror with a reflectance of 95%. The device's emitting aperture varies from 6 μm to 350 μm. The n-contact layer has an inner diameter of 10 μm, larger than the aperture, and its outer diameter is another 30 μm larger than the aperture. The size of the current blocking layer aperture determines the size of the emission; hence, the light is not emitted directly beneath the n-contact layer. This minimizes the light loss due to the n-contact layer. Figure 47 is a photograph of the forward-biased RCLED with an 'interfacial' top-side mirror. In Fig. 47, the mesa shape, the n-contact layer, and the emitting aperture are clearly illustrated. Figure 48 illustrates an example of the RCLED far-field emission pattern. In Fig. 48, the device's internal emission maximum is at 13.3°, corresponding to an external emission maximum at 35°. The dominant emission wavelength is 412 nm.

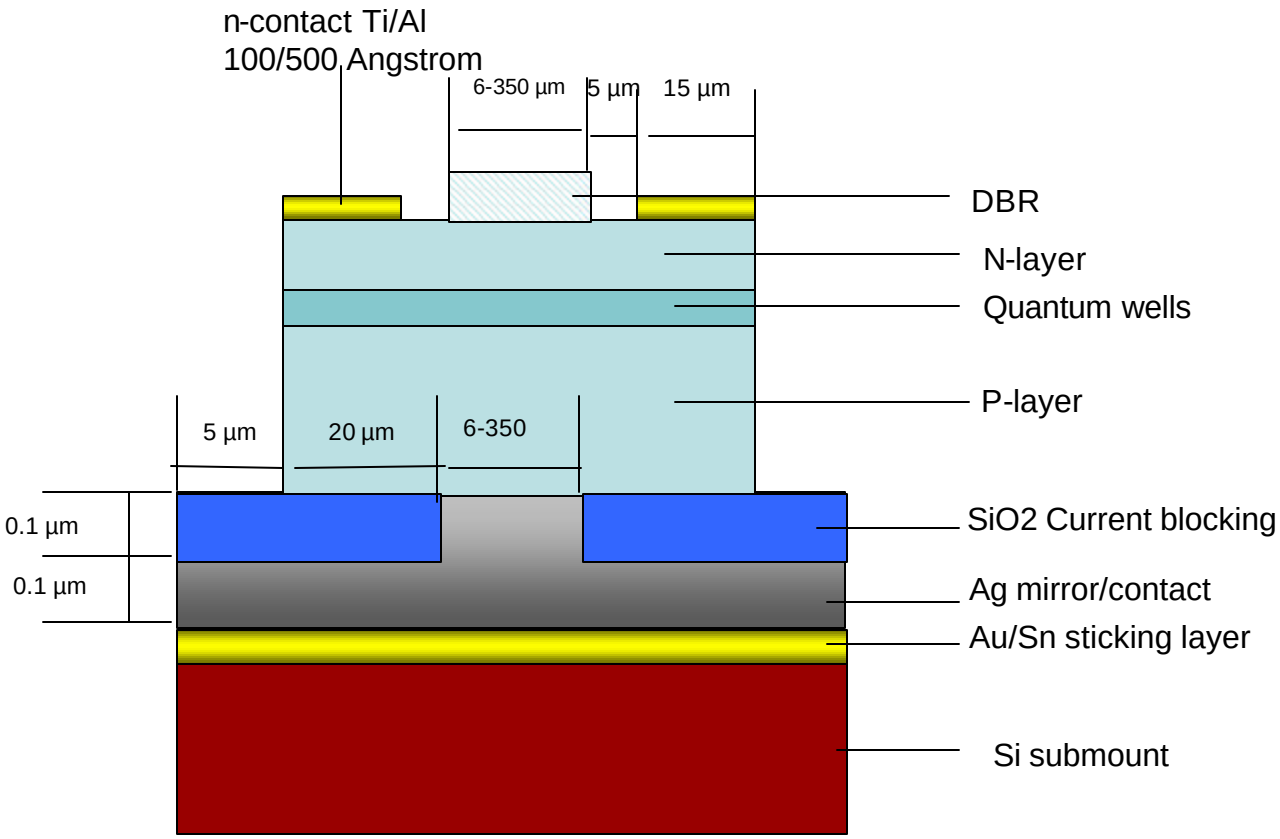

Fig. 46. UCSB RCLED structure [UCSB].

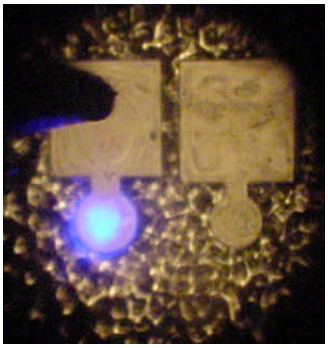

Fig. 47. Photograph of the forward-biased RCLED with 'interfacial' top-side mirror [UCSB].

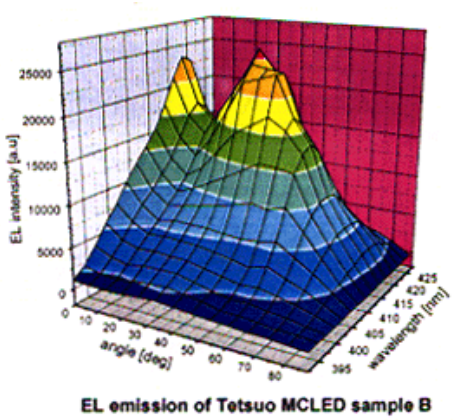

Fig. 48. An example of the RCLED far-field emission pattern [UCSB].

Prior to starting the modeling effort for the UCSB RCLED device, a short pilot study was conducted where a traditional LED and TIP LED devices were modeled to see how well results can be derived by using a commercial ray tracing software package LightTools™.

Modeling TIP LEDs in LightTools™

Table 3 summarizes the modeled TIP LED chip parameters.[28] The sapphire inclination angle was systematically changed from 0° to 75°, and the light extraction efficiency for each condition was calculated in the software. For each condition, 50,000 rays were traced. Figure 49 shows the modeled LED die shape at the different sapphire inclination angles. Figure 50 is the literature review findings on TIP LED light extraction efficiency [Eisert *et al.*, Simulation in the Development Process of GaN-based LEDs and Laser Diodes, Osram Opto Semiconductors GmbH, Regensburg, Germany, 2003].

Figure 51 illustrates our modeling result for the light extraction efficiency at different sapphire inclination angles. The results conform to those in Fig. 50. This consistency makes us believe that it is feasible to use LightTools to model LED chips.

Table 3. TIP LED source modeling parameters [Stefanov *et al.*, Proc. SPIE 4776 (2002) 223].

Layers	Thickness (μm)	Refractive index	Absorption (1/μm or %)
p-pad	0.24	-	14%
Transparent contact	-	-	15%
p_GaN	0.300	2.42	0.017
AlGaN	0.150	2.33	0
InGaN	0.110	2.54	1.25
N-GaN	3.000	2.42	0.017
Sapphire	75.000	1.78	0

*** Note, parameters are derived at wavelength 420nm**
**** The die dimensions are 350μm X 350μm**

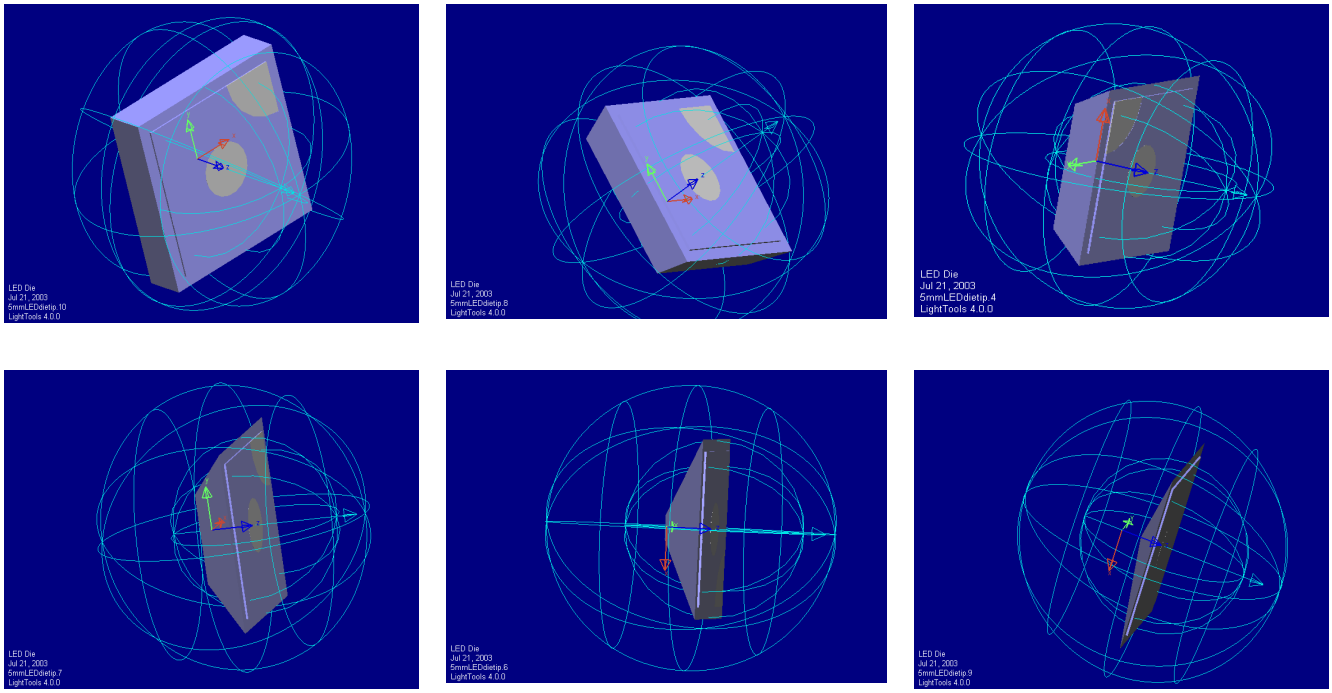

Fig. 49. TIP LED Chip Model at different sapphire inclination angles.

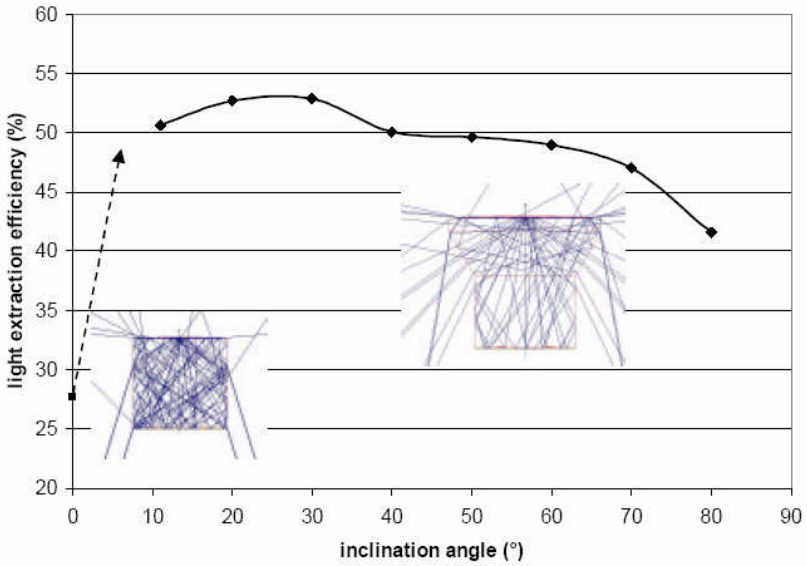

Fig. 50. TIP LED extraction efficiency at different sapphire inclination angles [Eisert *et al.*, Simulation in the Development Process of GaN-based LEDs and Laser Diodes, Osram Opto Semiconductors GmbH, Regensburg, Germany, 2003].

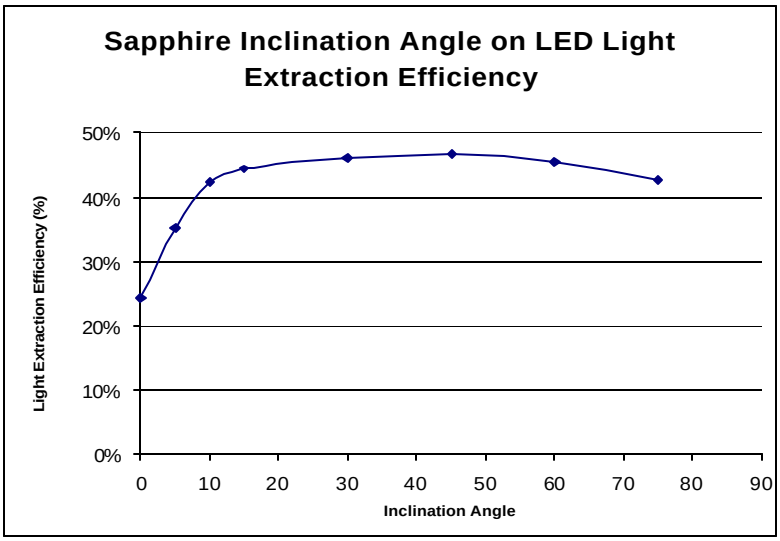

Fig. 51. Modeled TIP LED light extraction efficiency at different sapphire inclination angles.

Modeling UCSB RCLED in Light Tools

The next step was to model an RCLED. Table 4 summarizes the modeled UCSB RCLED parameters, including the thickness, refraction index, absorption, and reflectance of different layers.

Impact of Device Size and Internal Emission Pattern on Light Extraction

Since LightTools has limited capabilities in modeling physical optics such as the RCLED resonant-cavity effect, and because the UCSB RCLED internal angular emission distribution pattern is not available yet, three internal angular emission distribution patterns were selected to simulate the RCLED resonant-cavity effect. The first is the InGaAs RCLED internal angular emission distribution pattern, as shown in Fig. 52;[29] the second one is a shifted InGaAs RCLED internal emission pattern, which shifts the first emission about 5° to mimic the UCSB RCLED maximum internal emission at 14°; the third is the conventional Lambertian emission pattern. Figure 53 illustrates the three normalized internal angular emission distribution patterns. Note in Fig. 52 that the y-axis is in log scale; in Fig. 53, the same InGaAs emission pattern is plotted in linear scale.

Table 4. RCLED source modeling parameters.

Resonant Cavity LED Source Modeling Parameters

	Layers	Thickness (μm)	Refractive index	Absorption (1/μm or %)	Reflectance
Top reflector	p-contact and metal reflector	-	-	5%	95%
P-layer	p-GaN, GaN:Mg	0.082	2.51	0.017	0
	$Al_{0.18}GaN$:Mg	0.020	2.401	0	0
1-3 layer Quantum Wells	$In_{0.10}GaN$	0.004	2.661	1.25	0
	$In_{0.035}GaN$:Si barriers	0.008	2.545	1.25	0
N-layer	LT GaN:Si	0.008	2.51	0.017	0
	GaN:Si	1.000	2.51	0.017	0
3 pairs of DBR reflector	Ta_2O_5	0.048	2.16	0.017	45%~56%
	SiO_2	0.066	1.56	0	

*** Note, parameters are derived at wavelength 412nm**

16.13%

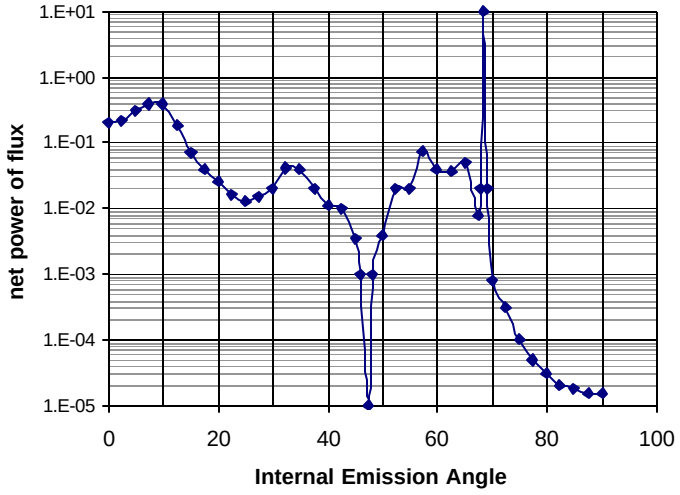

Fig. 52. Internal angular emission distribution pattern of InGaAs RCLED devices.

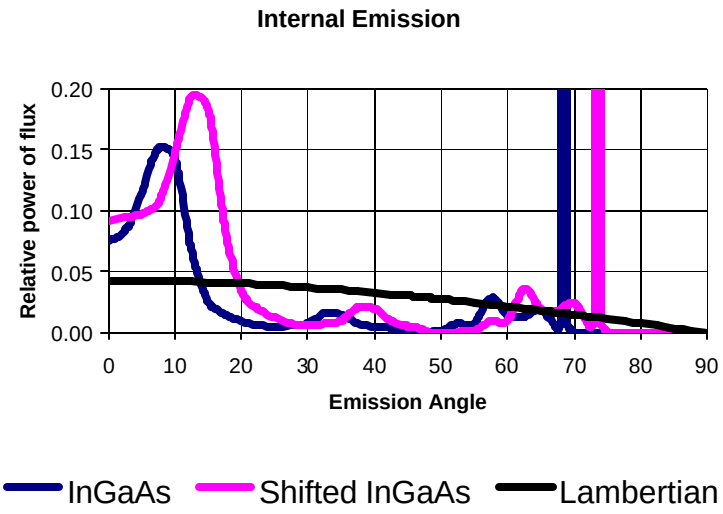

Fig. 53. Three internal emission distribution patterns used for the modeling.

Presently UCSB researchers are fabricating devices with different aperture sizes to analyze their performance. Therefore, six different RCLED devices with different aperture sizes, similar to the ones prepared by UCSB, were modeled: 6 µm, 20 µm, 30 µm, 50 µm, 100 µm, and 350 µm. Figure 54 illustrates two examples of the devices modeled in LightTools. The left one has an aperture size of 6 µm; the right one is 350 µm. Figure 55 shows the impact of device size and internal emission pattern on RCLED light extraction efficiency. It is not surprising that the internal angular emission patterns significantly impact the RCLED light extraction efficiency. For a 350 µm devices with a Lambertian emission pattern, the light extraction efficiency is 16.7%. Using the InGaAs RCLED emission pattern, the efficiency improved to 42.1%; with the shifted InGaAs RCLED emission pattern, it became 50%. Device aperture size also has some impact on light extraction. With an aperture size increase from 6 µm to 350 µm, the light extraction efficiency decreases approximately 6% for the InGaAs emission pattern and 7.6% for the shifted InGaAs emission pattern. Figure 56 illustrates the RCLED bare device's far-field intensity distribution. With the shifted InGaAs emission pattern (maximum internal emission at 14°), the model gives the maximum far-field intensity at about 35°. This conforms to the calculations done at UCSB that state the 13.3° maximum internal emission results in a maximum far-field intensity at 35°. It also worth noting that the device aperture size has little impact on the far-field intensity distribution pattern.

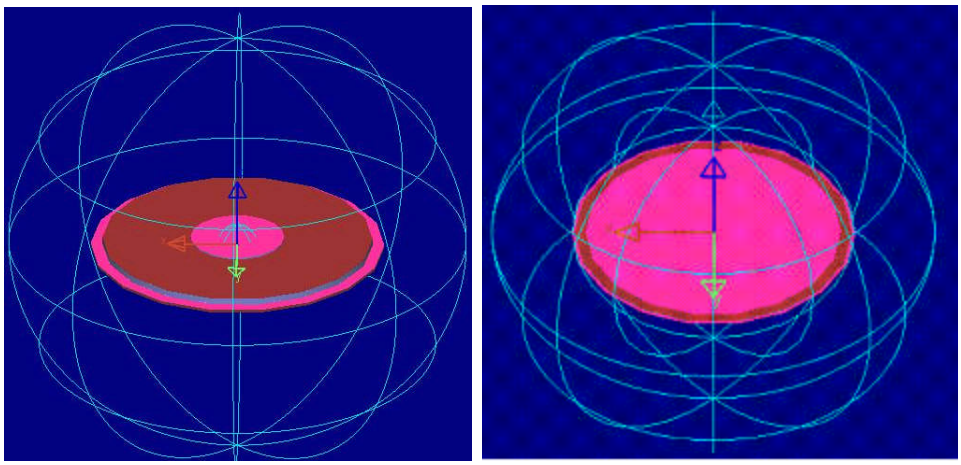

Fig. 54. Example of software-modeled devices (left: 6 µm aperture; right: 350 µm).

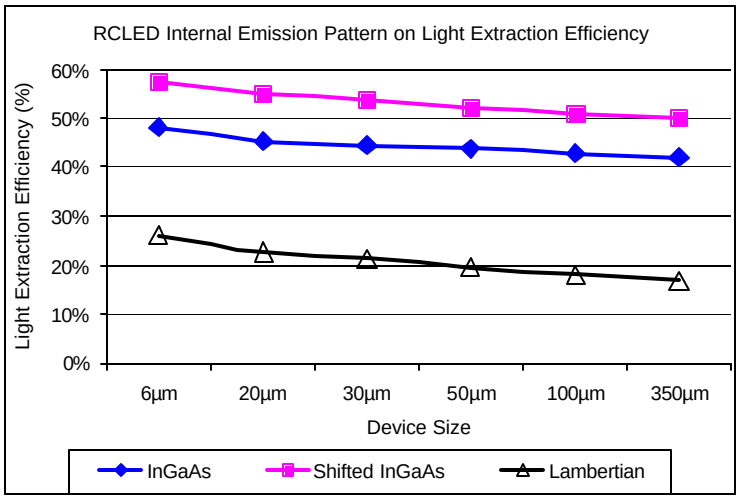

Fig. 55. Impact of device size and internal emission pattern on RCLED light extraction.

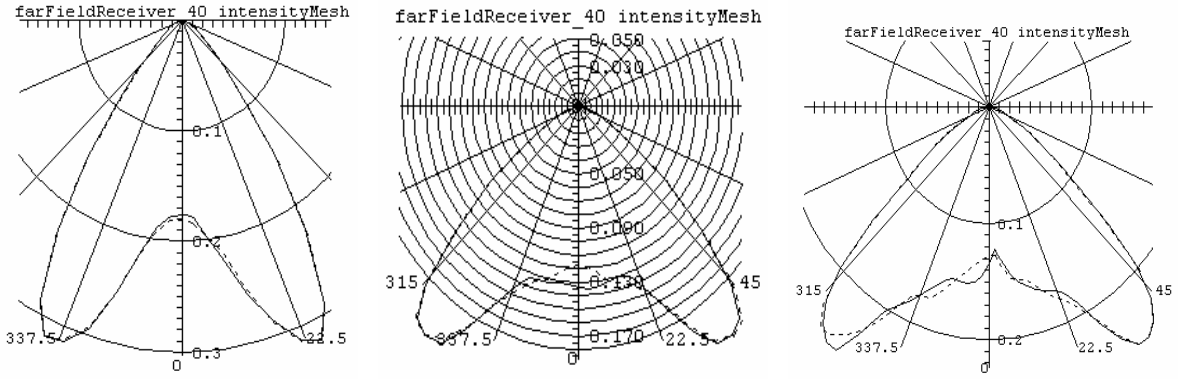

Fig. 56. RCLED far-field intensity distribution (left: 350 µm, InGaAs; center: 350 µm, shifted InGaAs; right: 6 µm, shifted InGaAs).

Impact of the Epoxy Dome on RCLED Light Extraction

A 5 mm diameter epoxy dome was attached to the RCLED. The refraction index of the epoxy dome is 1.5. Figure 57 illustrates the model of the epoxy dome and its enhancement on RCLED light extraction efficiency. It can be seen that the epoxy dome can dramatically enhance the light extraction efficiency for devices with a lambertian emission pattern, like the traditional LEDs (12% to 16% increase), but for RCLEDs with a more directional emission pattern such as the InGaAs or shifted InGaAs emission pattern, the enhancement is much smaller, a 6% to 9% increase. Figure 58 illustrates the far-field intensity distribution of the RCLED with the epoxy dome. Compared with Figure 56, it can be seen that the epoxy dome actually makes the intensity distribution more directional (decreases the beam angle).

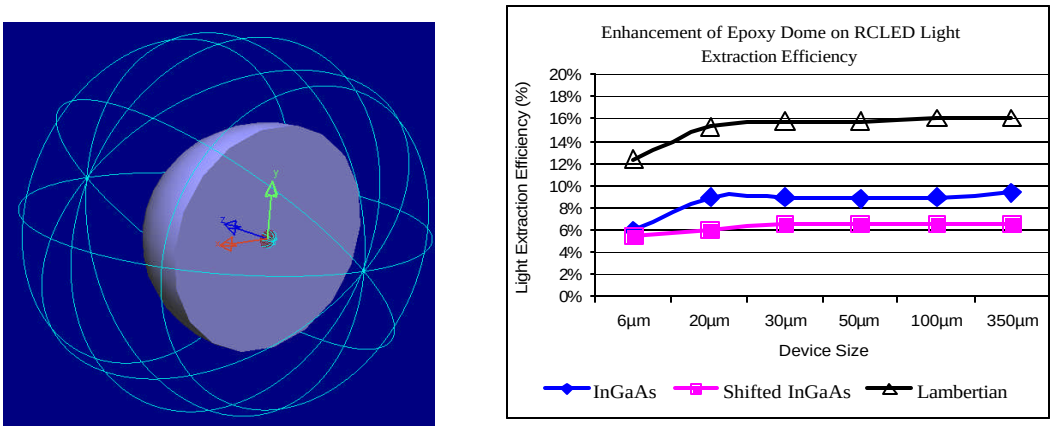

Fig. 57. The epoxy dome model and its enhancement on RCLED light extraction efficiency.

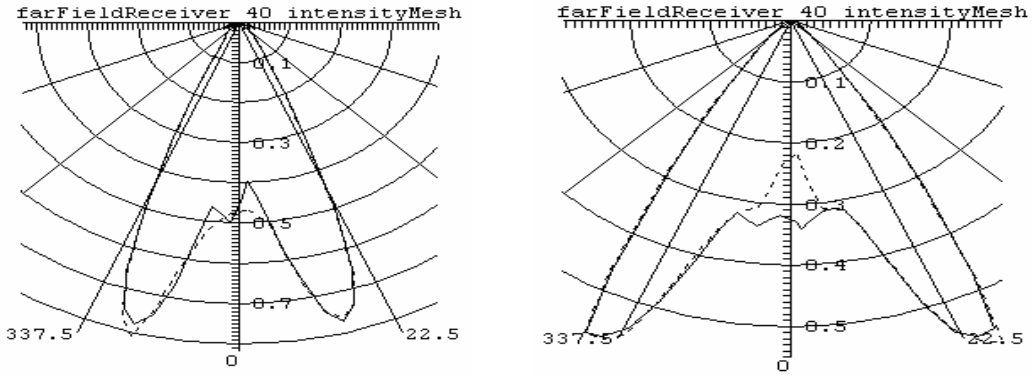

Fig. 58. Far-field intensity distribution of RCLED with epoxy dome (left: 350µm, InGaAs; right: 350 µm, shifted InGaAs).

Impact of Epoxy Cone on RCLED Light Distribution

It is always useful to have a method to change the beam distribution without impacting the extraction efficiency. The shape of the epoxy encapsulant was changed in this analysis. A truncated epoxy cone was attached to the RCLED. The refraction index of the epoxy cone is 1.5. The cylindrical surface of the epoxy cone is modeled as a reflecting cup (reflectance 95%). Figure 59 illustrates the epoxy cone model and the impact of cone taper angle on RCLED light extraction efficiency. It can be seen that at an epoxy cone taper angle between 20° and 75°, light extraction efficiency is almost constant; however, the taper angle changed the far-field intensity distribution pattern (Figure 31). Figure 60 shows the enhancement of a 60° tapered epoxy cone on RCLED light extraction efficiency. It can be seen that the epoxy cone can dramatically enhance the light extraction efficiency for devices with a Lambertian emission pattern (12% to 17% increase). However, for the RCLED with a more directional emission such as the InGaAs or shifted InGaAs emission pattern, the enhancement is much smaller, about 6% to 10%. Figure 61 illustrates the far-field intensity distribution of the RCLED with a 60° tapered epoxy cone. Compared with Fig. 56 and Fig. 58, it can be seen that the 60° tapered epoxy cone actually collected more light to the nadir.

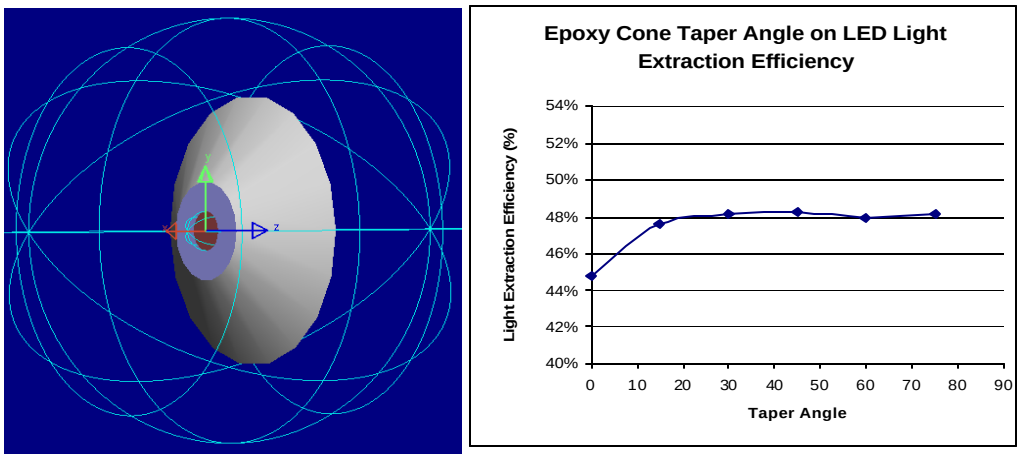

Fig. 59. The epoxy cone model and the impact of cone taper angle on light extraction.

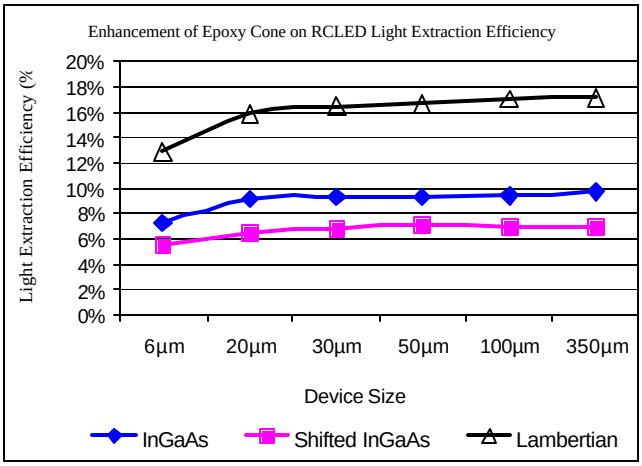

Fig. 60. The enhancement of a 60° tapered epoxy cone on RCLED light extraction efficiency.

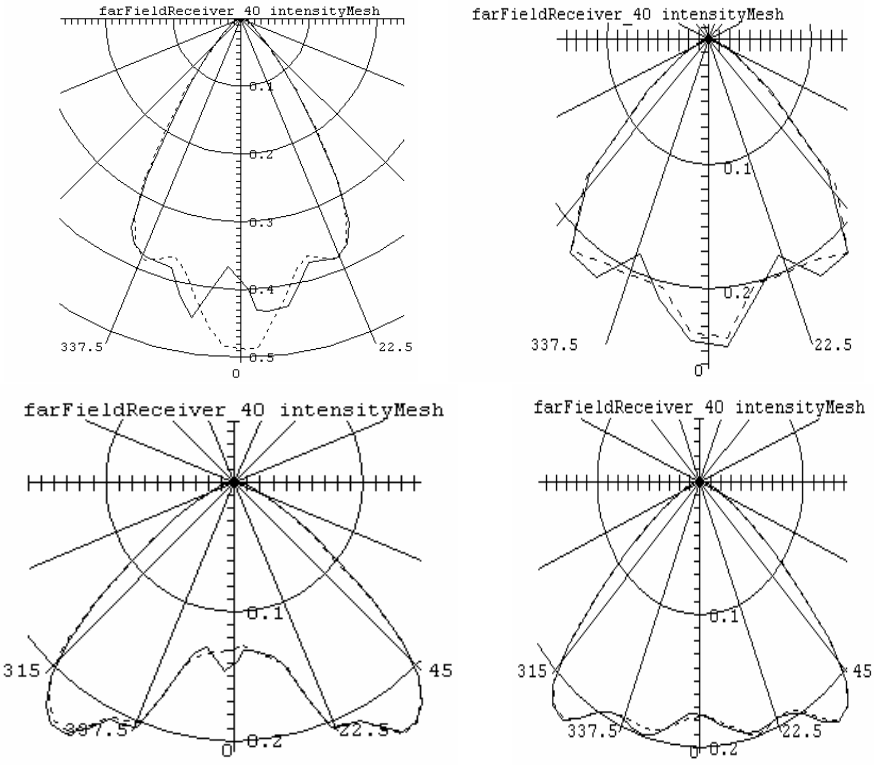

Fig. 61. Far-field intensity distribution of the RCLED with a tapered epoxy cone (top left: 350 µm, InGaAs, 60° taper; top right: 350 µm, shifted InGaAs, 60° taper; bottom left: 350µm, Shifted InGaAs, 75° taper; bottom right:350µm, shifted InGaAs, 30° taper).

Conclusions

- RCLED internal emission pattern has a major impact on light extraction efficiency. Devices with the InGaAs RCLED emission pattern double or triple extraction efficiency compared with those with a lambertian pattern such as in traditional LEDs.
- Device aperture size has some impact on RCLED light extraction efficiency. A device with a smaller aperture has larger light extraction efficiency; for example, a 6 µm aperture device has 6% more extraction efficiency than a device with a 350 µm aperture size. However, device aperture size seems to have little impact on the far-field intensity distribution.
- Epoxy shape also impacts RCLED light extraction efficiency. For devices with the InGaAs or shifted InGaAs RCLED emission pattern, a 6% to 9% extraction efficiency gain can be achieved with a 5 mm diameter epoxy dome or a 1 mm diameter truncated epoxy cone (taper angle 60°). The epoxy dome will narrow the beam angle and make the far-field intensity distribution more directional. The truncated epoxy cone with a 60° taper angle tends to project more light to the nadir direction. One of the advantages of using the truncated epoxy cone is that by changing the taper angle, we may obtain the desired far-field intensity distribution pattern without sacrificing light extraction efficiency.

Future work – Year 2 (remaining 3 months)

The future steps for this task include measuring the far-field intensity distribution of the RCLED prototype as soon as it is available from UCSB. This will allow us to verify the modeled results and refine the input parameters for future modeling tasks. Crosschecking the prototype against the computer

model will help to refine the simulating process. Once this is achieved, the role of each element in the RCLED structure can be studied systematically to understand its impact on the RCLED optimization.

R.8 RCLED Packaging Issues –*White Light Source Modeling and Prototyping*

White light source modeling

Since the ultimate goal is to create an efficient white light solid state light source, the goal of this task was to use the RCLED and create a 200 lm/W white light source. It was shown earlier that placing the phosphor layer further away from the LED device could improve performance significantly. This section describes the approach taken to address this issue. As mentioned earlier the performance target for the redistributing optical element is to achieve efficiency greater than 94% and uniformity of light along the length of the tube to be less than 10% (less than 10% variation for max/avg ratio).

Because the RCLEDs are still being developed, a traditional blue LED array was used to develop the white light source package. The LED source chosen for this investigation was a high-flux blue (470 nm) illuminator LED (Shark series) by Opto Technology Inc. Table 5 shows the electro-optical characteristics of the Shark blue LED. To verify the software modeling procedure, the Shark LED was modeled in LightTools software. The distribution matched with the distribution specification from the manufacturer (Fig. 62).

Table 5. Initial electro-optical characteristics of the Shark LED at TJ = 25°C, = 200 mA.

TYPE	Typical LUMINOUS FLUX (lm)	RADIANT FLUX (Calculated)	FORWARD VOLTAGE (V)	DOMINANT WAVELENGTH [PEAK] WAVELENGTH (nm, CIE x,y)		
				MIN	TYP	MAX
BLUE	7.0	51.5 lm/W @ 465 nm	16.06	465	470 x = 0.13 y = 0.07	475

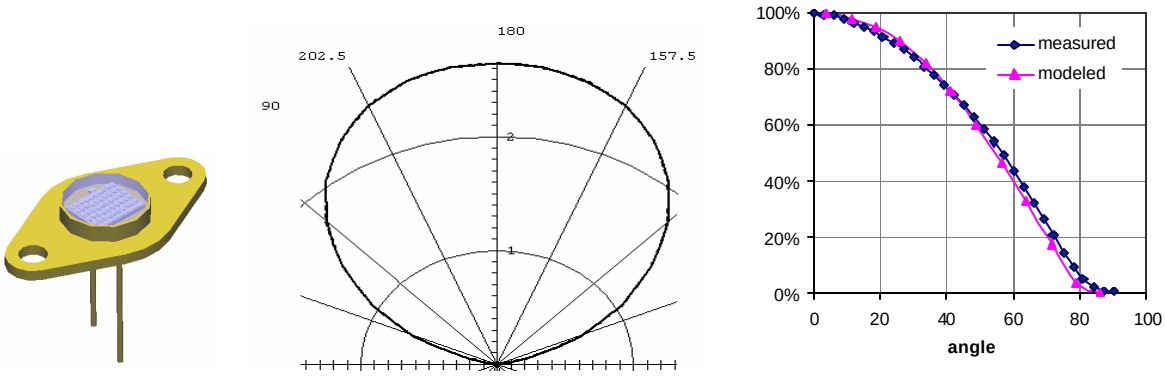

Fig. 62. Shark LED model and its distribution.

Optical modeling setup

Figure 63 shows the setup of the optical model, which consisted of the LED light source, the distributing optic, and a receiving plane next to the optical element at a distance where a hollow cylinder coated with the phosphor would be placed. The optical model was run to trace one million rays, which had a precision of approximately 5%. Calculations on the receiving plane gave a measure of the illuminance uniformity.

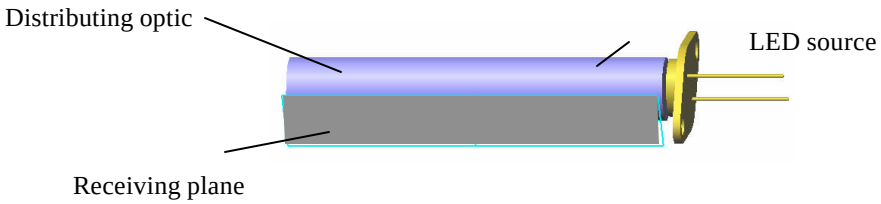

Fig. 63. Optical model setup.

Optical design approaches

There were two distinct approaches to the design of the distributing optics. One was similar to a linear fluorescent lamp where the light is uniform along the surface of the cylinder and is diffused (Fig. 64). The other approach was to make the beam more directional similar to a fluorescent lamp with a reflector (Fig. 65). Both were identified as having their own advantages depending on the application.

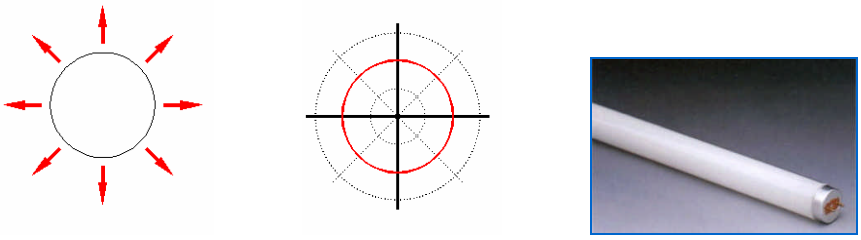

Fig. 64. Approach 1: Uniformly diffuse distribution.

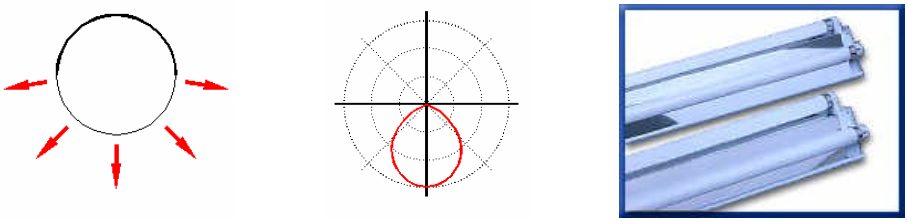

Fig. 65. Approach 2: Directional distribution.

Optical design approach 1: Uniform, diffuse distribution

Creating an uniform light output all around and along the length of the optical element required a waveguide optic with a diffuse, circularly symmetric (conical) reflector on the inside. The waveguide helped carry the light further along the length of the tube, as shown in Fig. 66, thereby creating more uniformity along the length. The conical reflector made the distribution uniform around the optic.

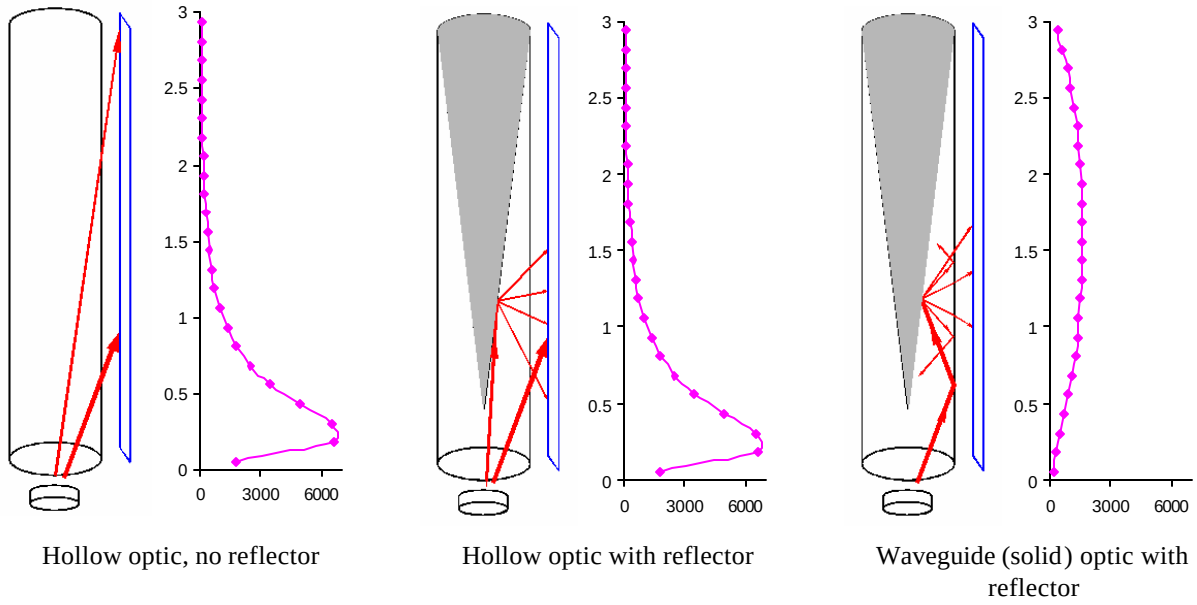

Fig. 66. Different optics with their illuminance distribution profiles along the length.

The illuminance uniformity increases with increases in the length of the cone reflector (Fig. 67). However, small changes in the reflector's conical profile were required to improve the uniformity at the top and the bottom end of the reflector (Fig. 68).

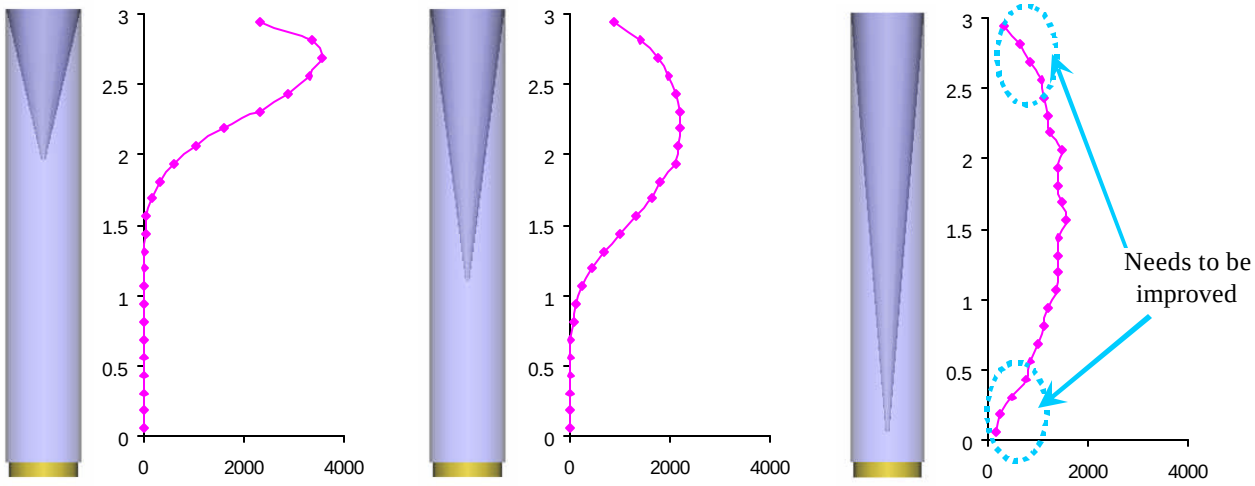

Fig. 67. Illuminance distribution as a function of the length of the reflector.

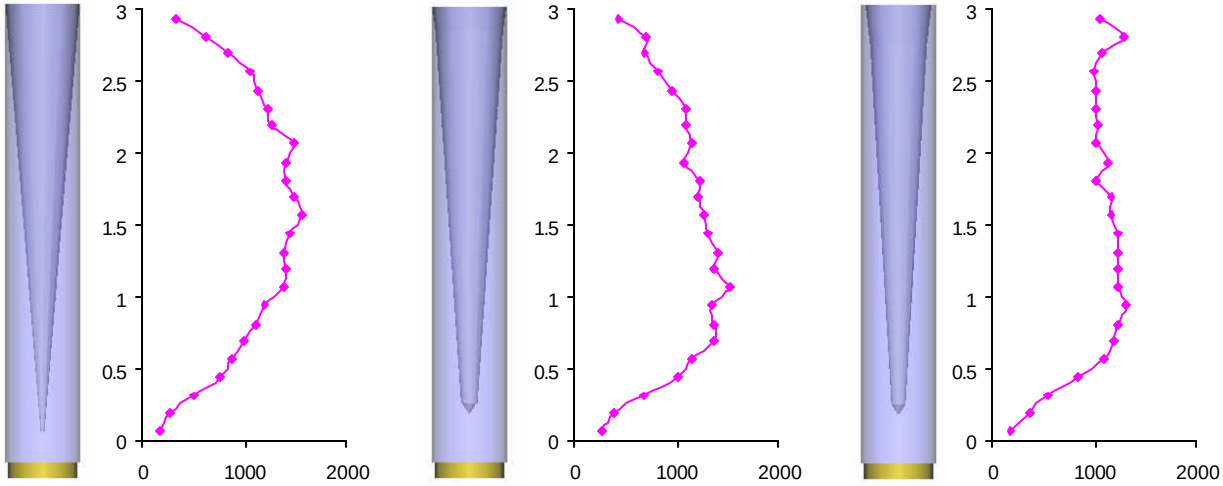

Fig. 68. Illuminance distribution as a function of the reflector profile.

Further analysis also showed that the optimum uniformity and efficiency were achieved when the length of the optic was 2 inches for the LED selected in this study (Fig. 69).

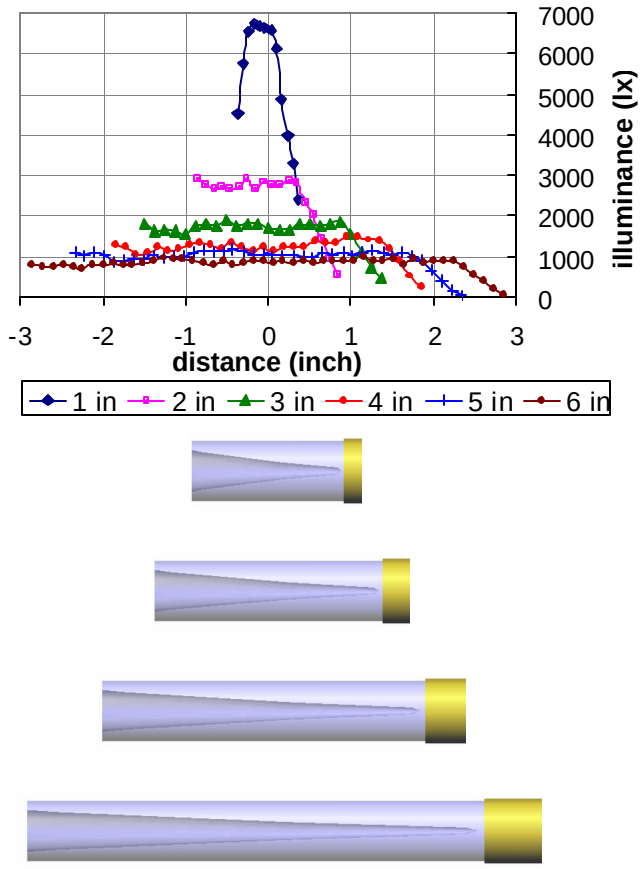

Fig. 69. Illuminance distribution as a function of the length of the optic.

Efficiency of the distributing optical element

The overall efficiency of the distributing optical element using Approach 1 was found to be approximately 73%. This is far below what we needed, 94%. Analysis showed the following losses:

- 14% absorbed by the reflector paint (90% reflectance)
- 7% light reflected back to LED
- 4% Fresnel loss
- 2% irrecoverable due to mounting hardware

Approximately half of the losses can be attributed to the reflectance of the paint (90%). This can be improved by using paint with a higher reflectance. Further, losses can be recovered by using a better coupling mechanism and an anti-reflective coating to prevent Fresnel losses. These values can be improved to 91% by recovering some of the losses. Steps to recover losses include increasing the reflectance of the reflector to 95%, using epoxy to fill the air gaps between the LED source and the optic, and adding a reflective filter in front of the LED source to prevent light from being reflected back to the LED.

Optical design approach 2: Directional distribution

One way to create a directional distribution is to have a reflector within a waveguide, forcing the distribution in a specific direction. With a circular waveguide, a directional distribution can be created using a circular reflector or a flat reflector (Fig. 70). The pitch of the reflector and the length of the optic control the uniformity, the beam distribution, and the efficiency of the optic.

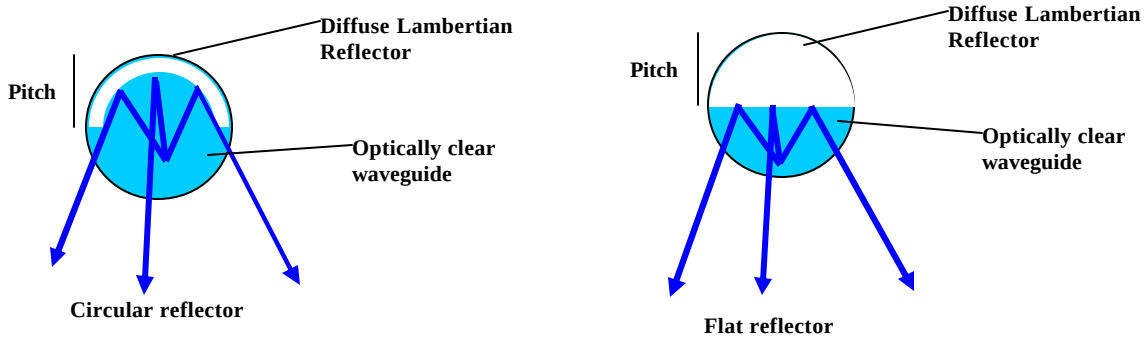

Fig. 70. Methods of creating directional distribution from a waveguide.

It was found that the uniformity did not vary much with the pitch, whereas the efficiency peaked at about 0.12 inches of the pitch for a 0.5 inch diameter waveguide (Figs. 71 and 72). It was also found that the circular reflector performed slightly better than the flat reflector for the same pitch.

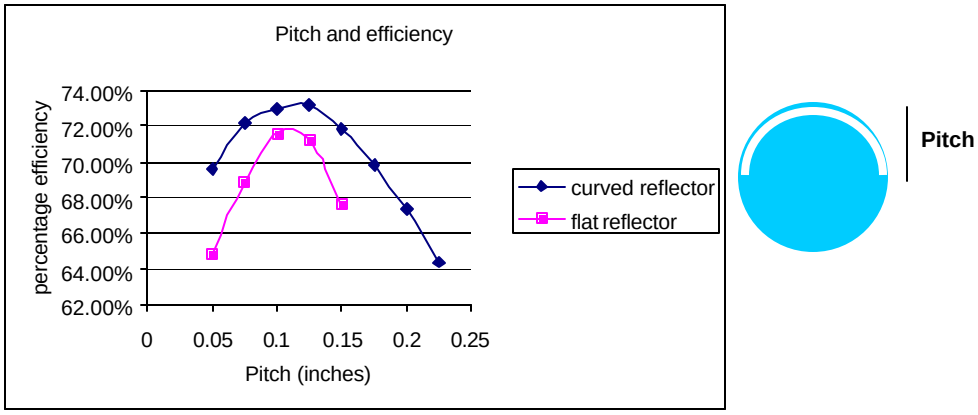

Fig. 71. Efficiency of the reflector as a function of its pitch.

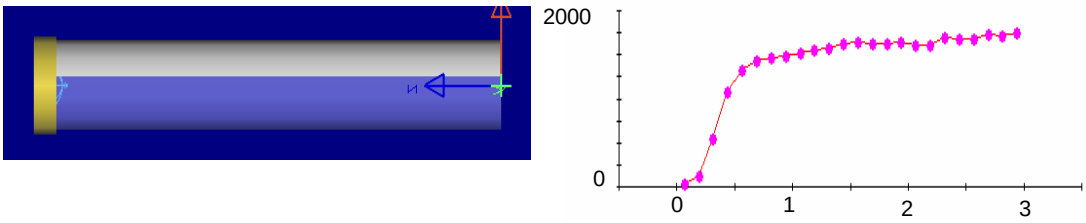

Fig. 72. Illuminance uniformity with a flat reflector.

The efficiency increases and the uniformity decreases with an increase in the length of the distributing optic. The highest efficiency value of 73% was achieved with a 3-inch length distributing optic with circular reflector and a pitch of 0.125 in. Analysis showed the following losses:

- 14% absorbed by the paint (@ 90% reflectance)
- 6% reflected back into the LED
- 4% Fresnel loss
- 3% irrecoverable due to mounting hardware

As in the previous case, the quality of the reflector plays a significant role in the efficiency of the distributing optic, so losses can be recovered by increasing its reflectance of the paint and reducing Fresnel loss. As before these values can be improved to 91% by recovering some of the losses. Steps to recover losses include increasing the reflectance of the reflector to 95%, using epoxy to fill the air gaps between the LED source and the optic, and adding a reflective filter in front of the LED source to prevent light from being reflected back to the LED.

Tolerance analysis

Before the prototype was built, a tolerance analysis was completed to understand the effects of minor changes in the position of the LED source or the optic. The analysis was completed for offsets in both the X and Z axis directions and also for rotation about the Y axis.

The analysis showed that there were significant changes when the offset was greater than 1/16 of an inch along the X axis, 1/32 of an inch along the Z axis, and 5° about the Y axis (Fig. 73).

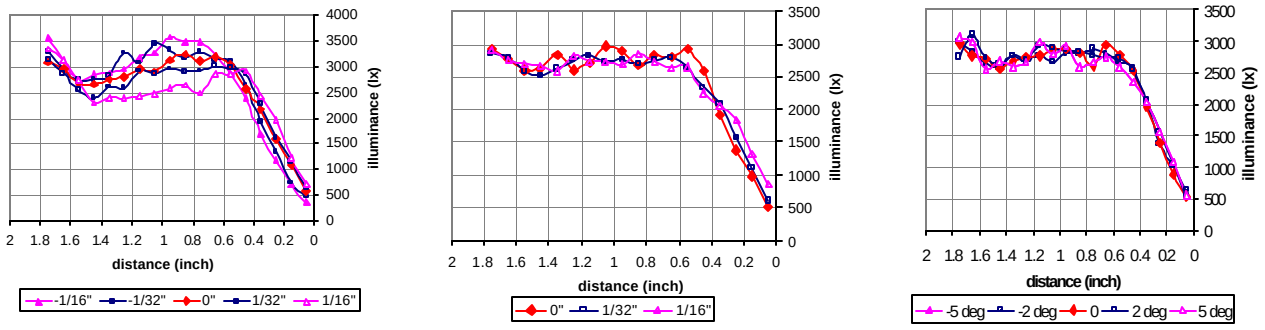

X axis offset Z axis offset Rotation about Y axis

Fig. 73. Tolerance analysis for changes in position of the LED source and optic.

Prototyping and testing

The first series of prototypes were built of clear acrylic rods within which the reflector shape was machined out. The reflector cone was painted with a 90% reflectance paint. This initial prototype did not conform to the original design because of the machining marks on the reflector surface. The final prototype was machined out of glass to specifications, which had a better match to the simulated optic.

The final prototype (Fig. 74) was then tested for illuminance uniformity using the image data captured from a CCD camera.

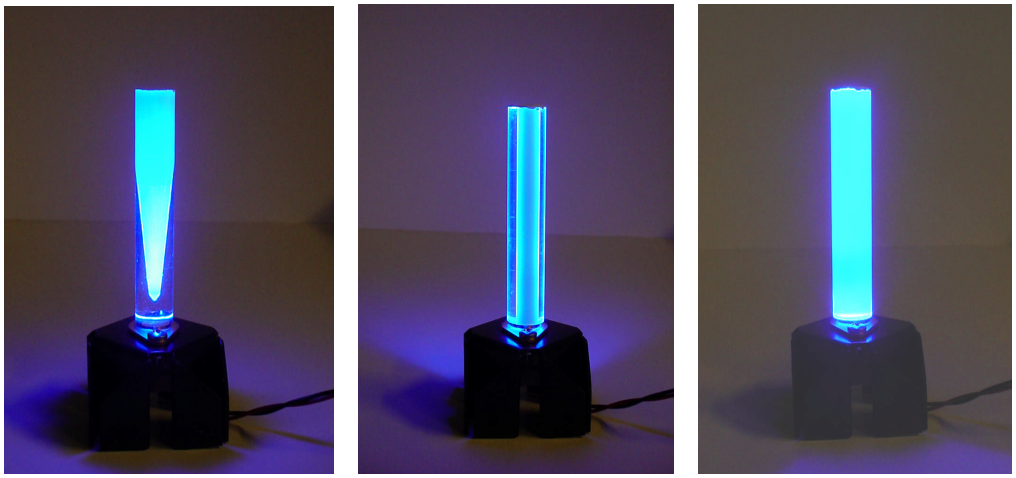

Fig. 74. Machined prototype of the simulated optic using blue LEDs showing the uniform diffuse distribution optic (left) and the rear and front views of the directional distribution optic (center and right, respectively).

Verification of simulation results

The simulated results were compared with the measured results from the prototype (Fig. 75). The simulated and the measured results matched closely for both approaches (Tables 6 and 7).

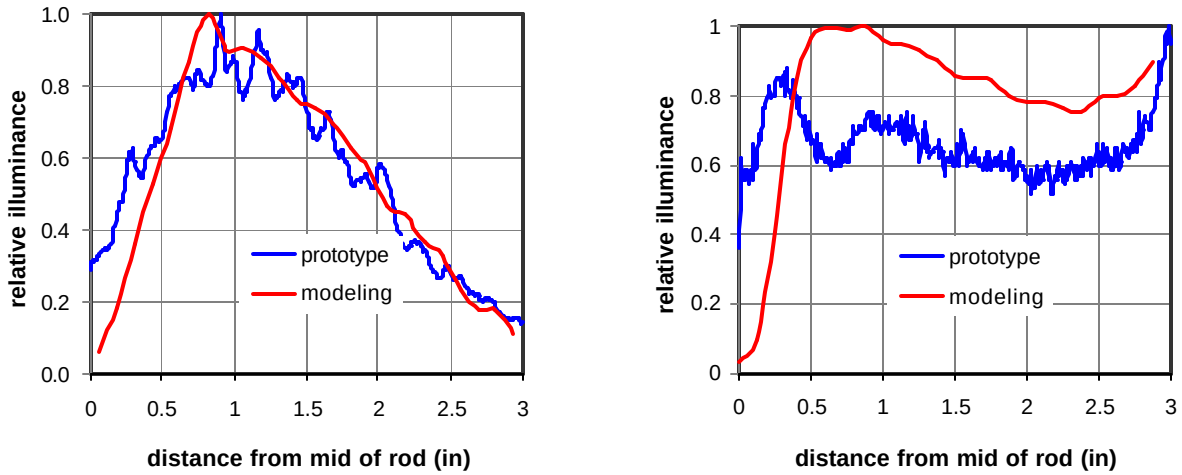

Fig. 75. Comparison of the simulated and prototyped results for the diffuse distribution optic (left) and the directional distribution optic (right).

Table 6. Comparison of results for Approach 1.

Uniformity ratio		Efficiency	
modeling	prototype	modeling	prototype
1.2	1.7	73%	72%

Table 7. Comparison of results for Approach 2.

Uniformity ratio		Efficiency	
modeling	prototype	modeling	prototype
1.3	1.5	65%	63%

Summary

Overall, the efficiency of the distributing optics for both approaches is lower than the target efficiency. These values can be improved to 91% by recovering some of the losses. Steps to recover losses include increasing the reflectance of the reflector to 95%, using epoxy to fill the air gaps between the LED source and the optic, and adding a reflective filter in front of the LED source to prevent light from being reflected back to the LED. Even though the uniformity ratios measured are satisfactory for phosphor excitation, a revised model shows that the uniformity can be further improved. The efficiency and uniformity measurements taken from the various prototypes closely matched the results from software modeling.

Future work – Year 2 (remaining 3 months)

As shown in Fig. 69, a 2-inch long distributing optic has the highest efficiency and uniformity. This 2-inch optic, prototyped in glass, will be available in the next several weeks. An outer tube with a uniform coating phosphor is also being made. This piece will be coupled with the distributing optic and assembled with a blue Shark LED. The complete assembly will then be tested for light output, efficacy, and uniformity.

R.9 Development of epoxy material

Three series of new oligomers were prepared. Curing and thermal stability properties of these oligomers were studied.

Oligomer Series 1

Oligomer Series 1 was synthesized by the following reaction:

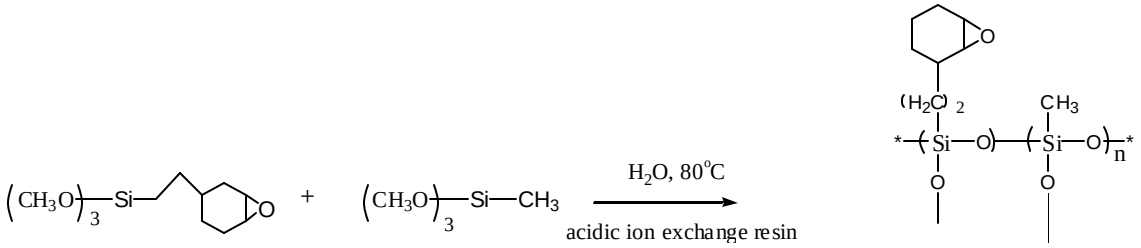

n = 3, 5, 8, 12

By varying the ratio of the two reactants from 1:3 to 1:12, the products with different structures were obtained. They are all colorless liquids which can be thermally and UV cured. The thermal stability tests we performed showed that all of the oligomers of Oligomer Series 1 turned yellow when kept in the oven at 140°C for one day. The cured polymers also turned yellow at 140°C.

Oligomer Series 2

Oligomer Series 2 was synthesized by the following reaction:

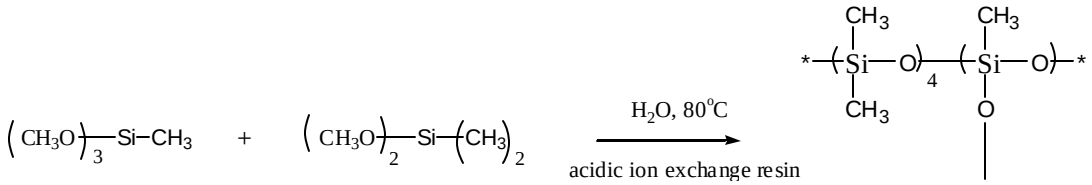

The resulting oligomer was a colorless liquid and formed a soft gel when cured in the oven at 140°C for a day. The resultant soft gel remained colorless at 140°C for 14 days. This result was very encouraging and led to the development of Oligomer Series 3.

Oligomer Series 3

Oligomer Series 3 was synthesized by the following reaction:

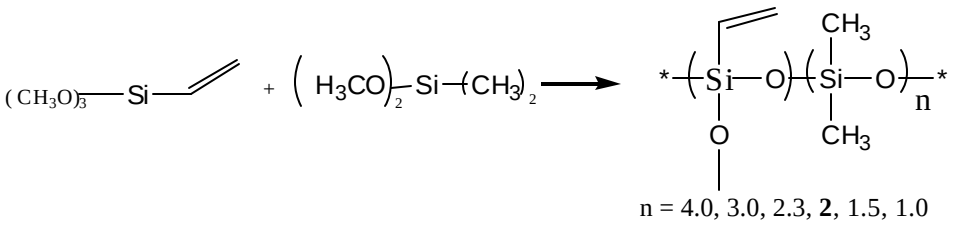

n = 4.0, 3.0, 2.3, **2**, 1.5, 1.0

By varying the ratio between the two reactants, vinyltrimethoxyl silane: dimethyl dimethoxyl silane = 1:1 to 1:4, a series of oligomers were obtained. The materials are all colorless liquids with low viscosities and can be cured to form colorless solids. All the solids remained colorless when heated to 140°C for 14 days. The results of the solids are listed in Table 8 below.

Table 8. Oligomer consistency vs. degree of oligomerization, **n**.

n=4	n=3	n=2.3	**n=2.0 (VPC 2000)**	n=1.5	n=1.0
soft	soft	soft	**hard**	hard with fractures	hard with fractures

We used the **n=2** oligomer (VPC 2000) for further thermal stability tests. The cured polymer remained colorless after three months at 140°C. Figure 76 shows a comparison of our material with conventional 5 mm LED epoxy. On the left are 5 mm LEDs without heat treatment, in the center are LEDs that were heated at 140 °C for 14 days, and on the right is our material that was heated at the 140°C for three months.

Fig. 76. Comparison of VPC 2000 with conventional 5 mm LED epoxy. Left: unheated conventional epoxy; center: conventional epoxy heated at 140°C for 14 days; right: VPC 2000 heated at 140°C for 3 months.

LED encapsulation with VPC 2000

Bare 50-LED arrays were purchased and encapsulated with VPC 2000. First, the VPC 2000 solution was added to fill the LED cup as shown in Fig. 77, and then it was placed in an oven at 88°C and kept at that temperature for one day. The material cured to form a colorless, clear solid with several cracks occurring within the cup. This cracking was likely due to volume expansion during curing and is the subject of ongoing study.

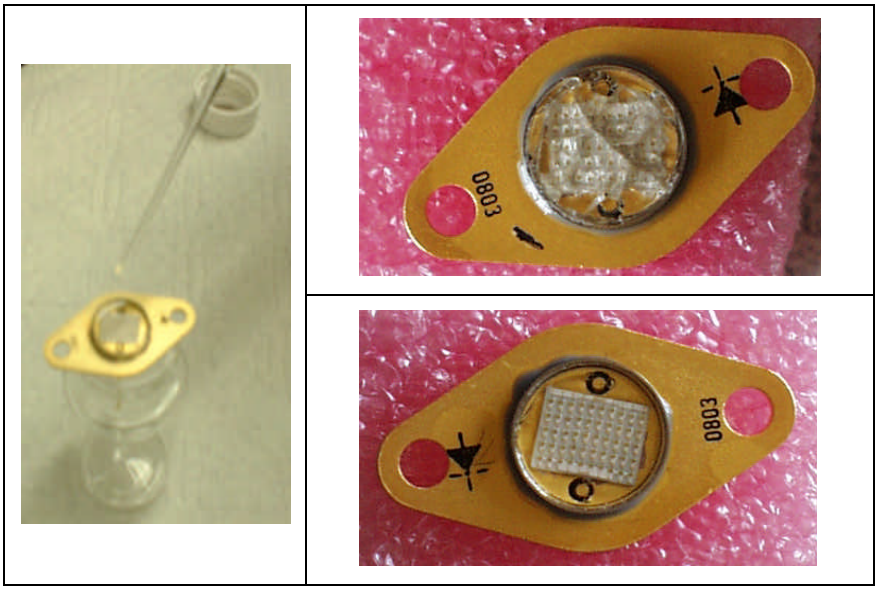

Fig. 77. Encapsulation of an LED array with VPC 2000 (Left: Filling of the LED cup, Right: cured product).

When the Lighting Research Center bought the bare 50-array product, four epoxy-filled commercial products from the same manufacturing batch were also acquired. One of the cured products (Fig. 77, right bottom) was life-tested in the Light Research Center together with one of the epoxy-filled commercial products. The life-test setup was the same as for the high-power LED benchmarking task. To date, more than 700 hours of life-test data have been collected. Figure 78 illustrates the comparison of the light output degradation rates of devices using RPI epoxy and those with the commercial product. The RPI epoxy device seems to degrade slower than the commercial product. A small volume of RPI-developed VPC2000 epoxy was sent to UCSB for further evaluation.

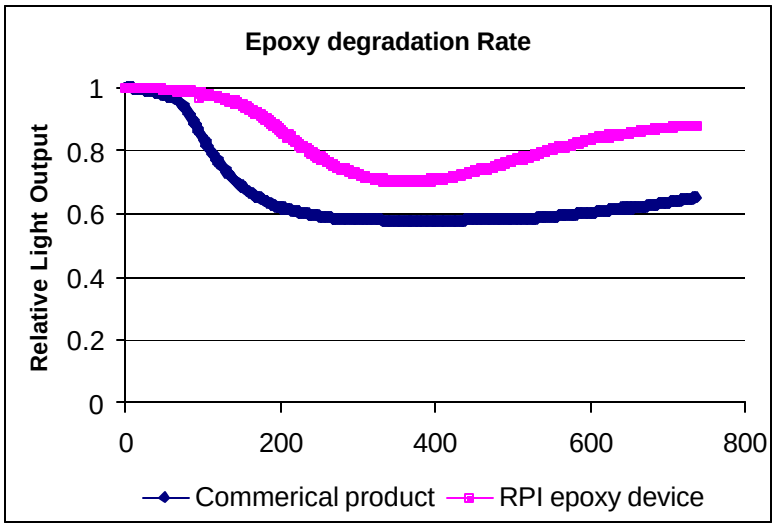

Fig. 78. Comparison of the light output degradation rates of devices using RPI epoxy and those of a commercial product.

Future work

More Shark LED devices have been ordered, and the LRC plans to life-test more RPI-epoxy devices and those with the OCK451 epoxy. Presently one or two other commercial products have appeared in the market. In addition to RPI epoxy, LRC will test some of these commercial epoxies on actual LED devices.

CONCLUSIONS

As detailed in the Results section, we have made significant progress in the areas of UV LED development, RCLED device design, lateral overgrowth by MOCVD and HVPE, and lighting and epoxy design. We have demonstrated that although AlGaN based UV LEDs were grown in tension on GaN base layers, an AlN interlayer could be inserted which allowed the growth of crack-free devices. Despite the LED being grown on an absorbing GaN base layer, we have demonstrated 0.367 mW of output power at 336 nm under pulsed conditions for 200 x 200 μm standard square geometry LEDs. The current devices are limited by self-heating due to high non-radiative recombination and current crowding in the n-type contact layer causing non-uniform current injection. We have shown that current packaging technology for nitride-based LEDs is absorbing in the ultraviolet spectrum and requires further development for commercialization of ultraviolet LEDs.

Our initial RCLED results have been promising, with bright emission from initial test structures utilizing a n-GaN-air 'interfacial' mirror and a p-GaN Ag mirror/contact. These structures exhibited mode structures in their electroluminescence spectra, the spacing of which agreed with the actual cavity length. Studies are underway to improve Ag mirror reflectivity and also deposit a oxide dielectric DBR stack on the n-GaN (front) side of the devices to achieve a controllable and reproducible reflectivity value of 50%. Cavity thinning via a combination of chemical-mechanical polishing and dry etching by either reactive-ion etching or inductively-coupled plasma etching is being pursued. As demonstrated above, we have observed clear modal behavior via the appearance of a far-field "rabbit-ear" intensity distribution.

LEO of non-polar $(11\bar{2}0)$ a-plane GaN films by both MOCVD and HVPE was demonstrated and threading dislocation density reduction was achieved. The low symmetry a-GaN surface exhibited LEO stripe morphologies that were dependent on crystallographic stripe alignment. Two primary orientations, $[0001]$ and $[\bar{1}100]$, were observed to possess uniform, symmetric stripe morphologies; $[\bar{1}100]$ stripes had vertical sidewalls while $[0001]$ stripes had coexisting vertical and inclined sidewalls. Dislocation reduction was achieved in $[\bar{1}100]$ stripes while dislocations propagated into the laterally overgrown regions of $[0001]$ stripes. Between the $[0001]$ and $[\bar{1}100]$ orientations, asymmetric stripe morphologies were observed. Except for $[0001]$ stripes, which had a non-polar lateral growth direction, all stripes exhibited asymmetric lateral growth rates. Fully coalesced HVPE LEO a-GaN layers were obtained over entire 2" wafers. With optimization of surface smoothness after coalescence, we will increase overall thickness to the point where mechanically stable free-standing a-GaN wafers can be made by removing the r-plane sapphire substrate.

Our work on solid-state lighting design has primarily focused on benchmarking existing commercially available LEDs for comparison with those fabricated during this study, designing optimum packaging for RCLED structures, and developing epoxy compositions that will be thermally stable as well as transmissive in the UV wavelengths of interest in this study. We have recently formulated epoxy resins that are thermally stable, but need further optimization to avoid cracking during curing. This and other epoxy development issues are the subjects of ongoing study.

REFERENCES

[1] I. P. Smorchkova, C. R. Elsass, J. P. Ibbetson, R. Vetury, B. Heying, P. Fini, E. Haus, S. P. DenBaars, J. S. Speck, and U. K. Mishra, J. Appl. Phys. **86,** 4520-6 (1999).

[2] O. Ambacher, J. Smart, J. R. Shealy, N. G. Weimann, K. Chu, M. Murphy, W. J. Schaff, L. F. Eastman, R. Dimitrov, L. Wittmer, M. Stutzmann, W. Rieger, and J. Hilsenbeck, J. Appl. Phys. **85,** 3222-33 (1999).

[3] I. Jin Seo, H. Kollmer, J. Off, A. Sohmer, F. Scholz, and A. Hangleiter, Phys. Rev. B **57,** R9435-8 (1998).

[4] R. Langer, J. Simon, V. Ortiz, N. T. Pelekanos, A. Barski, R. Andre, and M. Godlewski, Appl. Phys. Lett. **74,** 3827-9 (1999).

[5] P. Lefebvre, J. Allegre, B. Gil, H. Mathieu, N. Grandjean, M. Leroux, J. Massies, and P. Bigenwald, Phys. Rev. B **59,** 15363-7 (1999).

[6] P. Lefebvre, A. Morel, M. Gallart, T. Taliercio, J. Allegre, B. Gil, H. Mathieu, B. Damilano, N. Grandjean, and J. Massies, Appl. Phys. Lett. **78,** 1252-4 (2001).

[7] T. Takeuchi, C. Wetzel, S. Yamaguchi, H. Sakai, H. Amano, I. Akasaki, Y. Kaneko, S. Nakagawa, Y. Yamaoka, and N. Yamada, Appl. Phys. Lett. **73,** 1691-3 (1998).

[8] T. S. Zheleva, N. Ok-Hyun, M. D. Bremser, and R. F. Davis, Appl. Phys. Lett. **71,** 2472-4 (1997).

[9] N. Ok-Hyun, M. D. Bremser, T. S. Zheleva, and R. F. Davis, Appl. Phys. Lett. **71,** 2638-40 (1997).

[10] H. Marchand, J. P. Ibbetson, P. T. Fini, P. Kozodoy, S. Keller, S. DenBaars, J. S. Speck, and U. K. Mishra, MRS Internet J. Nitride Semicond. Res. **3,** 3 (1998).

[11] H. Marchand, X. H. Wu, J. P. Ibbetson, P. T. Fini, P. Kozodoy, S. Keller, J. S. Speck, S. P. DenBaars, and U. K. Mishra, Appl. Phys. Lett. **73,** 747-9 (1998).

[12] S. Nakamura, M. Senoh, S. I. Nagahama, T. Matsushita, K. Kiyoku, Y. Sugimoto, T. Kozaki, H. Umemoto, M. Sano, and T. Mukai, Jpn. J. Appl. Phys. **38,** L226-9 (1999).

[13] M. D. Craven, S. H. Lim, F. Wu, J. S. Speck, and S. P. DenBaars, (to be published).

[14] D. Kapolnek, S. Keller, R. Vetury, R. D. Underwood, P. Kozodoy, S. P. DenBaars, and U. K. Mishra, Appl. Phys. Lett. **71,** 1204-6 (1997).

[15] J. Park, P. A. Grudowski, C. J. Eiting, and R. D. Dupuis, Appl. Phys. Lett. **73,** 333-5 (1998).

[16] S. J. Rosner, G. Girolami, H. Marchand, P. T. Fini, J. P. Ibbetson, L. Zhao, S. Keller, U. K. Mishra, S. P. DenBaars, and J. S. Speck, Appl. Phys. Lett. **74,** 2035-7 (1999).

[17] J. A. Freitas, Jr., N. Ok-Hyun, R. F. Davis, G. V. Saparin, and S. K. Obyden, Appl. Phys. Lett. **72,** 2990-2 (1998).

[18] Z. Yu, M. A. L. Johnson, J. D. Brown, N. A. El-Masry, J. F. Muth, J. W. Cook, Jr., J. F. Schetzina, K. W. Haberern, H. S. Kong, and J. A. Edmond, MRS Internet J. Nitride Semicond. Res. **4S1** (1999).

[19] Narendran *et al.*, Proc. SPIE 5187 (2003) in press.

[20] Steigerwald *et al.*, IEEE Journal on Selected Topics in Quantum Electronics 8(2) (2002) 310.

[21] Bockstaele, Resonant Cavity Light Emitting Diode Based Parallel Optical Interconnections, Ghent University, 2001.

[22] Delbeke, Design and Fabrication of a Highly Efficient Light-emitting Diode: the Grating-Assisted Resonant-Cavity Light-Emitting Diode, Ghent University, Belgium, 2002.

[23] Streubel *et al.*, IEEE Journal on Selected Topics in Quantum Electronics, 8(2) (2002) 321.

[24] Krames et al., Appl. Phys. Lett. 75 (1999) 2365.

[25] Schad, Extraction efficiency of GaN-based LEDs. Annual report 2000, Optoelectronics department, University of Ulm, 2000.

[26] Schmid *et al.*, IEEE J. Sel. Top. Quantum Electron 8(2) (2002) 256.

[27] Windisch *et al.*, Appl. Phys. Lett. 74(16) (1999) 2256.

[28] Stefanov *et al.*, Proc. SPIE 4776 (2002) 223.

[29] Delbeke, IEEE Journal on Selected Topics in Quantum Electronics 8(2) (2002) 189.